UNIVERSITÀ
DEGLI STUDI
FIRENZE

Self-bound quantum droplets in Bose-Bose mixture

Settore scientifico disciplinare: FIS/03 Fisica della materia

Dottorando:
Giovanni Ferioli

Tutor:
Prof. Marco Fattori

Coordinatore:
Prof. Francesco Saverio Cataliotti

And why do we fall, Bruce? So we can learn to pick ourselves up..

<div style="text-align: right">Thomas Wayne, "Batman Begins" (probably about vacuum leaks)</div>

Abstract

Self-bound quantum systems appear in different physical scenarios. They result from the balance between attractive and repulsive forces. Recently the existence of a new object belonging to this class has been discovered. Using a bosonic mixture of ultracold atoms, it is possible to generate a self-bound state resulting from the interplay between an attractive mean-field energy and the repulsive first-order perturbative correction, the so-called Lee-Huang-Yang term. This system is known as quantum droplet.

During my PhD we have experimentally observed and characterized this novel quantum state. Thanks to an innovative technique, based on a time-averaged potential, we were able to levitate the mixture and study for the first time the self-bound nature of quantum droplets in 3D free space. We characterized their equilibrium properties, i.e. the size, the critical atom number for their formation and the spin imbalance, finding a very good agreement with the theoretical predictions.

Despite being extremely dilute, for large atom numbers quantum droplets enter a liquid-like incompressible regime, highlighted by the formation of a bulk with uniform density. We investigate the occurrence of this incompressible regime by studying collisions between two droplets. This is indeed a powerful tool to gain information about the energy scales characterizing the system. To this aim, we implemented an experimental sequence able to create two separate quantum droplets and to imprint them a tunable relative velocity.

By characterizing the outcomes of the collisions for different values of velocities and atom numbers in the droplets and comparing them with the results of energetic considerations and numerical simulations, we obtained the first evidence of a crossover between compressible and incompressible regimes.

Contents

Chapter 1

Introduction

Everyday life is characterized by the presence of matter in different phases. In several systems it is also possible to observe the transformations between two of such phases, i.e., a so-called phase transition. A remarkable example in this sense is that of water, where gaseous, liquid and solid phases and their corresponding phase transitions can be observed in easily accessible ranges of pressure and temperature. From a physical point of view, it is not trivial to understand the origin of a liquid phase. A first explanation was proposed in a pioneering work of J. van der Waals in 1873. In the model he developed, the liquid phase results from the presence of a repulsive and an attractive energy in the microscopic Hamiltonian describing the system. These two forces create an inter-particle potential that is repulsive for short distances and attractive for large separations, thus presenting a minimum at a finite value of the inter-particle distance. In this microscopic model, the long range attractive force is provided by a dipole-dipole interaction or other weak forces, while the short-range repulsion comes from the Pauli exclusion principle acting on the electrons of the external shells of the atoms. Extending this idea, we could state that a liquid phase, characterized by a bulk with a fixed saturation density, can be created as the result of the interplay between an attractive and a repulsive force, generating a microscopic potential $V(R)$ which displays an absolute minimum for a finite value of the inter-particle distance R.

As the temperature is decreased, we usually find matter either in liquid or solid phases. Conversely to this standard picture, in the past few decades scientists have been able to create gaseous ensembles of alkali atoms at extremely low temperatures, of the order of few tens of nK [1, 2]. These ultracold and extremely dilute systems fulfil the condition of quantum degeneracy between their constituents particles, thus forming either Bose-Einstein condensates (BECs) or Fermi degenerate gases, according to their statistics. As a consequence of both the diluteness and the low temperatures in these systems, the interatomic potential characterizing their microscopic Hamiltonian is quite different from the van der Waals potential introduced above. In terms of their mutual interactions, ultracold atoms can indeed be represented as hard spheres of size a, known as scattering length, which is much larger than the position of the minimum in the van der Waals potential. For this reason, it is not possible to reach a liquid regime in a conventional way [3]. In the years, different mechanisms have been proposed to create a liquid-like phase in ultracold quantum gases, for example exploiting the interplay between an attractive two-body interaction and a repulsive three-body term [4], but none of them has been verified in an experiment so far.

In 2015 the physicist D. Petrov proposed an innovative method to create a quantum liquid state starting from a quantum gas [5]. This new system, known as quantum droplet, is the result of an attractive mean-field energy (MF) balanced by the repulsive energy provided by the first-order perturbative correction to it, the so-called Lee-Huang-Yang (LHY) term. The latter comes from the effect of quantum fluctuations, that create a finite leak from the ground state to finite momentum states, even in a BEC at zero temperature. This fundamental leak

is known as quantum depletion. In a single component BEC, the MF and LHY terms have normally the same sign. Additionally, as a consequence of the diluteness of the BEC, the LHY term is typically negligible with respect to the MF. In the case of a bosonic mixture, the situation can change. It is indeed characterized by the presence of three different collisional channels: the intra-species scattering lengths a_{ii}, describing the interaction between atoms belonging to the same atomic species, and the inter-species interaction, governed by a_{ij} and describing the interaction between different atoms. Properly choosing the three interaction strengths and the relative density between the two species, Petrov pointed out that it is possible not only to make the energy contributions provided by the MF and LHY terms comparable in size, but they can also have opposite signs. The competition between these two energies can then lead to the formation of self-bound liquid-like droplets [5].

Almost concurrently to Petrov's theoretical work, it was discovered in an experiment the existence of analogous quantum droplets in dipolar BECs [6]. The strong magnetic moment of these atomic species introduces another collisional channel in addition to contact interactions, i.e. the dipole-dipole interaction. The latter plays the same role as the inter-species interaction in mixtures and it can be used to gently tune the MF energy to negative values, by varying the aspect ratio of the trap. This tool can be used to form self-bound systems stabilized by the same physical mechanism introduced above.

Despite the similar stabilization mechanism, the two quantum droplets present several differences. The most important is that the ones formed with dipolar atoms are elongated in one direction, as a consequence of the anisotropic dipolar interaction. Conversely, the self-bound systems created from Bose-Bose mixtures are spherical in free space. The excitation spectrum is thus expected to be different. In particular, it has been predicted that, under specific conditions, spherical quantum droplets automatically evaporate excitations and cool down to zero temperature [5]. This happens because the particle emission threshold is lower in energy than any excitation mode, i.e. it is energetically favorable for the droplet to release atoms than to be in an excited state. This peculiar and exotic property was not clearly observed so far and it is certainly one of the most interesting outlooks of the present work.

Another interesting feature of quantum droplets is that, despite being extremely dilute, they present liquid-like properties, closely analogous to those of classical liquids. When increasing the atom number, the ground-state wavefunction reaches a saturation density, so that it develops a bulk with uniform density and very weak compressibility [5].

Experimentally, quantum droplets have been first observed in dipolar BECs of Dysprosium atoms, in Stuttgard in the group led by Tilman Pfau [7, 8], and with Erbium atoms, in Innsbruck in Francesca Ferlaino's group [9]. Shortly after, the first experiments have been realized also with bosonic mixtures, in the group led by Leticia Taruell in Barcelona in confined spatial geometries [10, 11] and in our group in Florence in three-dimensional free space [12].

In general, the investigation of quantum droplets forming in ultracold atomic systems could be a useful tool to understand complex quantum systems beyond the mean-field paradigm. For example, another quantum self-bound state, that has been extensively studied from both an experimental and a theoretical point of view [13, 14], is that of Helium clusters. The challenging aspect in this kind of studies is that, due to the high density in these systems, it is hard to find a simple microscopic theory able to reliably reproduce their properties. Quantum droplets have densities 6 to 8 orders of magnitude smaller than those of Helium drops, so that they constitute an analogous system much easier to describe at the microscopic level.

The thesis is structured as follows. In Chapter 2 I introduce the theory of quantum droplets formed in bosonic mixtures, addressing, in particular, the conditions for their formation, their equilibrium properties and some basic notions about their excitation spectrum. In Chapter 3 I describe in detail a key ingredient for the experimental study of droplets in 3D free space,

i.e. the compensation of gravity, which is realized by making use of a time-averaged optical potential. The experimental results concerning the observation and characterization of a single quantum droplet are reported in Chapter 4. Finally, in Chapter 5 I report on the study of collisions between two quantum drops. By characterizing the outcomes of such collisions as a function of the collision velocity and of the atom number in the droplets, we get insights on the relevant energy scales in the system and we find a first hint of a crossover between a compressible and an incompressible regime, driven by the total atom number. In Chapter 6 I summarize the results of the study about quantum droplets and discuss some future perspectives of this work.

In the first part of my PhD I participated in an experimental study concerning the dynamics of a BEC in an optical double-well potential. The capability of tuning the interactions in the system allows to study with great accuracy the interplay between tunneling and interaction energies in the dynamics of a bosonic Josephson Junction. This kind of study paves the way to the realization of a trapped atomic interferometer. Since the largest part of my PhD has been dedicated to the experimental study of quantum droplets, this thesis is mainly dedicated to that topic. Nonetheless, in Chapter 7 I report the results of the theoretical study I have carried out to characterize the stability of the atomic interferometer we are planning to realize in the near future.

List of publications

- **Ferioli, G.**, Semeghini, G., Masi, L., Giusti, G, Modugno, Inguscio, M., G., Gallemí, A., Recati, A., Fattori, M. (2019). Collisions Of Self-Bound Quantum Droplets. Physical Review Letters, 122(9), 090401

- Semeghini, G., **Ferioli, G.**, Masi, L., Mazzinghi, C., Wolswijk, L., Minardi, F., Modugno, G., Modugno, M., Inguscio, M., Fattori, M. (2018). Self-Bound Quantum Droplets of Atomic Mixtures in Free Space. Physical Review Letters, 120(23), 235301.

- Spagnolli, G., Semeghini, G., Masi, L., Ferioli, G., Trenkwalder, A., Coop, S., Landini, M., Pezzé, L., Modugno, G., Inguscio, M., Smerzi, A., Fattori, M. (2017). Crossing over from attractive to repulsive interactions in a tunneling bosonic Josephson junction. Physical review letters, 118(23), 230403.

Chapter 2

Theory

In this chapter I present the theory that describes the formation of a quantum droplet and its properties. After reporting the mean-field (MF) description of a single species BEC, I will introduce the first-order perturbative correction, the so-called Lee-Huang-Yang (LHY) term. I will then generalize the results obtained for a single species BEC to the case of a Bose-Bose mixture, discussing the mechanism leading to the formation of quantum droplets. At the end of the chapter I will describe some equilibrium and dynamical properties of the droplets.

2.1 Weakly interacting bosonic systems

A three-dimensional system made of N interacting bosonic particles in free space is described by a many-body Hamiltonian:

$$\hat{H} = -\frac{\hbar^2}{2m} \sum_{i=1}^{N} \frac{d^2}{d\boldsymbol{r}^2} + \sum_{i=1}^{N} \sum_{j=i+1}^{N} U(\boldsymbol{r}_i - \boldsymbol{r}_j) \tag{2.1}$$

where $U(\boldsymbol{r}_i - \boldsymbol{r}_j)$ is the inter-particle potential, m is the mass of the atom we are considering and $\hbar$ is the Plank constant divided by 2π. In the context of ultracold atoms, one can introduce the approximation:[15]

$$U(\boldsymbol{r}_i - \boldsymbol{r}_j) \simeq g\delta(\boldsymbol{r}_i - \boldsymbol{r}_j) \tag{2.2}$$

where the coupling constant $g = \frac{4\pi\hbar^2 a}{m}$. The approximation to a contact potential is valid when both the average distance between particles, $d = (V/N)^{1/3}$, and the thermal De Broglie wavelength, $\lambda_T = \sqrt{2\pi\hbar^2/mk_B T}$, are much larger than the range of the interatomic forces. In typical experimental situations, both conditions are fulfilled. In this picture the only parameter that describes the strength of the interaction between two identical ultracold atoms is the so called scattering length a. Thanks to magnetic Feshbach resonances [16], a can be tuned in experiments by applying a uniform magnetic field, so that $a = a(B)$. Using this tool it is then possible to change the sign of the interactions, making it repulsive for $a > 0$, attractive for $a < 0$ and create a non-interacting system for $a = 0$.

A more suitable way of treating the many-body problem is to use the formalism of second quantization. In this framework, the many-body Hamiltonian in Eq. 2.1 becomes the Hamiltonian of the quantum field theory:

$$H = \int d\boldsymbol{r}\,\Psi^\dagger(\boldsymbol{r})(-\frac{\hbar^2}{2m}\nabla^2)\Psi(\boldsymbol{r}) + \frac{1}{2}\int d\boldsymbol{r}d\boldsymbol{r}'\Psi^\dagger(\boldsymbol{r})\Psi^\dagger(\boldsymbol{r}')U(\boldsymbol{r}-\boldsymbol{r}')\Psi(\boldsymbol{r})\Psi(\boldsymbol{r}') \tag{2.3}$$

where $\Psi(\boldsymbol{r})$ and $\Psi^\dagger(\boldsymbol{r})$ are the annihilation and creation operators respectively satisfying the bosonic commutation rules and $N = \int d\boldsymbol{r}\Psi^\dagger(\boldsymbol{r})\Psi(\boldsymbol{r})$ is the atom number operator.

Making use of the pseudopotential approximation introduced in Eq. 2.2, the previous second quantization hamiltonian is simplified:

$$H = \int d\boldsymbol{r}\Psi^\dagger(\boldsymbol{r})(-\frac{\hbar^2}{2m}\nabla^2)\Psi(\boldsymbol{r}) + \frac{g}{2}\int d\boldsymbol{r}\Psi^\dagger(\boldsymbol{r})\Psi^\dagger(\boldsymbol{r})\Psi(\boldsymbol{r})\Psi(\boldsymbol{r}) \tag{2.4}$$

For a uniform gas occupying a volume V the field operators can be conveniently written as the superposition of plane waves:

$$\Psi(r) = \frac{1}{\sqrt{V}}\sum_{\boldsymbol{p}} a_{\boldsymbol{p}} e^{i\boldsymbol{pr}/\hbar} \tag{2.5}$$

where $a_{\boldsymbol{p}}$ is the operator annihilating a particle in the single-particle state with momentum $\boldsymbol{p}$. Using Eq. 2.5 it is possible to write the many-body Hamiltonian operator as:

$$H = \sum_{\boldsymbol{p}} \frac{p^2}{2m} a_{\boldsymbol{p}}^\dagger a_{\boldsymbol{p}} + \frac{g}{2V}\sum_{\boldsymbol{p1},\boldsymbol{p2}} a_{\boldsymbol{p1}}^\dagger a_{\boldsymbol{p2}}^\dagger a_{\boldsymbol{p1}} a_{\boldsymbol{p2}} \tag{2.6}$$

2.1.1 Mean-field energy and beyond-mean-field correction

Using the Hamiltonian in Eq. 2.6 it is possible to evaluate the ground state energy of a weakly interacting Bose gas. This can be done by using the so-called MF approximation , which is based on the replacement of the operator $a_{\boldsymbol{p=0}}$ with a c-number, i.e.:

$$a_{\boldsymbol{p=0}} = \sqrt{N_0} \tag{2.7}$$

where N_0 is number of particles with a momentum $\boldsymbol{p} = \boldsymbol{0}$. This approximation is accurate for a dilute gas at very low temperature, $T \simeq 0$. In this case the occupation number of states with $\boldsymbol{p} \neq \boldsymbol{0}$ is small. This means that, in the first approximation, all the creation and annihilation operators of states with $\boldsymbol{p} \neq \boldsymbol{0}$ can be neglected in the Hamiltonian in Eq. 2.6. In this limit the ground state energy of a weakly interacting BEC in free space is:

$$E_0 = \frac{g}{2} nN \tag{2.8}$$

where $n = N/V$ is the atomic density. The energy density associated to this is $\epsilon_0 = \frac{g}{2} n^2$. This energy contribution is called mean-field energy because it is obtained by neglecting the quantum or thermal fluctuations around the expectation value of the operator $n_0 = a_{\boldsymbol{p=0}}^\dagger a_{\boldsymbol{p=0}}$. Using the same approximation, several properties of the weakly interacting gas can be calculated, as the quantum pressure P

$$P = -\frac{\partial E_0}{\partial V} = \frac{1}{2} gn^2 \tag{2.9}$$

that is different from zero also at $T = 0$ and positive for a system with repulsive interactions. In the same way it is easy to obtain that the compressibility k_T is also finite:

$$k_T = \frac{\partial n}{\partial P} = \frac{1}{gn} \tag{2.10}$$

The sound velocity c can be deduced from the compressibility using:

$$k_T = \frac{1}{mc^2} \tag{2.11}$$

and so $c = \sqrt{\frac{gn}{m}}$.

Finally, it is possible to evaluate also the chemical potential μ of the system, as

$$\mu = \frac{\partial E_0}{\partial N} = gn = mc^2 \tag{2.12}$$

7

This is the energy required to add one particle into the condensate or the energy gained by subtracting one particle from it.

I will now extend the mean field results, by taking into account the field operators of states with momentum $\boldsymbol{p} \neq \boldsymbol{0}$. Since the collision between two ultracold atoms is elastic, in the many-body Hamiltonian in Eq. 2.6 the terms containing only one field operator with $\boldsymbol{p} = 0$ are not allowed by momentum conservation. If the temperature is small enough, we can restrict the collision terms to the cases of interaction between one particle with $\boldsymbol{p} = \boldsymbol{0}$ and one particle with momentum different from zero. The Hamiltonian can be written as:

$$H = \frac{g}{2V}a_0^\dagger a_0^\dagger a_0 a_0 + \sum_{\boldsymbol{p}} \frac{p^2}{2m}a_{\boldsymbol{p}}^\dagger a_{\boldsymbol{p}} + \frac{g}{2V}\sum_{\boldsymbol{p}} 4a_0^\dagger a_{\boldsymbol{p}}^\dagger a_0 a_{\boldsymbol{p}} + a_{\boldsymbol{p}}^\dagger a_{-\boldsymbol{p}}^\dagger a_0 a_0 + a_0^\dagger a_0^\dagger a_{\boldsymbol{p}} a_{-\boldsymbol{p}} \tag{2.13}$$

In particular, the energy terms in the last sum in equation Eq. 2.13 takes into account the collisions between particles with (i) $\boldsymbol{p_1} = \boldsymbol{0}$, $\boldsymbol{p_2} = \boldsymbol{p}$ and no momentum transfer, (ii) $\boldsymbol{p_1} = \boldsymbol{p}$, $\boldsymbol{p_2} = \boldsymbol{0}$ and again no momentum transfer, (iii) $\boldsymbol{p_1} = \boldsymbol{0}$, $\boldsymbol{p_2} = \boldsymbol{p}$ but a momentum transfer $\boldsymbol{p}$ and finally (iv) $\boldsymbol{p_1} = \boldsymbol{p}$, $\boldsymbol{p_2} = \boldsymbol{0}$ and momentum transfer $-\boldsymbol{p}$. The two cases (i) and (ii) do not involve the transfer of a momentum between two particles, for this reason they are called direct terms. The other two cases (ii) and (iv), instead, involve the transfer of momentum between two particles, so they are called exchange terms. Identical quantum particles are indistinguishable, so we take into account all those direct and exchange terms.

As done before, it is now possible to replace the operator a_0 with its expectation value $\sqrt{N}$ in the last term of Eq. 2.13. In the first term, instead, we use a normalization relation:

$$a_0^\dagger a_0 + \sum_{\boldsymbol{p}\neq\boldsymbol{0}} a_{\boldsymbol{p}}^\dagger a_{\boldsymbol{p}} = N \tag{2.14}$$

or equivalently

$$a_0^\dagger a_0^\dagger a_0 a_0 \simeq N^2 - 2N \sum_{\boldsymbol{p}\neq 0} a_{\boldsymbol{p}}^\dagger a_{\boldsymbol{p}} \tag{2.15}$$

where we neglect the hight order terms .

Substituting Eq. 2.15 into the many-body Hamiltonian reported in Eq. 2.13, we get:

$$H = \frac{1}{2}gnN + \sum_{\boldsymbol{p}} \frac{p^2}{2m}a_{\boldsymbol{p}}^\dagger a_{\boldsymbol{p}} + \frac{1}{2}gn \sum_{\boldsymbol{p}\neq\boldsymbol{0}} (2a_{\boldsymbol{p}}^\dagger a_{\boldsymbol{p}} + a_{\boldsymbol{p}}^\dagger a_{-\boldsymbol{p}}^\dagger + a_{\boldsymbol{p}} a_{-\boldsymbol{p}}) \tag{2.16}$$

where the third term represents the energy of the excited states due to the interaction, the simultaneous creation of the excited states at momenta $\boldsymbol{p}$ and $-\boldsymbol{p}$, and simultaneous annihilation of the excited states respectively.

The Hamiltonian in Eq. 2.16 can be diagonalized using the so-called Bogoliubov transformations, [17]:

$$a_{\boldsymbol{p}} = u_{\boldsymbol{p}} b_{\boldsymbol{p}} + v_{-\boldsymbol{p}} b_{-\boldsymbol{p}}^\dagger \tag{2.17}$$

and

$$a_{\boldsymbol{p}}^\dagger = u_{\boldsymbol{p}} b_{\boldsymbol{p}}^\dagger + v_{-\boldsymbol{p}} b_{-\boldsymbol{p}} \tag{2.18}$$

The two parameters $u_{\boldsymbol{p}}$ and $v_{\boldsymbol{p}}$ in Eqs. 2.17 and 2.18 are determined by imposing that the two operators $b_{\boldsymbol{p}}$ and $b_{\boldsymbol{p}}^\dagger$ obey the bosonic commutation rules, as the field operators $a_{\boldsymbol{p}}$ and $a_{\boldsymbol{p}}^\dagger$. This assumption is fulfilled if:

$$u_{\boldsymbol{p}}^2 - v_{-\boldsymbol{p}}^2 = 1 \tag{2.19}$$

or equivalently

$$u_{\boldsymbol{p}} = \cosh(\alpha_{\boldsymbol{p}}) \tag{2.20}$$

$$v_{-\boldsymbol{p}} = \sinh(\alpha_{\boldsymbol{p}}) \tag{2.21}$$

Imposing the condition on the bosonic nature of the two Bogoliubov operators b and $b^\dagger$, the transformation matrix depends only on one parameter, i.e. $\alpha_{\boldsymbol{p}}$. It is possible to chose it such that the non-diagonal terms in Eq.2.16 become zero. With some calculations [18] it is possible to prove that this condition is fulfilled for

$$\coth(2\alpha_{\boldsymbol{p}}) = -\frac{p^2/2m + gn}{gn} \tag{2.22}$$

from which it is possible to determine uniquely the two coefficients of the Bogolubov transformation $u_{\boldsymbol{p}}$ and $v_{-\boldsymbol{p}}$:

$$u_{\boldsymbol{p}}, v_{-\boldsymbol{p}} = \pm\sqrt{\frac{p^2/2m + gn}{2\epsilon(p)} \pm \frac{1}{2}} \tag{2.23}$$

where $\epsilon(p)$ is the famous Bogoliubov dispersion relation:

$$\epsilon(p) = \sqrt{\left(\frac{p^2}{2m}\right)^2 + p^2\frac{gn}{m}} \tag{2.24}$$

Finally, we can write the diagonalized hamiltonian:

$$H = \frac{1}{2}gnN + \frac{1}{2}\sum_{\boldsymbol{p}\neq 0}(\epsilon(p) - gn - \frac{p^2}{2m} + \frac{m(gn)^2}{p^2}) + \sum_{\boldsymbol{p}\neq 0}\epsilon(p)b_{\boldsymbol{p}}^\dagger b_{\boldsymbol{p}} \tag{2.25}$$

The results in Eq. 2.25 have a very deep physical meaning: the dynamics of an interacting many-body Bose gas can be described using a Hamiltonian of a non-interacting quasi-particles, representing the collective excitations of the system. These quasi-particles have a dispersion relation given by $\epsilon(p)$. To understand better this picture it is possible to consider two limits: as previously shown, the speed of sound of an interacting BEC is given by $c = \sqrt{gn/m}$; the momentum related to it is then $p_{sound} = \sqrt{mgn}$. If $p \ll p_{sound}$, using the expression for $u_{\boldsymbol{p}}$ and for $v_{-\boldsymbol{p}}$ in Eqs. 2.17 and 2.18, we get that $|u_{\boldsymbol{p}}| \simeq |v_{-\boldsymbol{p}}| \gg 1$ and so:

$$a_{\boldsymbol{p}} \simeq u_{\boldsymbol{p}}(b_{\boldsymbol{p}} - b_{-\boldsymbol{p}}^\dagger) \tag{2.26}$$

In this limit, a real particle described by the field operators $a_{\boldsymbol{p}}$ and $a_{\boldsymbol{p}}^\dagger$ is represented as the superposition of the forward propagating of many quasi-particles $u_{\boldsymbol{p}}b_{\boldsymbol{p}}$ and the backward propagating of $v_{-\boldsymbol{p}}b_{-\boldsymbol{p}}^\dagger$.

In the opposite limit $p \gg p_{sound}$, instead, we get that $u_{\boldsymbol{p}} \simeq 1$ but $v_{-\boldsymbol{p}} \simeq 0$. In this case the quasi-particle becomes indistinguishable from real one, i.e. $a_{\boldsymbol{p}} \simeq b_{\boldsymbol{p}}$

The ground state at $T = 0$ corresponding to the vacuum state for Bogoliubov quasi-particle, i.e. for every $\boldsymbol{p} \neq 0$ the ground state satisfies:

$$b_{\boldsymbol{p}}|0\rangle = 0 \tag{2.27}$$

The first-order perturbation correction to the mean-field energy has been calculated by Lee, Huang and Yang (LHY) in [19, 20] and it can be obtained from the Hamiltonian in Eq. 2.25 as:

$$E = \frac{1}{2}gnN(1 + \frac{128}{15\sqrt{\pi}}(na^3)^{1/2}) \tag{2.28}$$

The related chemical potential is given by:

$$\mu = gn(1 + \frac{32}{3\sqrt{\pi}}(na^3)^{1/2}) \tag{2.29}$$

The LHY correction to the MF energy is proportional to $\sqrt{na^3}$. For this reason, the LHY term is typically negligible in the dilute system with $an^3 \ll 1$ and it is thus difficult to be measured

in expereiments. A possibility in this sense is to work with divergent scattering length making use of a Feshbach resonance. Strongly correlated system like this are usually called unitary Bose gases [21, 22]. Experimental observation of the LHY perturbative correction have been made so far using the equation of state of an unitary Bose gas [23] or probing the system with RF spectroscopy [24, 25, 26, 27].

2.1.2 Quantum depletion

As shown in the previous section, a weakly-interacting BEC can be treated as a non-interacting system made of quasi-particles. The effect of the interaction is to create a leak in the occupation of the ground state of the BEC even at zero temperature, this is called quantum depletion. Mathematically this is a direct consequence of the Bogoliubov's prescription, indeed the field operators of this quasi-particles obey Bose statistic. For this reason the mean number of quasi-particles with momentum $\boldsymbol{p}$ must satisfy:

$$N_{\boldsymbol{p}}^{excitations} = \langle b_{\boldsymbol{p}}^{\dagger} b_{\boldsymbol{p}} \rangle = \frac{1}{e^{\beta\epsilon(p)} - 1} \tag{2.30}$$

where $\beta = 1/k_B T$. This number is different from the average number of real particles with momentum $\boldsymbol{p}$ given by:

$$N_{\boldsymbol{p}} = \langle a_{\boldsymbol{p}}^{\dagger} a_{\boldsymbol{p}} \rangle = |v_{-\boldsymbol{p}}|^2 (1 + \langle b_{-\boldsymbol{p}}^{\dagger} b_{-\boldsymbol{p}} \rangle) + |u_{\boldsymbol{p}}|^2 \langle b_{\boldsymbol{p}}^{\dagger} b_{\boldsymbol{p}} \rangle \tag{2.31}$$

where we use the definition of the Bogoliubov operators and the fact that $\langle b_{\boldsymbol{p}} b_{-\boldsymbol{p}} \rangle = \langle b_{\boldsymbol{p}}^{\dagger} b_{-\boldsymbol{p}}^{\dagger} \rangle = 0$. Making use of the expression in Eq. 2.30, it is possible to prove that the number of atoms in the BEC corresponds to:

$$N_0 = N - \sum_{\boldsymbol{p} \neq \boldsymbol{0}} N_{\boldsymbol{p}} = N - \frac{V}{(2\pi\hbar)^3} \int dp (|v_{-\boldsymbol{p}}|^2 + \frac{|u_{\boldsymbol{p}}|^2 + |v_{-\boldsymbol{p}}|^2}{e^{\beta\epsilon(p)} - 1}) \tag{2.32}$$

At $T = 0$, and so $\beta \to \infty$, the second term in the integral vanishes but there is still a finite leakage of particles with $\boldsymbol{p} = \boldsymbol{0}$ due to the first term in the previous equation, even if the occupation number $< b_{\boldsymbol{p}}^{\dagger} b_{\boldsymbol{p}} >= 0$. This fundamental leakage of atoms form the condensate is called quantum depletion.

For temperatures larger than zero, the quantum depletion is negligible compared to the thermal depletion provided by the second term in the integral of Eq. 2.32. Using Eq. 2.23, it possible to evaluate the averaged number of real particles with $\boldsymbol{p} \neq \boldsymbol{0}$ due to quantum depletion:

$$N_{\boldsymbol{p}}^{QD} = \frac{\frac{p^2}{2m} + gn}{2\epsilon(p)} - \frac{1}{2} \tag{2.33}$$

For small momenta, this quantity is equal to $\frac{\sqrt{mgn}}{2p}$ meaning that quantum depletion of an interacting BEC decreases as $1/p$. In the opposite limit of large momenta, it is possible to prove that quantum depletion is negligible because it goes to zero as $1/p^4$.

Thermal depletion has instead a different dependence on the momentum $\boldsymbol{p}$. In the limit of small momenta, it goes as:

$$N_{\boldsymbol{p}}^{ThD} = \frac{m k_B T}{p^2} \tag{2.34}$$

The divergence at small momenta is thus stronger than in the case of quantum depletion. For large momenta thermal depletion goes to zero according to $e^{-\beta\epsilon(p)}$.

The different dependence on the momentum has allowed to distinguish the two kinds of depletion in experiments [28, 29].

Integration of Eq. 2.32 gives at $T = 0$:

$$N_0 = N(1 - \frac{8}{3\pi}(na^3)^{1/2}) \tag{2.35}$$

which means that the quantum depletion of the BEC depends on the same parameter $\sqrt{na^3}$ of the LHY in Eq. 2.28.

2.2 Quantum droplets of Bose-Bose mixtures

In this section, I will describe the mechanism allowing for the formation of self-bound liquid droplets in an ensemble of bosonic atoms. I will first discuss the general conditions an atomic system needs to fulfill to form a liquid-like droplet, introducing a simplified toy model for a quantum liquid (Sec. 2.2.1). I will then describe how these requirements can be satisfied by considering the realistic case of an attractive Bose-Bose mixture (Sec. 2.2.2) and I will report the analytical description of the resulting quantum droplet (Sec. 2.2.3), as first introduced in [5]. Finally, I will discuss the excitation spectrum of the droplet (Sec. 2.2.4) and some information we can deduce from a simplified model of it, based on a gaussian ansatz for its wavefunction (Sec. 2.2.5).

2.2.1 Toy model for a quantum liquid

The idea first introduced in [30] to create a liquid-like state in an ultracold atomic sample started from a simple assumption. Consider the mean-field and LHY energy terms introduced in the previous sections and assume that there exist a situation where they have opposite signs. Consider in particular the case where the mean-field energy is negative and the LHY is positive. The energy density will then correspond to:

$$e(n) = -\frac{1}{2}\alpha n^2 + \frac{2}{5}\beta n^{5/2} \tag{2.36}$$

where the two parameters $\alpha > 0$ and $\beta > 0$ depend on the microscopic interactions in the system.

From the energy density $e(n)$ it is possible to derive some thermodynamics properties. The chemical potential is given by:

$$\mu = \frac{de(n)}{dn} = -\alpha n + \beta n^{3/2} \tag{2.37}$$

The pressure is:

$$P = -e(n) + n\frac{de(n)}{dn} = -\frac{1}{2}\alpha n^2 + \frac{3}{5}\beta n^{5/2} \tag{2.38}$$

In order to have a stable liquid one needs $P = 0$, which occurs for $n_0 = (\frac{5\alpha}{6\beta})^2$ that is larger than zero.

Evaluating the chemical potential at this density, we get:

$$\mu(n_0) = -\frac{1}{6}n_0\alpha < 0 \tag{2.39}$$

A negative chemical potential is also a necessary condition for a self-bound state, because it prevents the system from evaporation. A final condition is that the resulting state is stable against collective excitations, which corresponds to: $c^2 > 0$, where c is the speed of sound. Using definition of compressibility and Eq. 2.10, we get:

$$mc^2 = (\frac{dP}{dn})_{n=n_0} = \frac{1}{4}n_0\alpha > 0 \tag{2.40}$$

We conclude that a system governed by the energy density of Eq. 2.36 fulfills all the requirements necessary for the realization of a quantum liquid. As already said, in a single component BEC the toy model presented here cannot be implemented: even if the MF and the LHY terms have the proper dependence on density, they always have the same sign.

A different situation occurs in a bosonic mixture. As Petrov pointed out in his proposal from 2015 [5], under certain conditions the two energy terms can have opposite signs and thus give rise to a liquid phase.

2.2.2 Bose-Bose mixture

In this section we will extend the results previously shown in Sec 2.1 for a single component BEC to the case of a mixture. We will also discuss the specific situation where we can recover the same energy density as in the toy model of Eq. 2.36. Let us start from the MF contribution. For a mixture, the MF density can be written as:

$$e_{MF}(n_1, n_2) = \frac{1}{2}g_{11}n_1^2 + \frac{1}{2}g_{22}n_2^2 + g_{12}n_1n_2 \qquad (2.41)$$

where $n_{1,2}$ are the densities of each species, g_{ii} the intraspecies coupling constant describing the interaction between atoms belonging to the same speci, while g_{12} describes the interspecies interaction. When all interactions are repulsive, two different phases could occur: the miscible regime, when $g_{12} < g$ ($g = \sqrt{g_{11}g_{22}}$), where the wavefunctions of the two species are overlapped and immiscible regime, when $g_{12} > g$ ($g = \sqrt{g_{11}g_{22}}$), where instead they are separated. Both regimes have been experimentally observed for example in [31, 32]
Following [5] we will consider a mixture with positive intraspecies interactions, $g_{11} > 0$ $g_{22} > 0$, and attractive interspecies interaction, $g_{12} < 0$. In this case the MF energy is positive, and thus the mixture is stable, only if $|g_{12}| < g$. We consider the unstable case, where the MF energy is slightly negative. we will consider a system with a slightly negative MF energy. We can introduce $\delta g = g_{12} + g < 0$, and we take the case where it is small, i.e. $\delta g << g$. Using this definition, we can rewrite the MF energy density as:

$$e_{MF}(n_1, n_2) = -|\delta g|(n_1n_2) + g(n_1^2 - \frac{a_{22}}{a_{11}}n_2^2) \qquad (2.42)$$

The second term in the MF energy is minimized if the two species have the same density, modulo a scale factor, i.e $n_2 = \sqrt{a_{11}/a_{22}}n_1 = \gamma n_1$, while the first term is minimized if $n_1 + n_2 \to \infty$, which corresponds to a collapse of the condensate. We can rewrite all the energy density in terms of a total density $n = n_1 + n_2$ and of the parameter γ. Assuming that the densities of the two clouds satisfy the condition $n_2 = \gamma n_1$, the second term in Eq. 2.42 vanishes, and we obtain:

$$e_{MF}(n) = -|\delta g|\frac{\gamma}{(1 + \gamma)^2}n^2 \qquad (2.43)$$

The generalization of the LHY term to the case of a mixture case is not trivial. Here I just report the results of the calculation, referring the interested reader to more technical papers [33]. The LHY energy term for a homonuclear mixture is given by [5]:

$$e_{LHY}(n_1, n_2) = \frac{8m^{3/2}}{15\pi^2\hbar^3}\sum_{\pm}\left(g_{11}n_1 + g_{22}n_2 \pm \sqrt{(g_{11}n_1 - g_{22}n_2)^2 + 4g_{12}^2n_1n_2}\right)^{5/2} \qquad (2.44)$$

Note that imposing $n_1 = n_2$, $g_{11} = g_{22}$ and $g_{12} = 0$, we can obtain the result already discussed for a single species.
In the mean-field unstable regime, $g_{12} + \sqrt{g_{11}g_{22}} < 0$ the square root in Eq. 2.44 satisfies the inequality:

$$\sqrt{(g_{11}n_1 - g_{22}n_2)^2 + 4g_{12}^2n_1n_2} > n_1\sqrt{g_{11}^2 + 2\gamma g_{11}g_{22} + \gamma^2 g_{22}^2} = n_1(g_{11} + \gamma g_{22}) \qquad (2.45)$$

which means that the term with the minus sign in the sum $\sum_{\pm}$ of Eq. 2.44 is negative, adding an imaginary term to the LHY energy.

In order to solve this problem we use the same approximation discussed in [5]. In the limit of $|\delta g| << g$ we can neglect the small δg corrections and set, just for the LHY term, $g_{12} = \sqrt{g_{11}g_{22}}$. In this limit the energy density provided by the LHY correction is given by:

$$e_{LHY}(n_1) = \frac{8m^{3/2}}{15\pi^2\hbar^3}(g_{11}n_1 + g_{22}n_2)^{5/2} \qquad (2.46)$$

If we assume again that the two densities are the same modulo a scale factor provided by the minimization of the MF energy, we can simplify the last equation obtaining:

$$e_{LHY}(n) = \frac{8m^{3/2}}{15\pi^2\hbar^3}(\gamma g_{22})^{5/2}n^{5/2} \qquad (2.47)$$

In this limit, since the MF and the LHY energy densities have a different sign, the Bose-Bose mixture fulfills the conditions introduced in Sec. 2.2.1 and thus creates a liquid-like state. From Eqs.2.43 and2.47 we can derive the two parameters α and β of Eq. 2.36:

$$\alpha = \frac{2|\delta g|\gamma}{(1+\gamma^2)} \qquad (2.48)$$

$$\beta = \frac{2m^{3/2}}{3\pi^2\hbar^3}(\gamma g_{22})^{5/2} \qquad (2.49)$$

Both of them depend only on the inter and intra-species interactions that can be tuned, in the presence of suitable Feshbach resonances, with an external magnetic field. Evaluating the expected equilibrium density $n_0 = (\frac{5\alpha}{6\beta})^2$ and multiplying it for $\gamma/(1+\gamma)$ and $1/(1+\gamma)$ respectively, we obtain the equilibrium densities n_1 and n_2:

$$n_i^0 = \frac{25\pi}{1064}\frac{|\delta g|^2}{a_{11}a_{22}\sqrt{a_{ii}}(\sqrt{a_{11}}+\sqrt{a_{22}})^5} \qquad (2.50)$$

which correspond to the results of [5].

2.2.3 Analytical solution

Following Petrov [5], we can define the wave function of each species as:

$$\Psi_i(r,t) = \sqrt{n_i}\phi(r,t) \qquad (2.51)$$

where $\phi(r,t)$ is a scalar wave-function common to both species. It is convenient to work using adimensional coordinates $\tilde{r} = r/\xi$ and $\tilde{t} = t/\tau$, where:

$$\xi = \sqrt{\frac{3}{2}\frac{\sqrt{g_{22}}+\sqrt{g_{11}}}{m|\delta g|\sqrt{g_{11}}n_1^0}} \qquad (2.52)$$

and

$$\tau = \hbar\frac{3}{2}\frac{\sqrt{g_{22}}+\sqrt{g_{11}}}{|\delta g|\sqrt{g_{11}}n_1^0} \qquad (2.53)$$

The energy density of the droplet is given by [5]:

$$\epsilon(\phi) = \frac{1}{2}|\nabla_{\tilde{r}}^2\phi|^2 - \frac{3}{2}|\phi|^4 + |\phi|^5 \qquad (2.54)$$

where $\hbar = m = 1$.

The scalar wave-fuction of the ground state can be obtained by solving a Gross-Pitaevskii equation in the adimensional units for $\phi(\tilde{t}, \tilde{t}) = \phi_0(\tilde{r})$:

$$\mu\phi_0(\tilde{r}) = (-\frac{1}{2}\nabla^2 - 3|\phi_0(\tilde{r})|^2 + \frac{5}{2}|\phi_0(\tilde{r})|^3)\phi_0(\tilde{r}) \qquad (2.55)$$
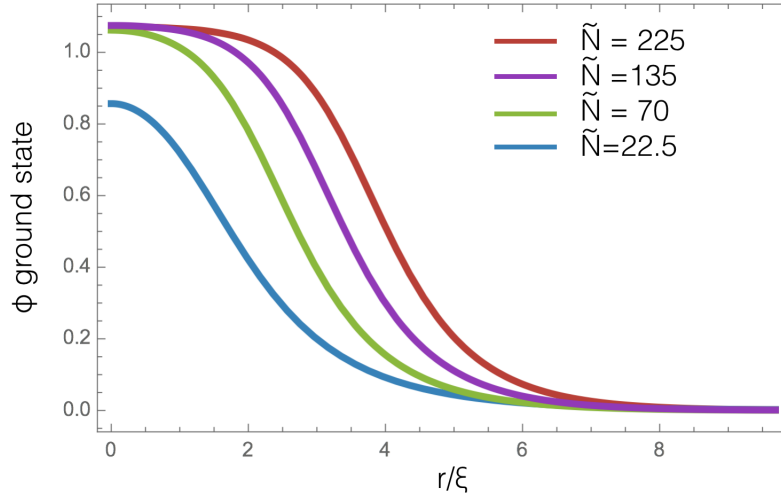
Figure 2.1: Ground state wavefunction of the droplet for different values of $\tilde{N}$. For large atom numbers the pick density saturates to a fixed value, giving rise to a flat-top bulk.

The chemical potential is fixed by the normalization condition: $\tilde{N} = \int |\psi_0|^2 d^3\tilde{r}$. $\tilde{N}$ is related to the actual atom number by:

$$N_i = n_i^0 \xi^3 \tilde{N}_i \tag{2.56}$$

Some examples of the ground state wave-functions obtained for different values of $\tilde{N}$ are reported in Fig. 2.1. For small $\tilde{N}$ the shape of the wave-function is similar to a gaussian while, for large $\tilde{N}$, the ground state of the mixture is a spherical droplet of radius $\tilde{R} \simeq (3\tilde{N}/4\pi)^{1/3}$ which displays a flat-top shape indicating a saturation density in the bulk.

Knowing the ground state wave-function, it is possible to evaluate the binding energy of the droplet as a function of $\tilde{N}$. In the adimensional units, this quantity is given by $\tilde{E} = \int \epsilon(\psi_0) d^3\tilde{r}$. In Fig. 2.2 it is reported how the binding energy changes as a function of the atom number in the droplet.

Given the liquid-like nature of this self-bound droplet, we can write its total energy by introducing the so-called liquid drop model, already used for example in the context of the liquid Helium [34, 14]:

$$\frac{E(N)}{N} = E_B + E_S N^{-1/3} + E_C N^{-2/3} \tag{2.57}$$

The first term is called bulk energy. It provides a contribution proportional to N and is the dominant term in the expansion. The coefficient associated E_B to it is negative because the binding energy of a self-bound state is negative. The first correction to it is the surface energy which is proportional to $N^{2/3}$. This contribution is typically positive $E_S > 0$ because breaking the bulk has an energy coast. The surface tension can be calculated from the coefficient E_S. The last term in the model, the curvature term, is the one with less physical meaning. In the limit of small atom number is primarily determined by the energies of small drops whose central density is smaller than the liquid density. Note indeed that it is the smallest one and for a droplet in equilibrium is typically negligible but negative $E_C < 0$. If we are considering an excited system it can assume also positive sign and in this case it is related to convexity of the surface.

By fitting $\tilde{E}(\tilde{N})$ in Fig. 2.2 with the energy functional of Eq. 2.57 with E_B, E_S and E_C as free parameters we note that the model well approximates the behavior of $\tilde{E}(\tilde{N})$ in the whole range of $\tilde{N}$. However, the three terms in Eq. 2.57 have a clear physical interpretation only in the large $\tilde{N}$ regime, where the distinction between the bulk and the surface is evident. Recently a similar approach has been used also in the study of a quantum droplet [35].

In classical liquids the quantity E_S is related to the surface tension of the droplet σ by $\sigma = E_S/(4\pi r_0^2)$, where r_0 is the unit radius of the liquid and it is defined as

$$r_0 = [\frac{5}{3}\langle r^2(N)\rangle]^{1/2}N^{-1/3} \tag{2.58}$$

where $\langle r^2(N)\rangle$ is the mean-square radius of the cluster, i.e. $\int d^3r|\psi(r)|^2r^2$.

From the fit in Fig. 2.2 we get $E_B \simeq -0.57$, $E_S \simeq 1.89$ and $E_C \simeq -0.81$.

In Fig. 2.2 we also observe that for $\tilde{N} < 22.55$ the binding energy becomes positive,
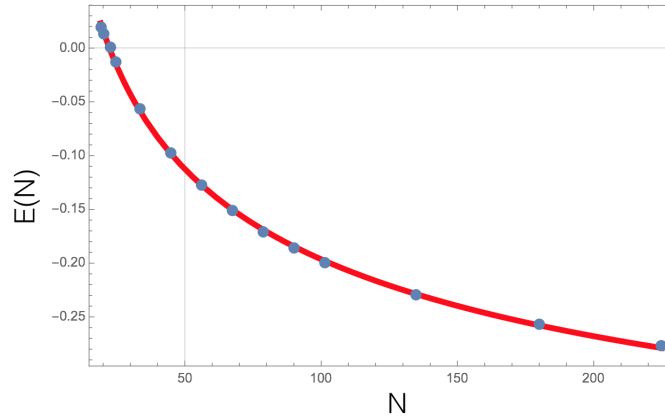

Figure 2.2: Droplet binding energy as a function of the atom number calculated as $\tilde{E} = \int \epsilon(\psi_0)d^3\tilde{r}$ (blue dots), in adimensional units. The red is a fit of the blue dots with the liquid droplet model of Eq. 2.57.

meaning that a self-bound droplet is no more a stable solution. For $18.65 < \tilde{N} < 22.55$ the droplet can exist as a metastable state, while for $\tilde{N} < 18.65 = \tilde{N}_C$ the droplet cannot form at all. This behavior can be understood qualitatively by looking at the dependence of the different energies contributions on the size of the cloud and on the atom number $\tilde{N}$. The kinetic energy scales as $E_{kin} \propto N/R^2$, the MF contribution as $E_{MF} \propto -N^2/R^3$, while $E_{LHY} \propto -N^{5/2}/R^{9/2}$. As I show in Fig. 2.3, as $\tilde{N}$ decreases, the minimum of $E(R)$, corresponding to the droplet, first becomes positive and the global minimum of $E(R)$ occurs at $R \to \infty$, where $E(R \to \infty) = 0$: in this situation the droplet is a metastable states. For even smaller atom numbers, the energy minimum at finite R disappears and the self-bound state cannot exist.
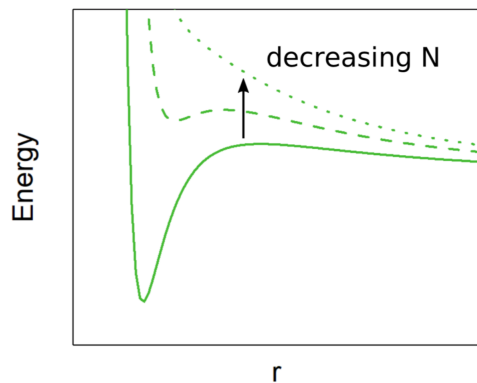

Figure 2.3: E(R) for different values of $\tilde{N}$. Decreasing the atom number the system passes from a self-bound regime to a metastable one and then the liquid-like state disappears.

2.2.4 Excitation spectrum

One of the most fascinating and peculiar properties of quantum droplets deals with their excitation spectrum. In particular, it is interesting to compare the excitation modes with the particle emission threshold, provided by the chemical potential with the opposite sign $-\tilde{\mu}$. This quantity represents the energy gained by the system by releasing a particle. Due to the liquid-like nature of the quantum droplet, $\tilde{\mu} < 0$ and so the particle emission threshold is positive. Note that, according to the liquid drop model, the chemical potential is given by:

$$\tilde{\mu} = E_B + \frac{2}{3}\frac{E_S}{\tilde{N}^{1/3}} + \frac{1}{3}\frac{E_C}{\tilde{N}^{2/3}} \tag{2.59}$$

In the limit of large atom numbers it goes asymptotically to $E_B \simeq -1/2$, which also highlights the liquid-like nature of the system.

In order to study the small-amplitude excitations, Petrov [5] solves the Bogoliubov-De Gennes equation obtained from the linearization of the GPE in Eq. 2.55. In this way one can calculate the energies of the collective exciations of the droplet, like the monopole, quadrupole and the oscillations with increasing angular momenta.

The results are reported in Fig. 2.4. In the limit of large N, where the droplet enters the incompressible regime, the excited states are expected to be surface modes (ripplons) and so we can try to compare the results introduced above, with those obtained using the classical results from the physics of liquid droplets and evaluated from the surface tension [36]:

$$\omega_l = \sqrt{\frac{4\pi}{3}l(l-1)(l+2)\frac{\tilde{\sigma}}{\tilde{N}}} \tag{2.60}$$

where $l > 0$ is the angular momentum. The $l = 1$ mode refers to the dipolar mode, i.e. to a center of mass displacement of the droplet, and thus $\omega_1 = 0$. The $l = 0$ mode represents the monopole mode and it cannot be calculated using Eq. 2.60, since it is a classical result not valid in the limit of incompressible droplet [36]. The modes calculated with Eq. 2.60 are reported in Fig. 2.4 as the thin-dotted lines. Note that again we can use the results of the liquid drop model to get the surface tension, obtaining essentially the same results of Petrov. The two approaches give similar results for the surface modes, suggesting the liquid-like nature of quantum droplets in the large N regime. As we can see from Fig. 2.4, for a stable droplet with $(\tilde{N} - \tilde{N}_C)^{1/4} > 1.5$, the particle emission threshold is smaller than any excitation mode up to $(\tilde{N} - \tilde{N}_C)^{1/4} \simeq 3$, which corresponds to $\tilde{N} \simeq 100$, where $-\tilde{\mu}$ becomes equal to the quadrupole mode.

The peculiar relation between the excitation modes and the particle emission threshold gives rise to the phenomenon of self-evaporation. In the limit of small atom number, the droplet prefers to expel any excitations loosing atoms instead of occupying an excited state. The droplet is thus an auto-evaporating object, since it has an internal mechanism to dissipate energy and reach zero temperature. This property paves the way to a possible use of the quantum droplet as a coolant for other system. The experimental observation of this is still missing and it represents one of the most interesting perspectives in the investigation of quantum drops. We will discuss again some aspects about self-evaporation in Section 2.3, making use of a numerical simulation that is able to capture the dynamics of the system.

2.2.5 Gaussian Ansatz

An alternative way to derive the equilibrium properties of the droplet is to use a gaussian ansatz (GA) for the wave-function of the ground state. This approach has been recently used to described the oscillation mode of a droplet confined in a quasi-1D waveguide [37]. In this approximation we can write the density of the system as:

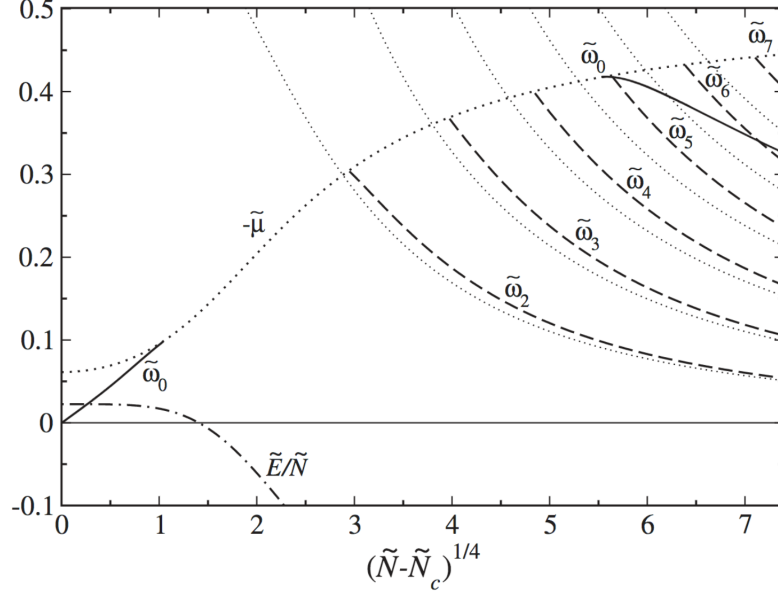$$n(r) = Ae^{-r^2/(2\sigma^2)} \tag{2.61}$$

Figure 2.4: The dash-dotted line corresponds to the energy per particle $\frac{\tilde{E}}{\tilde{N}}$ analogously to the one reported in Fig. 2.2. The thick dotted line represent $-\tilde{\mu}$, i.e. the particle emission threshold. The solid line is the monopole mode ω_0, while the dashed are the higher angular momentum modes ω_l. The thin dotted lines are the corresponding modes calculated with the surface modes approximation of Eq. 2.60. All these quantities are plotted as a function of $(\tilde{N} - \tilde{N}_C)^{1/4}$. Image taken from [5].

where A is a normalization constant. Its value is fixed the normalization condition N_{at} , i.e. $\int_0^\infty An(r)4\pi r^2 dr = N_{at}$. Solving for A we get:

$$n(r) = \frac{N_{at}}{2\sqrt{2}\pi^{3/2}\sigma^3}e^{-r^2/(2\sigma^2)} \tag{2.62}$$

We assume that the associated wave-function is $\psi(r,t) = \sqrt{n(r,t)}$ without considering phase terms which are not relevant in the study of the equilibrium properties of the system. From the definition of $n(r)$ we can simply evaluate the kinetic energy functional:

$$E_{kin}(\sigma, N_{at}) = -\frac{\hbar^2}{2m}\int_0^\infty 4\pi\psi(r)\frac{d}{dr}(r^2\psi'(r))dr = \frac{3\hbar^2 N_{at}}{4m\sigma^2} \tag{2.63}$$

To calculate the MF and LHY terms we insert the gaussian ansatz for n in Eq.s 2.43 and 2.47. We can prove that:

$$E_{MF}(\sigma, N_{at}) = -\frac{\gamma}{(1+\gamma)^2}|\delta g|\frac{N_{at}^2}{8\pi^{3/2}\sigma^3} \tag{2.64}$$

and

$$E_{LHY}(\sigma, N_{at}) = \frac{8m^{3/2}}{15\pi^2\hbar^3}(\gamma g_{22})^{5/2}\frac{N_{at}^{5/2}}{5\sqrt{5}2^{3/4}\pi^{9/4}\sigma^{9/2}} \tag{2.65}$$

Where again we assume $n_2 = \gamma n_1$ and $\gamma = \sqrt{g_{11}/g_{22}}$. The total energy functional as a function of σ and N_{at} is the sum of the Eq.s 2.63 2.64 2.65. To study the equilibrium properties using a gaussian approximation, we proceed as follows. At a specific value of the magnetic field and thus of the coupling constants g_{ij}, we search the value of $\sigma_0(N_{at})$ that minimizes $E_{tot}(\sigma, N)$ for different values of N_{at}. As expected, we find that the energy minimum is negative for atom numbers larger than a critical number N_C. We define N_C

imposing $E_{tot}(N_C, \sigma_0(N_C)) = 0$. We repeat the same procedure for different values of the magnetic field. To compare the results obtained with the gaussian approximation with those reported in the previous section from the analytical solution by Petrov, we need to convert the latter in dimensional units. Using Eq. 2.56 and considering $\tilde{N}_C = 22.55$, we find:

$$N_C(B) = \xi(B)^3 (n_1^0 + n_2^0) 22.55 \tag{2.66}$$

The width of the gaussian density is related to the Petrov's radius $\tilde{R}$ by:

$$\sigma_0(B) = \frac{\tilde{R}\xi(B)}{\sqrt{2}} = \xi(B)\left(\frac{3\tilde{N}}{4\pi}\right)^{1/3}\frac{1}{\sqrt{2}} \tag{2.67}$$

where the factor $1/\sqrt{2}$ is provided by the fact that the half width at $1/\sqrt{e}$ of the denisty profile is $\sqrt{2}$ times smaller than that of the the wave-function, corresponding to $\tilde{R}$. The comparison between the GA and analytical results is shown in Fig. 2.5 for the critical atom number and $\sigma_0(N_C)$.

The agreement between the two models is very good: the equilibrium properties of the
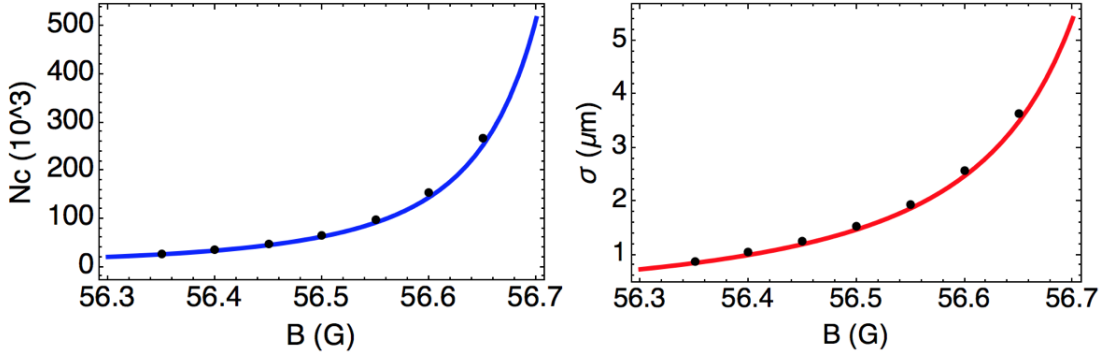

Figure 2.5: Comparison between the gaussian ansatz (black dots) and the solutions provided by Petrov (continued lines) for the critical atom number N_C (left) and the size $\sigma_0(N_C)$ (right) for different values of the magnetic field.

droplet are then well reproduced by a simple gaussian Ansatz model. The agreement is expected to get worse as the atom number increases and the droplet wave-function deviates from the gaussian shape.

2.3 Numerical simulations of the quantum droplet

Both the analytical model by Petrov and the GA solution introduced so far, were used to describe the equilibrium properties of the droplet. None of these models can describe the dynamical evolution of the droplet that we observe in the experiment. For this reason, in collaboration with prof. Michele Modugno, we developed a numerical simulation able to reproduce the dynamics of the experiment. The evolution of the mixture is described by solving numerically a system of coupled GP equations modified by the addition of the LHY term as discussed in [5]:

$$i\hbar\frac{\delta\psi_j}{dt} = \left(-\frac{\hbar^2}{2m}\nabla^2 + V_{ext} + \mu_i(n_1, n_2)\right)\psi_j \tag{2.68}$$

where ψ_j is the wave-function describing the j-th hyperfine level and μ_i the associated chemical potential:

$$\mu_i = \frac{\delta e_i}{\delta n_i} = g_{ii}n_i + g_{12}n_j + \frac{\delta e_{LHY}}{\delta n_i} \tag{2.69}$$

Using the LHY energy density evaluated in the limit of $|\delta g| \ll g$, we can prove that:

$$\frac{\delta e_{LHY}}{\delta n_i} = \frac{32}{3\sqrt{\pi}} g_{ii}(a_{ii}n_i + a_{jj}n_j)^{3/2} \tag{2.70}$$

This approach is valid in the limit of the local density approximation. The latter has been recently considered for the description of the formation of macroscopic quantum droplets in dipolar condensates [38, 39, 40].

In Chapter 4 we will use the numerical simulations to understand the dynamical evolution of the droplet observed in the experiment. In this section, I will use them to better understand some properties of the droplet, in comparison with the models introduced above.

First of all, I can evaluate the equilibrium size of the droplet, defined as the radius at $1/\sqrt{e}$ of the density profile, for different values of the atom number. In Fig. 2.6 I compare the results obtained from the simulation with the one predicted by the GA (black curve) and Petrov's analytical theory (green line). As we can see, the size of the system obtained is well described by the GA for atom numbers smaller then 200×10^3 atoms, i.e., 5 times the critical atom number. When, increasing the atoms numbers, the results deviate from the GA prediction and converge the droplet radius predicted by Petrov for the large N regime.
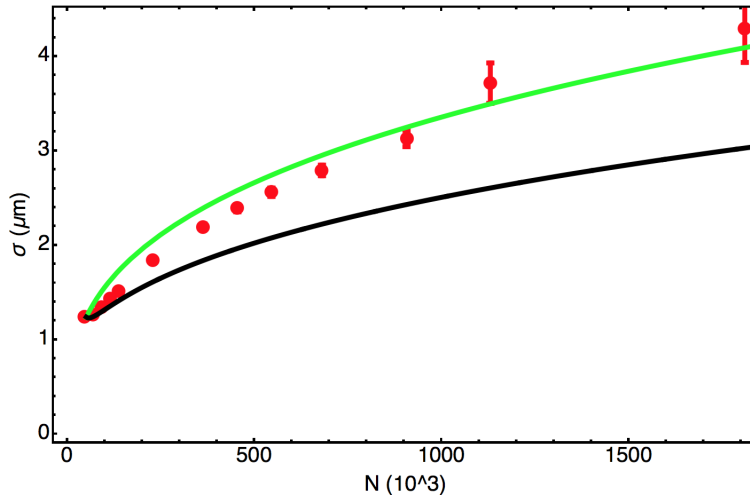

Figure 2.6: Red dots: σ obtained from the simulation using different atom number measured as the distance from the center such that the density assumes a value that is $n_0 e^{-1/2}$ where n_0 is the density at $r = 0$. Black curve: $\sigma(N)$ evaluated using the gaussian ansatz explained in the previous section. Green curve: $\sigma(N)$ according the Petrov's theory.

2.3.1 Monopole mode

The second aspect that numerical simulations can help us understand concerns with the peculiar features of the droplet excitation spectrum, as introduced in Sec. 2.2.4. I performed some simulations preparing the mixture out of its equilibrium configuration, i.e. at a size larger than the radius of its ground-state, and looked at its dynamical evolution. If the initial state maintains its spherical symmetry, we expect that the out-of-equilibrium preparation excites a monopole mode in the droplet. We indeed observe an oscillation in the radius of the droplet which gets damped after a certain time, indicating the effect of the self-evaporation mechanism discussed above. We report in Fig. 2.7 the evolution of $\sigma(t) - \sigma_0(\tilde{N})$, where $\sigma_0(\tilde{N})$ is the equilibrium size of a droplet with $\tilde{N}$ atoms, as a function of time for an atom number that is 30, 40 and 50 times the critical one. I fit the data using a damped sinusoidal

function $Ae^{-t/T}\sin[2\pi ft]$. For $N \simeq 40N_C$ Petrov's theory predicts that the monopole mode should become energetically favorable with respect to the particle emission threshold. For this reason, the damping coefficient T becomes larger as N increases (see Fig. 2.8).

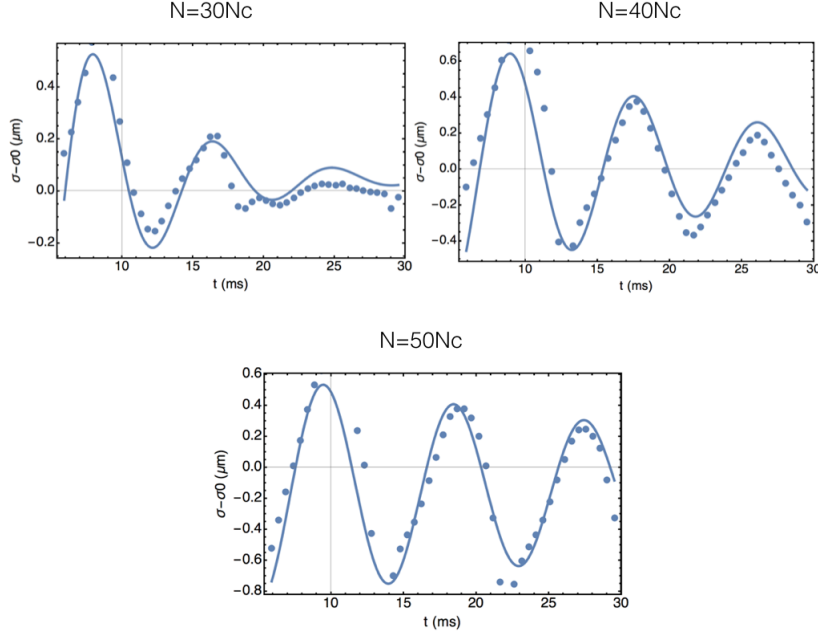We can try to be more quantitative using the adimensional units. The oscillation frequency

Figure 2.7: Monopole oscillation of a quantum droplet. Is there reported for N=30, 40 and 50 N_C the temporal evolution of $\sigma(t) - \sigma_0(\tilde{N})$. The atom number crosses the point where the monopole mode becomes energetically favorable respect to the particle emission threshold. The crossover between this two regimes is highlighted by the increasing of the damping coefficient.

obtained from the fit previously introduced can be converted in $\tilde{\omega}$ as:

$$\tilde{\omega} = \nu 2\pi \tau(B) \tag{2.71}$$

while the damping coefficient is simply $\tilde{T} = T/\tau(B)$. In Fig.2.8 I report the monopole mode frequency $\tilde{\omega}_{mono}$ and the relative damping rate as a function of $\tilde{N}$. The red curve on the left panel represents the particle emission threshold $-\mu$ evaluated using the Liquid Drop Model explained before. One can see that, when $\tilde{\omega}_{mono}(\tilde{N}) \simeq \tilde{\mu}(\tilde{N})$, the damping coefficient increases exponentially.

We can interpret this damping mechanism as a genuine consequence of self-evaporation. Since for $\tilde{N} < 45\tilde{N}_C$ emitting particle is energetically favorable with respect to the monopole excitation, the droplet evaporates the excess of energy by expelling particles and thus the oscillation is damped. We can try to estimate the expelled atoms number using a simple energetic argument. Suppose to have a droplet made of $\tilde{N}$ atoms out of equilibrium so that the monopole mode is excited in a region where self-evaporation can occur. The total energy of the system is given by $\tilde{E}_{in} = \tilde{E}(\tilde{N}) + \tilde{\omega}(\tilde{N})$. Suppose for simplicity that the monopole frequency does not depend on the atom number. After the evaporation the system will be in equilibrium but with a smaller atom number: $\tilde{E}_{fi} = \tilde{E}(\tilde{N}')$ with $\tilde{N}' < \tilde{N}$. For energy conservation $\tilde{\omega}(\tilde{N}) = \tilde{E}(\tilde{N}) - \tilde{E}(\tilde{N}')$. From the definition of chemical potential, we can approximate the energy difference as $-\tilde{\mu}(\tilde{N})\Delta\tilde{N}$ and so: $\tilde{\omega}(\tilde{N}) = -\tilde{\mu}(\tilde{n})\Delta\tilde{N}$. In first approximation, we can thus conclude that the expelled atoms are given by:

$$\Delta\tilde{N} = -\frac{\tilde{\omega}_{mono}(\tilde{N})}{\mu(\tilde{N})} \tag{2.72}$$

In the region where self evaporation occurs this quantity is larger but of the same order of 1. Since the critical atom number is 22.5, we can conclude that the atom lost for self evaporation is of the order of one percent of the starting atom number.
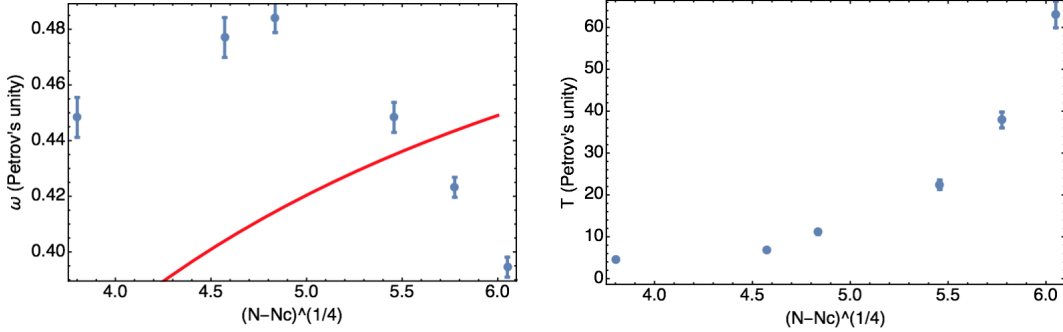

Figure 2.8: On the left: blue dots represent $\tilde{\omega}_{mono}$ for different atom number while the red line is the particle emission threshold calculated using the Liquid Droplet Model. On the right: the simulated damping time as a function of N.

2.3.2 Three-body losses

In order to reproduce the behavior of our experimental system, in the numerical simulations we also introduce a term describing three-body recombination effects. These can be modeled by adding to the Hamiltonian a purely imaginary, phenomenological loss term:

$$H_{3BL} = -i\frac{\hbar K_{111}}{2}|\psi|^4 \tag{2.73}$$

where K_{111} is the three body recombination coefficient. This kind of approach has been used successfully to describe the collapse of dipolar BEC [41]. Three-body losses leads to a non-unitary dynamics where the wave function decay as

$$\frac{d}{dt}\int_V |\psi|^2 = -K_{111}\int_V |\psi|^6 \tag{2.74}$$

so proportionally to the density to the third power. This picture is correct assuming that the products of recombination collisions leave the cloud without interacting with the remaining atoms, i.e. neglecting the avalanche terms [42]. Indeed this term affects the losses in a dense system and in principle could play an effect even in our system. A detailed comparison between the simulated and the experimentally observed dynamics will be presented in Chapter 4.

2.4 Quantum droplets in dipolar gases

In this section we will shortly introduce some concepts about another similar self-bound system, stabilized by perturbative corrections to the MF energy, i.e. dipolar droplets, that are actually the first kind of quantum droplets observed in experiments. In addition to the usual contact interaction $V_C = \frac{4\pi\hbar^2 a}{m}$, dipolar BECs possess another interaction channel, i.e. the dipolar interaction:

$$V_{dip} = \mu_0\mu^2\frac{1 - 3\cos^2(\theta)}{4\pi r^3} \tag{2.75}$$

where μ_0 is the vacuum polarizability and θ is the angle between the direction of the polarizability μ and the position between the dipoles r [43]. Dipolar systems are then characterized

by two different length scales: the contact scattering length a and a length scale associated to the dipolar interaction $a_{dd} = \frac{m\mu_0\mu^2}{12\pi\hbar^2}$. The ratio between these two quantities is defined as $\epsilon_{dd} = a_{dd}/a$. The presence of these two different interaction terms, makes it possible to have a situation analogous to that of attractive bosonic mixture, where the MF and LHY energies have opposite signs. The role of the attractive inter-species interaction is here taken over by the dipole interactions when the dipoles are properly oriented, while the repulsive term is provided by the contact interaction.

It is possible to prove that the MF energy scales as:

$$E_{MF} \propto \frac{gn_0^2}{2}(1 - \epsilon_{dd}f(k)) \tag{2.76}$$

where $f(k)$ is a function of the aspect ratio k of the atomic cloud and n_0 is the averaged density. Fixing the value of the magnetic field, and thus of g, it is possible to change the MF interaction by opportunely tuning the aspect ratio of the trap. The MF energy can then be made arbitrarily small and negative, so that the interplay with the repulsive LHY term can arrest the collapse [41], this mechanism generates the quantum droplet. Note that in dipolar gases the LHY correction maintains the same dependence on the density and on the contact scattering length introduced in Section 2.1.1 [44]:

$$E_{LHY}(0) = \frac{128}{15\sqrt{\pi}}\sqrt{na^3}Q_5(\epsilon_{dd}) \tag{2.77}$$

where Q_5 depends only on ϵ_{dd}.

Dipolar droplets have been observed with both Dysprosium [8, 6] and Erbium [9] BECs. The main difference between the dipolar droplet and Bose-Bose mixture droplet is the shape of the ground state wave-function. Indeed, due to the anisotropic nature of dipolar interaction, the dipolar droplet is elongated in one direction differently from the Bose-Bose mixture droplet which is spherical. This difference strongly modifies the excitation spectrum of the two. Several properties of quantum dipolar droplets have been investigated by the group of Tilman Pfau in Stuttgart [8, 6, 7, 45, 46, 47, 48]. Here we will only report the most relevant results in comparison with our experiment.

One remarkable measurement performed with dipolar droplets concerns the validation of the stabilization mechanism provided by the LHY correction with respect to a different one proposed in [4] and [49], which relies on the interplay between two and three body interactions. The two stabilization mechanisms predict different equilibrium densities for the droplet and thus different lifetimes due to the three-body losses. Comparing the measured lifetimes with the predicted one, the authors confirm that the stabilization mechanism responsible for the formation of self-bound droplets is the one provided by the LHY correction [7].

Another peculiar property of dipolar quantum droplets, is the capability to create self-organized states. It has been shown both theoretically [50] and experimentally [45], that, increasing the harmonic confinement along the direction of the dipoles, the ground state of the system passess from a single droplet to multiple-droplets. This observation arises questions about the possible super-solid nature fo this state. Super-solids are characterized by a self-organized ground state with a periodic density profile that does not perturb the large scale coherence. Similar system have been observed making use of solid Helium [51] and recently also in the context of ultracold atoms [52, 53]. Even if dipolar quantum droplets manifest a self-organized density profile, the authors could not observe any coherence from a ToF expansion of the multiple droplet. This can be explained by the fact that the condensate undergoes a modulation instability and for this reason the system is in an excited state. The ground states could in principle manifest such super-solid behavior [50]. In a similar experiment but, using a different trapping potential, it was recently observed coherence between different stripes [54].

Collisions between dipolar quantum drops have also been investigated. Several quantum droplets are created in a waveguide, with the dipoles perpendicular to the the propagation direction that creates the laser beam used for the waveguide. Applying an additional harmonic confinement along the longitudinal direction of the waveguide, the droplets get closer to each others. In this configuration one observes that the repulsive inter-droplet interactions induces oscillations of the droplets inside the waveguide [46]. This oscillation is a direct consequence of the repulsive dipolar droplet-droplet interaction and thus such collisions, differently from the case we will consider, do not bring any information about the physics of quantum droplets.

A very fascinating possibility would be to create a system in which both the discussed stabilization mechanism are present, i.e. an attractive mixture of dipolar gases. The occurrence of a self-bound state in such system has been recently proposed [55]. The candidate for the experimental realization of this new kind of droplet is the new Er-Dy experiment in Innsbruck [56].

Before concluding this section I would like to highlight that recently the existence of quantum droplets has been proved also in photon fluids [57, 58].

2.5 Collisions between self-bound objects

The second part of the experimental characterization of quantum droplets reported in this thesis concerns on the study of collisions between two droplets (Chapter 5). In this section I will report some of the results found in literature about the collisions between self-bound objects, which could help us as a guideline to understand the behavior observed in the collision of our quantum droplets.

Liquid drops. Collisions between classical liquid drops have been extensively studied from both an experimental and a theoretical point [59] of view. The first pioneering work was made by Rayleigh who considered the problem in order to explain the size distribution of rain drops [60]. More recently, the collsion between droplets has played an increasing important role in the study of formation of liquid jets [61] and in the understanding the physics of spays [62]. Several phenomena can occur when liquid drops collide: coalescence, i.e. the creation of a single macro-droplet starting from two; droplets bounce or droplets separation. The distinction between the different regimes depend on two main parameters: the Weber number We and the impact parameter b. The first one is defined as:

$$We = \frac{2\rho R v^2}{\sigma} \tag{2.78}$$

where ρ is the density of the droplet, R the radius, v the relative velocity between the colliding droplets and σ is the surface tension. It is possible to define a generalized Weber number $We^* = E_{kin}/Es$. The two definitions are connected by: $We^* = We/12$. The impact parameter b is defined as the ratio of the projection of the center-to-center line onto the direction perpendicular the relative velocity to the averaged droplet radius.

The typical phase diagram for the collision between classical droplets is reported in Fig. 2.9. The coalescence region is limited by an upper and a lower bound depending on the impact parameter b. For large b, separation occurs because the macro-droplet is unstable with respect to the rotational energy acquired in the impact. For this reason the separation is "off-center". In the opposite limit, for small values of the impact parameter, the formation of a single droplet is prevented for large We number by the excitation of large vibrational modes [63]. Considering the lower part of the phase diagram, close to $b = 0$, which is more relevant in comparison with our case, we can deduce that coalescence occurs if the kinetic energy of the collision is smaller then the energy scale defined by the surface tension, i.e., for sufficiently small value of We.
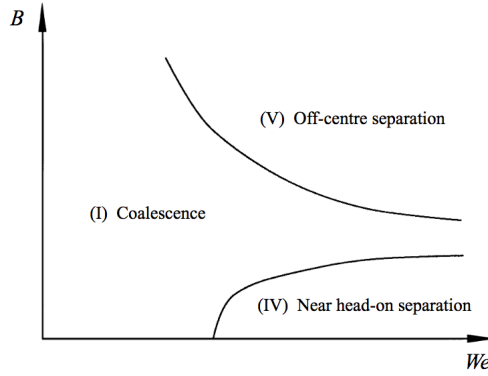
Figure 2.9: Results of the collision between two classical drops as a function of the We and of the impact parameter b. Image taken from [64]

Atomic nuclei. Similar studies have been carried out for understand the the dynamics of some nuclear reactions. As a matter of fact the most simple model to describe the binding energy of a nucleus is the so-called *liquid drop model* which is based on the famous Bethe-Weizsäcker formula. Within this model, the nuclear binding energy depends on five terms: the first three are the bulk, surface and curvature terms (in the nuclear case the latter is provided by the Coulomb interaction between protons), that can be found also in classical droplets. The fourth term comes from the Pauli exclusion principle, while the last term, called pairing term, takes into account the interaction between the spins of the nucleons. Using the liquid drop model, it is possible to partially describe several nuclear reactions, including fission, fusion of heavy nuclei and collisions between nuclei [65, 66].

The main difference between nuclear collisions and collisions between classical drops, is provided by the quantum nature of the nuclei. The two wave-functions representing the colliding nuclei, could have different (coherent) phases and in principle this could play a dynamical role, as it happens for instance in the Josephson effect. It has been recently discovered [67] that the initial phase difference between two colliding nuclei has a negligible role as the system becomes strongly interacting. When the two nuclei enter in contact, the authors observe the establishment of a common phase. This phase locking mechanism, attributed to the superfluid nature of the colliding objects, keeps the phases entangled even after the separation of the nuclei. In the opposite limit of a weakly interacting system, the initial phase plays instead a significant role [68] due to interference effects.

Matter − wave Solitons. Collisions between self-bound systems have been studied also in the context of ultracold gases, in particular making use of matter wave solitons. Solitons are localized solutions of a non-linear equation, that propagate without changing their shape, as a result of the interplay between the attractive mean field energy and the kinetic energy provided by the wave packet dispersion. Even if, by definition, a soliton exists only in a 1D system, it is possible to prove the existence of a bright soliton-like solution also in a cigar-shaped attractive BEC. Differently from the pure 1D case, the soliton-like solution displays a maximum critical atom number N_C above which the soliton-like system is unstable to collapse. In a pure 1D system, solitons are "stable" against collisions: they pass through each other without changing the amplitude of the wavefuction, the shape and the velocity. However the behavior observed during the collision depends on the phase difference between the two. For a phase difference $\Delta\phi \simeq 0$ is observed an antinode in the density profile as a result of a constructive interference between the colliding solitonic matter-wave. In the opposite case, $\Delta\phi \simeq \pi$, the interference is destructive and the antinode does not appear during the collision. This two different regimes were observed in [69] and they are reported in Fig. 2.11.
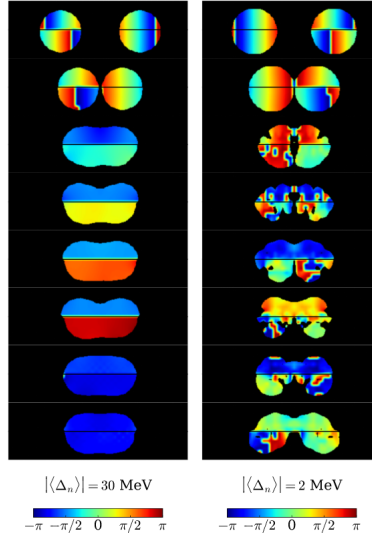
Figure 2.10: Collisions between two strongly interacting (left) and weakly interacting (right) nuclei. In the strongly interacting case it is possible to observe the phase-locking mechanism. Image from [67]

The situation changes dramatically when considering a BEC in a quasi 1D waveguide. In
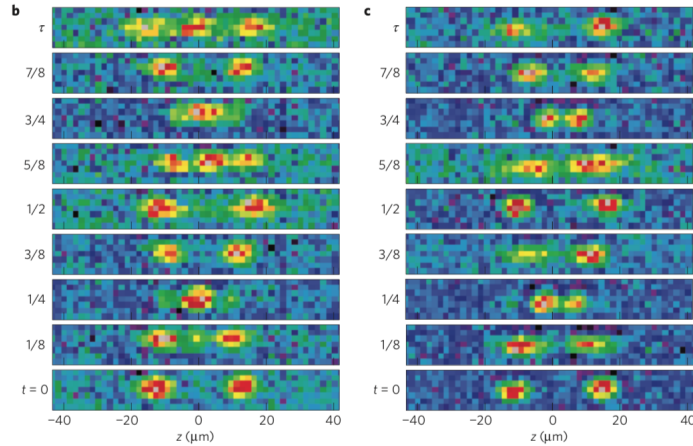

Figure 2.11: Right side: collision between bright solitons with $\Delta\Phi \simeq 0$. Left side: collision between solitons with $\Delta\Phi \simeq \pi$. Figure taken from [69].

this case merging and annihilation can occur for $\Delta\phi \simeq 0$. As reported in [70], this can be understood by considering the energy dissipated via radiation losses and the decrease in the binding energy that occur during the inelastic collision. If the sum of these two terms is equal to or exceeds the initial kinetic energy of the collision, merging in energetically favorable and annihilation occurs if $N > N_c$. It is then possible to calculate a critical velocity below which merging occurs [70]. Merging and annihilation of the two matter-waves have been observed, again this phenomena occur due to 3D nature of the systems. By a theoretical point of view, merging between solitons occurs if the relative velocity is smaller than a critical v_C that depends on the waveguide geometry as well as on the atom number [70].

Helium Clusters. A very important class of self-bound systems is represented by Helium droplets which are expected to have properties very similar to our quantum drops. Interesting results have been obtained in [71] where the authors make collide magnetically

levitated helium drops. During the early stages of the coalescence dynamics, a small contact region between the two drops called neck grows rapidly. In classical liquid drops the power-law increase of the neck diameter depends on the viscosity of the liquid bulk. In superfluid systems, as Helium drops, the bulk, contrary to the surface, has no viscosity. For this reason the coalescence of superfluid drops displays a peculiar power-low scaling which is a smoking-gun of the superfluid flow occurring in the bulk [72].

Finally studies on the collisions between the atomic quantum droplets described in this Chapter have been performed so far only for a pure 1D systems [73]. In this work the authors show that colliding droplets may merge or suffer fragmentation, depending on their relative velocity, phase and atom number. An experimental observation of quantum droplets in a pure 1D system is anyway still missing.
Although these theoretical results can help us understanding the qualitative picture of the different possible collisional outcomes, a quantitative comparison is not feasible since the relevant droplets parameters are strongly affected by the dimensionality of the system.

Chapter 3

Optical compensation of gravity

One of the most important issues concerning the experimental observation of quantum droplets is related to gravity. To keep the self-bound state in the center of the high resolution imaging system, it is necessary to compensate for gravity after releasing the atoms from the trap. Typically, in the ultracold atoms framework, gravity is compensated using a magnetic gradient. An atom in a given hyperfine level possesses indeed a characteristic magnetic moment, $\mu(B)$. A linear magnetic field thus creates a force on the atoms provided by $-\mu(B)\nabla B$. By tuning properly the magnetic gradient it is possible to cancel gravity.

This solution cannot be used in our case, since we are interested in studying a quantum droplet formed by a Bose-Bose mixture and, in the region of magnetic field where the two species satisfy the collisional properties necessary for the creation of the self-bound state, the two components posses different magnetic moment. Indeed, applying a magnetic gradient to such a system imposes, a different force to each component thus separating them as in a Stern-Gerlach experiment.

For this reason we implemented an innovative technology that is able to compensate for gravity in a homo-nuclear mixture of ultracold atoms. It makes use of the dipole force, i.e., the conservative force provided by a far off resonance light on the atoms, that acts in the same way on both species. To paint the linear gradient of light we use a time-averaged optical potential.

Before starting to explain how the setup works, I want to briefly discuss what are the characteristics that the levitating potential should have. Obviously we require that it creates a force on the atoms opposite to gravity but, in addition, it should also introduce negligible residual confinement in every direction. This condition is required mainly for two reasons: the first one is that in order to probe the self-bounded nature of the droplet we need to observe it in free space, ideally without any external trapping. Secondly, if we compress the droplet in a trap we expect that its life time is reduced. This happens because the density of the in-trap droplet would become larger than the equilibrium value and, in this case, three-body recombination processes dramatically reduce the lifetime of the system. We can give an estimation of the maximum frequency that the droplet can afford as follows. The droplets size is of the order of 1-3 μm. It is well known that a harmonic potential has an associated length scale, the so called harmonic oscillator length $a_0 = \sqrt{\hbar/2\pi m\nu}$ where ν is the trapping frequency of the potential. To a first approximation, we want that the harmonic oscillator lengths related to the residual trapping frequencies are larger than the droplet size. For $\nu = 20$ Hz, $a_0 = 3.6$ μm thus we require residual curvatures to be smaller than 20 Hz.

This Chapter is organized as follows: in the first section we will introduce some theoretical aspects about the time-averaged optical potential, finding what is the better design to compensate for gravity. After that, in Section 3.2, I will present the setup we realized while in Section 3.3 the lower and the upper bounds on the modulation frequency. Finally in Section 3.4 I will show the characterization measurements performed on the atoms, giving particular

attention to those concerning the residual confinements.

3.1 Time-averaged optical potential

Time-averaged potentials can be used to create potentials with arbitrary shape [74].The great advantage of this technique is the possibility of creating potentials for trapping Bose-Einstein condensates, which are simultaneously dynamic, fully arbitrary, and sufficiently stable to not heat the ultra cold gas. The setup that we implemented makes use of just one Acusto-Optical-Modulator (AOM). This solution is much simpler than others using, for instance, Spatial Light Modulators (SLM) [75] or Digital Micromirror Devices (DMD) [76] to crate arbitrary potentials.

The idea of a time-averaged optical potential is simple: a far detuned laser creates an optical potential that is proportional to the intensity of the laser light, i.e., $V_{opt}(z,t) \propto I(z,t)$ [77]. Suppose to have a gaussian beam with an intensity profile given by $I(z,t) = I_0 e^{-2(z-z_0(t))^2/w_z^2}$, where the position of the center is periodically modulated in time using the AOM with period T: $z_0(t+T) = z_0(t)$. If T is much smaller than the typical time scales of the atom dynamics, the atoms experience a potential that is the time average of the modulated one:

$$V(z) = \frac{1}{T} \int_0^T V_0 e^{-2(z-z_0(t)^2/w_z^2)} dt \tag{3.1}$$

Choosing an appropriate modulation function of the beam center $z_0(t)$, we can create an arbitrary optical potential along z which is the vertical direction.

In our case, to move the position of the laser beam, it is sufficient to change the Radio-Frequency (RF) applied to the AOM. In this way we can tune the Bragg angle and so the propagation diraction of the diffracted beam. To do that, it is sufficient to play with the voltage applied to the Voltage Controlled Oscillator (VCO) inside the AOM driver. In other words, the position of the laser beam is a function of a voltage V, $z(t) = f(V(t))$, where f depends on the optical system between the AOM and the atoms.

For our purpose we are interested in creating a linear potential that is able to cancel the effect of gravity on the atoms. To create such potential we require

$$dt \propto z_0 dz_0 \tag{3.2}$$

Calling t the a-dimensional time normalized by the period of the modulation $\tau = t/T$, it is possible to show that the function:

$$z_0(\tau) = \delta(2\sqrt{|2\tau - 1|} - 1) + \text{offset} \tag{3.3}$$

satisfies the differential Eq. in 3.2. The quantity δ is the amplitude of the modulation.

The modulation ramp has the shape reported in Fig. 3.1. Using Eq. 3.3 and Eq. 3.1 it is possible to calculate the time-averaged intensity. The linearity of the painted potential critically depends on the modulation amplitude δ and on the waist of the beam w_z. If $\delta \gg w_z$, that is the waist of the beam along the z axes, the averaged potential is in a very good approximation a linear potential. However, in order to cancel the gravity, the force provided by the optical potential must equal to mg. Increasing δ increases the scanned area and so, to keep the proper value of the averaged dipole force, it is necessary to increase the laser power. The latter indeed imposes an upper bound to the amplitude modulation δ, which is also limited by the maximum deflection angle that the deflector can reach. In our setup we have a maximum available power of the diffracted beam $\simeq 3$W. The laser beam has $w_z = \simeq 23(3)\mu$m while in the other direction $w_y = 1(0.05)$mm, the laser wavelength is 1064nm. With these parameters it is possible to prove that we can compensate the gravity using 2.7W of laser power and a modulation amplitude $\delta \simeq 50\mu$m.
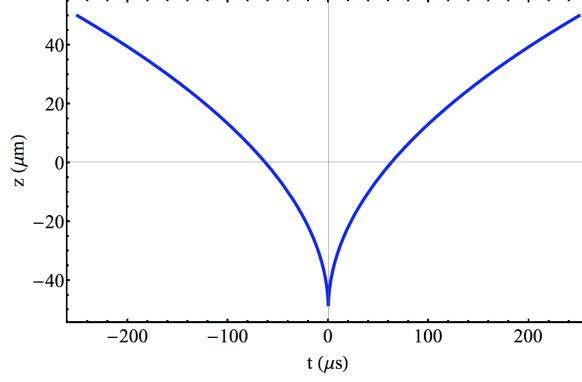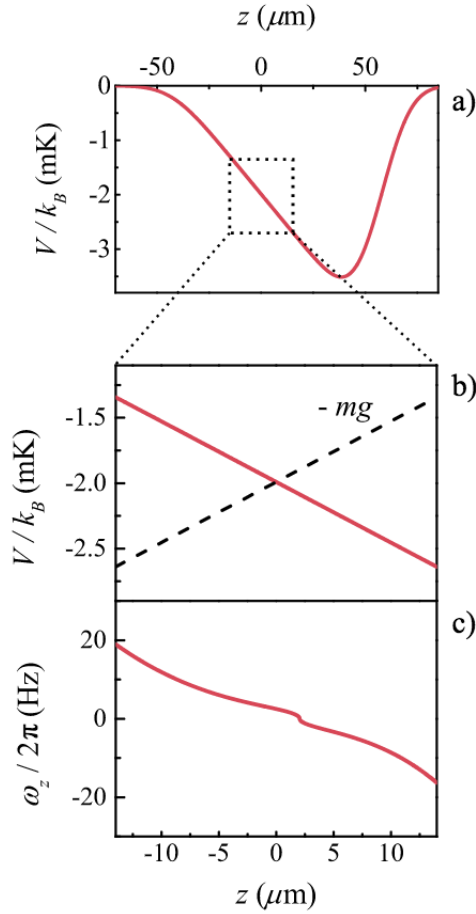
Figure 3.1: $z_0(t)$ for $w_z = 20\mu m$ and $\delta = 50\mu$m.

Figure 3.2: a) Profile of the time-averaged potential $V(z)$. b) Profile of $V(z)$ around $z = 0$ compared with gravity. c) Calculated curvature produced by the levitating potential along the vertical direction.

In panel a) of Fig. 3.2, I report the expected profile for $V(z)$ evaluated using the above parameters. In b), we report a zoom of the time-averaged potential in comparison with the linear gravitational potential for an atom of ^{39}K. Finally, in panel c), we report the calculated residual trapping frequency induced by the potential:

$$\omega_z(z) = \sqrt{\left|\frac{V''(z)}{m}\right|} \; \text{sign}\left(\frac{V''(z)}{m}\right) \tag{3.4}$$

29

using the convention that if the residual trapping frequency is negative the potential is anti-confining.

We notice from Fig. 3.2 that the calculated ω_z is of the order of a few Hz in the central part of the potential and $|\omega_z| < 20$Hz on a region of 30μm.

I would like to point out that this is not the only solution for creating a linear optical potential. As I will describe in the following, this solution is affected by some complications related to the high harmonics components of the modulation function $z_0(t)$. Another possibility is, for instance, to modulate linearly in time both the position and the amplitude of the laser beam. This solution has the drawback of requiring more laser power than the one described here, which is the reason why we choose this solution.

3.2 Optical setup

In this section I will describe the optical setup used to create the time-averaged optical potential.

The laser source we use is a Mephisto Mopa laser with a wavelength of 1.064μm, with an output power after the isolator of 20 W. After passing through a non-linear crystal for the creation of light at 532nm used for the repulsive barrier in the collision experiment of Chapter 6, the residual infrared light is coupled into a high-power optical fiber. With a precise mode matching we optimized the coupling up to 80%. At the fiber output we have a collimated beam with a waist of $\simeq 600$ μm that goes directly inside the AOM. In the diffracted order we have at maximum approximately 3W. The AOM has two main purposes: acting on the frequency of the RF, we modulate the beam position and tuning the amplitude of the RF we stabilize the beam intensity.

A pictorial representation of the reference frame as well as the non-modulated beam is reported in Fig. 3.3. To obtain a good linearity of the potential, w_z has to be as small as the optical access to the atoms allows. The only accessible optical path require that the beam passes through a 200mm lens (L3) with a focal plane on the atoms. This lens is located in a box and the beam can access it by passing through a hole of 1cm in diameter. This constraints limits w_z to a minimum value of 20μm.

The optical setup is represented in Fig. 3.4. It is made of a cylindrical telescope (lenses L1
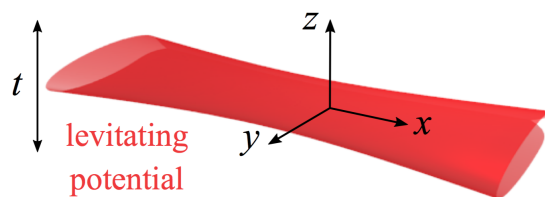

Figure 3.3: Non-modulated far detuned IR beam used for creating the time-averaged optical potential.

and L2) that magnifies by a factor 5 in the z direction the starting input beam. On the other direction, the y axes, the spherical lens L3 and the cylindrical lens L4 form another telescope that increases the beam size up to have $w_y \simeq 1$ mm. L1 and L2 are placed in specific positions with respect to the AOM and to the last spherical lens L3. Indeed, if the distance between L1 and the AOM is equal to f_1 and if the separation between L2 and L3 is equal to the sum of their foci $f_3 + 20$ cm, the diffracted beams obtained by changing the diffracted angle are parallel in the atom plane. We chose this solution because in this way the optical system is able to convert a diffracted angle into a displacement along z at the atom position. This

mapping is provided by $dz = d\theta_{Bragg}f_3/M$ where M is the magnification of the telescope in the z direction. Additionally, the optical path creates a very asymmetric beam, in this way we minimize the residual confinement in y direction.
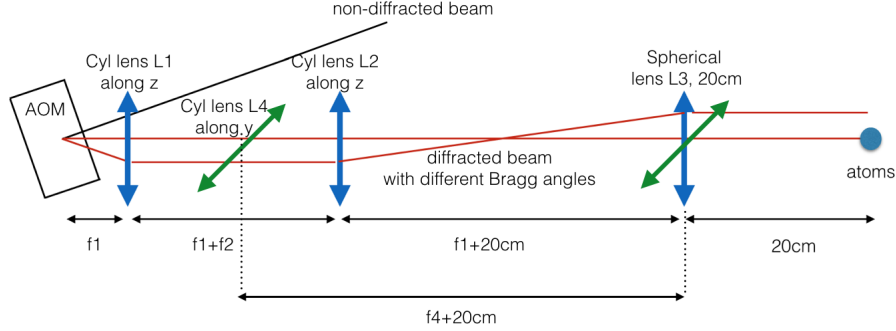

Figure 3.4: Geometrical path for the time-averaged optical potential. The black line represents the beam non diffracted by the AOM, while the red one the first-order diffracted beams using different Bragg's angles. The blue arrows represent the lenses along z direction while the green ones along y.

3.3 Modulation frequency

It is not trivial to understand what is the lower bound for the modulation frequency that we can use. Obviously if the beam is modulated too slowly, the atoms would follow the beam in its motion. To avoid micro-motion effects that would heat the sample [78, 79], we need to modulate sufficiently fast.

The minimum modulation frequency is set by the timescales of the density oscillations of the cloud in the unmodulated beam, which are determined by the trapping frequency. The relevant one is that along the vertical direction which is close to 500Hz and which determines density oscillation at 1KHz. In order to be more quantitative in the lower-bound limit of the modulation frequency, we perform a simulation of a non interacting BEC in the time-averaged optical potential and we study for different modulation frequencies the micro-motion and the heating of the cloud. The first parameter is related to the cloud while the second to its size. As it is possible to see in Fig. 3.5 both effects are negligible for modulation frequencies larger than 1 kHz, which sets a lower bound. On the other side, while one would say that the best option is to modulate as fast as possible, we need to consider some technical limitations to the maximum reachable frequency. They are related to the bandwidth of the VCO in the AOM driver and to the finite bandwidth of the AOM itself. These two aspects will be discussed in the next two sections.

3.3.1 VCO bandwidth

Typically our AOM drivers working around 110 MHz use with a ROS150 VCO. This VCO has a bandwidth of $\nu_0 =$100 kHz, which means that, if the modulation of the voltage has some Fourier components at frequencies larger than ν_0, the shape of the optical averaged potential could be affected. To quantify this effect we perform the following calculation. According to Fourier theory, a periodic even function $f(t)$ with period T, can be written as:

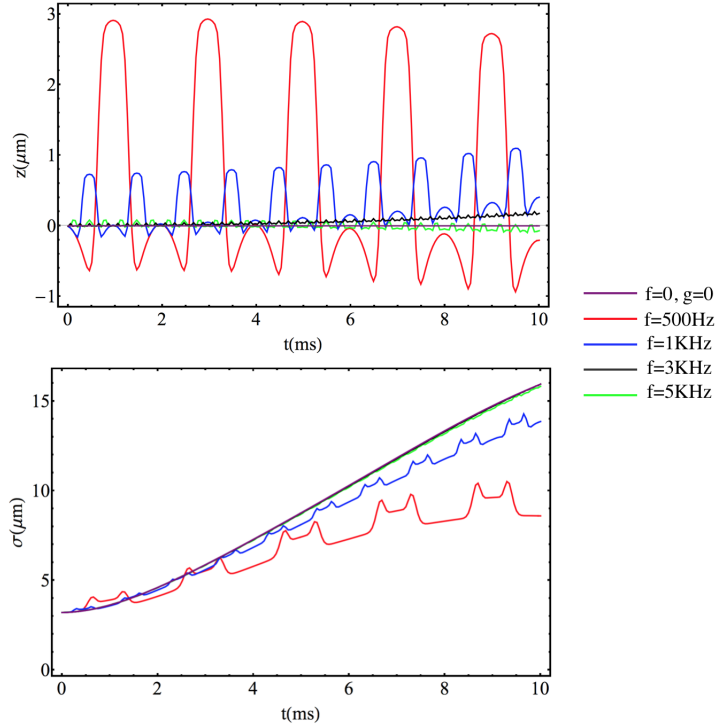$$f(t) = a_0 + \sum_{i=1}^{\infty} a_i \cos(2\pi it/T) \tag{3.5}$$

Figure 3.5: Upper panel: micro-motion of a not interacting BEC inside the time-averaged optical potential, for different values of the modulation frequencies. Below it is reported the simulated σ defined as the Thomas-Fermi radius.

where

$$a_i = \int_{-T/2}^{T/2} f(t)\cos(2\pi it/T)dt \tag{3.6}$$

while

$$a_0 = \int_{-T/2}^{T/2} f(t)dt \tag{3.7}$$

In order to understand the effect of the finite bandwidth, we calculate the Fourier spectrum of Eq. 3.3 using Eq. 3.6 and we convolve it with a first order low-pass filter with a cut-off frequency of 100 kHz. With an inverse Fourier transformation, we can estimate the filtered modulation function and we can use it to numerically evaluate the resulting time-averaged potential. We perform the same analysis for different values of the period of the modulation T. Results for $z(t)$ and for some averaged optical potentials are reported in Fig. 3.6 together with some intensity profiles acquired with a CCD camera before aligning the beam on the atoms. As we can see, the ramp profiles change as T decreases. This calculation, even if simplified, because the voltage VCO frequency transfer function has not been characterized with great accuracy, well explains the experimental images acquired by the CCD as can be seen by comparing the profiles in the central and right columns of Fig. 3.6. The effect on the atoms of the modified optical profiles, is to increase the residual trapping potential even for a modulation period of 1/5 kHz.

We solved this problem by changing the VCO in the AOM driver with another model ROS-355-219+, which has a much larger bandwidth of 3MHz but with a central frequency of 355MHz. Since the AOM we use works at a frequency of 110MHz, the VCO output is mixed with a fixed RF at 445MHz and then the signal passes through a lowpass filter with a cutoff at 150MHz. In this way the RF that is amplified and then applied to the AOM is at 110MHz and can be modulated with a larger bandwidth. Since we have implemented this new VCO when the system was already mounted on the atoms, we could not acquire any CCD pictures
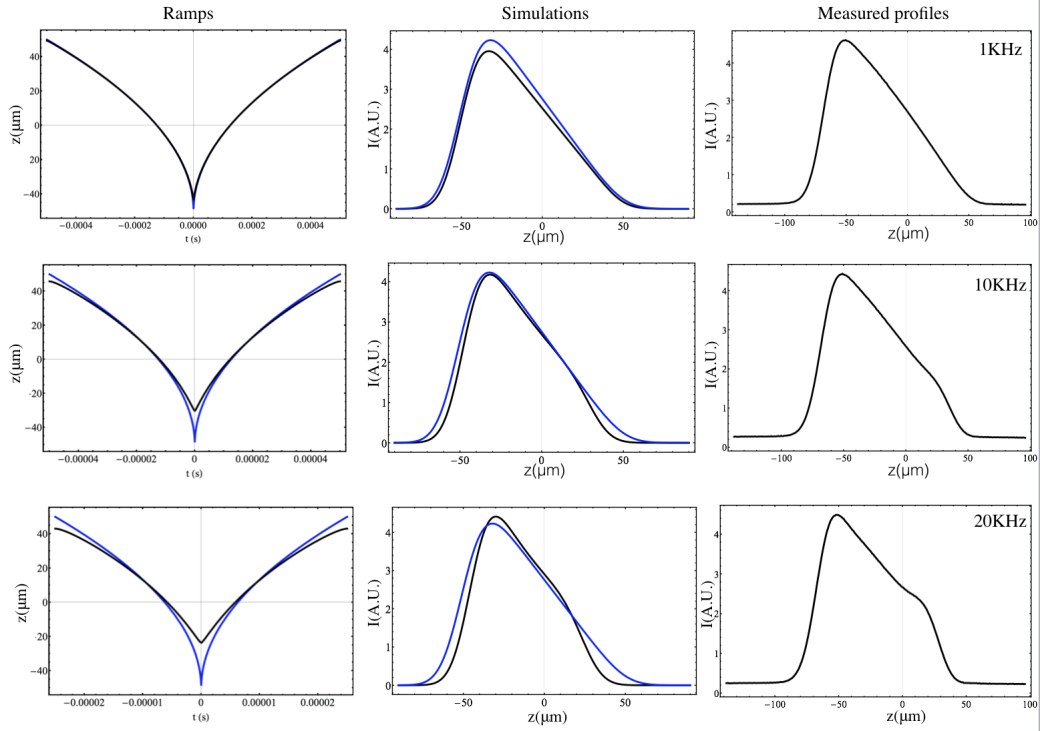
Figure 3.6: Effect of the low pass filter effect of the VCO on the modulation function (left column) and on the averaged optical potential (central column). In the right column we report some experimental pictures of the intensity profile acquired with an auxiliary CCD. In the first row the modulation frequency is 1 kHz, in the second 10 kHz and in the third 20 kHz. In the first two columns the calculated profiles in black are compared with the ideal profiles in blue.

with the faster VCO. Based on the caluculated profiles we can anyway conclude that the upper bound imposed by the VCO bandwidth has been shifted up to 100 kHz.

3.3.2 Intensity stabilization

The second effect that modifies the shape of the averaged potential is the intensity fluctuation of the beam. Eq. 3.1 is valid if V_0 is fixed, i.e., if the laser intensity is constant. As we will show in the following, in order to move z_0 by 50 μm we need to change the RF in the AOM by 7 MHz and, in this region, the diffraction efficiency of the AOM is not flat, i.e. the intensity of the diffracted beam is not constant. This intensity variation can be compensated by stabilizing the output power with a feedback loop on a Proportional-Integrator (PI) controller but since this effect is caused by the time modulation, the intensity fluctuations have the same frequency components of the modulation function. We optimized the PI to have a measured bandwidth of 100kHz, but, as we will see, this effect is still the one that mostly limits the performance of the time-averaged potential setting an upper bound to the modulation frequency.

The AOM we use is a 3100-125 by Crystal Technology and it works around 110MHz, with a bandwidth of 20MHz. To characterize the efficiency of the AOM we measure the output power of the diffracted beam changing the RF frequency in a range of ± 10 MHz. The efficiency curve together with a polynomial fit $E(dF)$ where dF is the difference with respect to the central frequency of 110MHz, is reported in Fig. 3.7.

Due to this effect the amplitude $V_0 E(t)$ of the modulated beam varies during the periodic
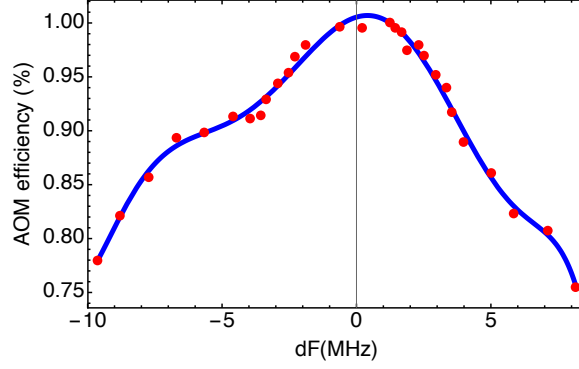
Figure 3.7: Red dots: measured efficiency of the AOM as a function of the RF frequency. The blue curve is a polynomial fit to the experimental data

modulation. The time-averaged potential is thus:

$$V(z) = V_0 \int_0^1 E(\tau) e^{-2(z-z_0(\tau)^2)/w_z^2} d\tau \tag{3.8}$$

where again $\tau = t/T$ is the a-dimensional time and $E(t) = E(dF(\tau))$. As we introduced before, the position $z_0(\tau)$ of the diffracted is proportional to $F(\tau)$, i.e., $F(\tau)$ has the same dependence on time of $z_0(\tau)$. In Fig. 3.8 I reported $F(\tau)$ and the corresponding $E(\tau)$, evaluated from the polynomial fit of Fig 3.7.

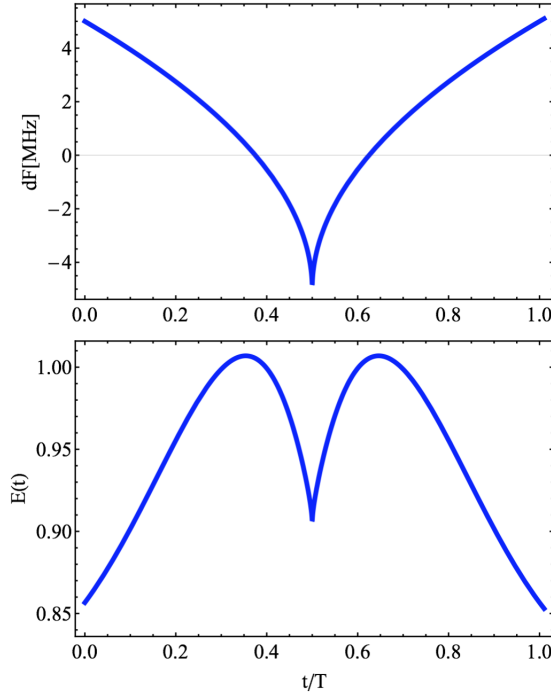The effect of the AOM efficiency on the shape of the potential is problematic because it

Figure 3.8: Upper pannel: $dF(t)$, lower pannel $E(t)$.

increases the residual trapping frequency, up to 50Hz in the central of the potential and it also decreases the mean intensity of the optical potential. In Fig. 3.9 I reported the profiles of the ideal time-averaged optical potential compared with the one obtained taking into account the AOM efficiency, and the curvatures evaluated curvatures calculated according to Eq. 3.4.
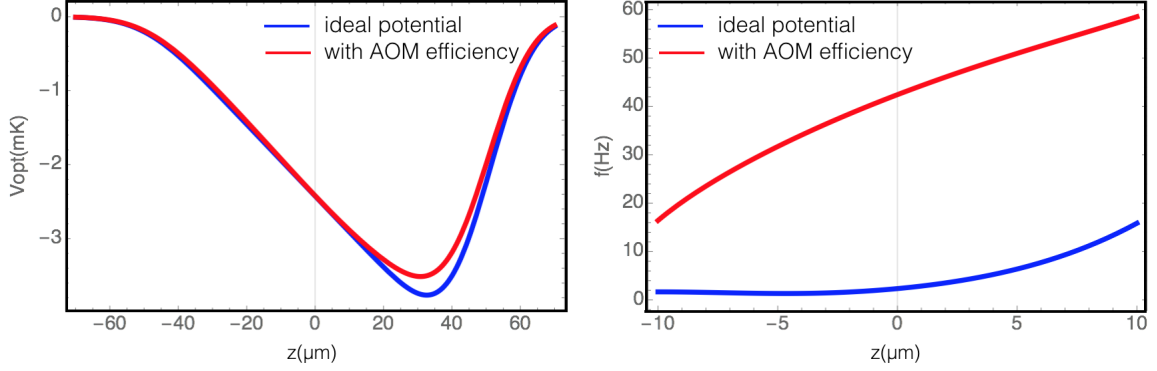
34

Figure 3.9: Left panel: ideal optical potential (blue curve) and the one obtained taking into account the AOM efficiency. Right panel: residual curvature measured by the trapping frequency along the vertical direction z.

These effects can be reduced by implementing the intensity stabilization mentioned above. The PI controller we use has a bandwidth of 100 kHz, which means that the noise introduced by the AOM efficiency is not completely compensated. The Fourier components of $E(t)$ are larger than 100 kHz even for modulation frequency of 5 kHz. We can try to get an estimation of the residual trapping frequency and the modified profiles as follows. We model the PI as a high-pass filter with a cutoff at 100 kHz. This is obviously a brutal approximation but as we will see it works well. As before we evaluate the Fourier spectrum of $E(t)$ and we convolve it with the PI gain function. Applying the inverse Fourier transform, we get a new function $E_{PI}(t)$ that takes into account the PI correction. In Fig. 3.10 are reported the residual curvatures for different modulation frequencies. As it is possible to see, the residual frequencies are smaller than 20Hz in a region sufficiently larger than the typical droplet size for modulation frequencies smaller than 10kHz.

Considering the upper bound to the modulation frequency discussed here and the lower bound introduced above we decide to work at 1/T=3 kHz. The main limitation of the system is
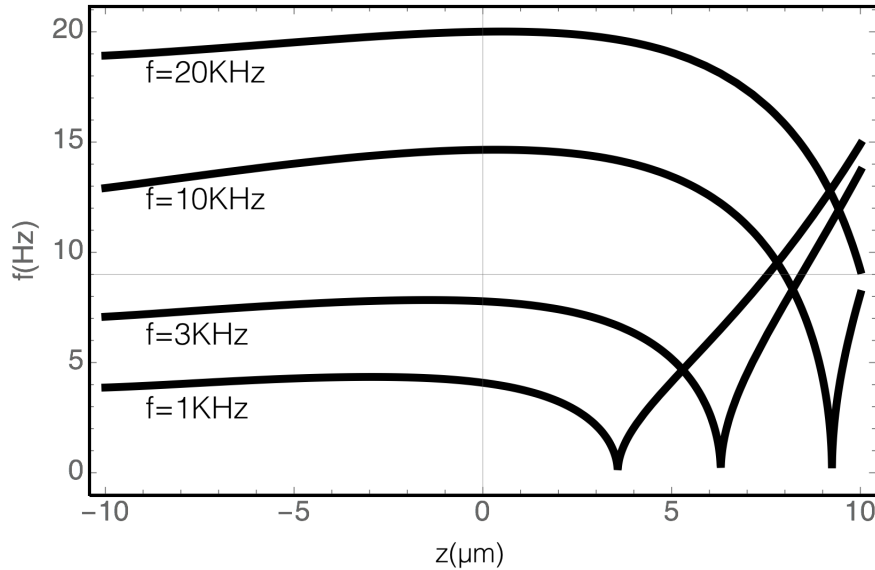

Figure 3.10: Residual curvature, measured by the modulus of the trapping frequency, introduced by taking in account the AOM efficiency and the PI correction.

related to the AOM efficiency. To solve this problem we could change the AOM in the setup

with an Acusto-Optical-Deflector (AOD). This device is characterized by a very flat efficiency inside the operation bandwidth and the problem discussed in this section should be reduced significantly.

3.4 Calibration on the atoms

3.4.1 Alignment

Here I will present the calibration measurements performed on the atoms. In the first one we verified the proportionality between the displacement of the beam at the atom position and the voltage applied to the VCO. Let us start with a "theoretical" prediction of this quantity. Using the VCO and a spectrum analyzer we measure the linear dependence between the applied voltage and the RF, finding that:

$$F(\text{MHz}) = 110.2 - 0.065 \frac{\text{MHz}}{\text{mV}} Vin(\text{mV}) \tag{3.9}$$

The AOM maps the frequency difference $dF = F - 110.2\text{MHz}$ into an angle deviation $d\theta$ of the diffracted beam. The relation between the two quantities is provided by the Bragg Law:

$$d\theta = \lambda \frac{dF}{v_s} \tag{3.10}$$

where λ is the wavelength of the laser radiation, $1.064\mu m$, and v_s is the speed of sound in the crystal. Since the AOM we use is made of TeO2, v_s is known and it is equal to 4260 m/s. Using Eq.s 3.9 and 3.10 it is possible to evaluate a constant of proportionality between the applied voltage variation dV and $d\theta$:

$$d\theta = -1.6 \frac{10^{-5}}{\text{mV}} dV(\text{mV}) \tag{3.11}$$

The optical setup we implemented maps $d\theta$ into a displacement dz on the atoms plane. More precisely $dz = -d\theta f_3/M$ where M is the magnification of the telescope, that in our case is M=5. We get:

$$dz = 0.64 \frac{\mu m}{mV} dV(mV) \tag{3.12}$$

In order to check if this theoretical estimation is correct, we perform the following measurement: we modulate the position of the beam with a function $dV(t/T) = (-50(2\sqrt{|2t/T - 1|} - 1) + 4)\text{mV}$, a modulation frequency $1/T = 50\text{Hz}$ and a phase $\phi \simeq 0.1$ radiants and we measure the vertical position of the BEC trapped in the potential, as function of time. Since the modulation frequency is slow, the BEC follows the beam in its motion. In Fig. 3.11 we report the experimental data in blue and the theoretical prediction of the position of the beam in red (see Eq. 3.12).

The error bars in Fig. 3.11 are estimated as half of the variance $\sigma_z/2$ of the gaussian fit of the density profile $n(z) = n_0 e^{-z^2/(2\sigma_z^2)}$. The experimental data are in good agreement with the theory, confirming that the setup is well aligned and validating our prediction on the characteristics of the levitating potential.

3.4.2 Residual trapping frequency

In this section I will describe the measurements performed on the atoms to get an estimation of the residual trapping frequency along the vertical direction introduced by the optical compensation of gravity. Since the residual curvature defined as in Eq. 3.4 has a peculiar dependence on z, it is not so easy to measure. Two different measurements are possible: a
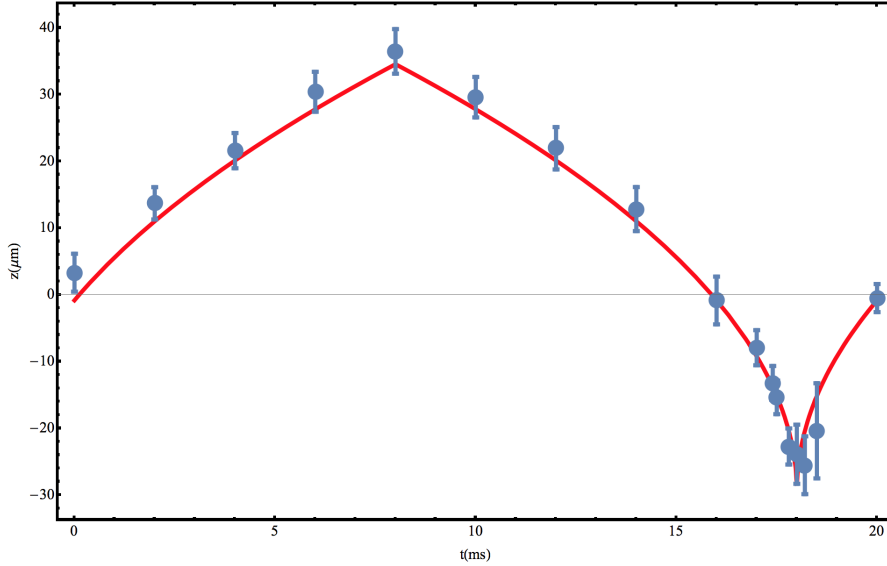
Figure 3.11: Calibration of the movable beam on the atoms. Blue points represent the experimental data of the position of a BEC that follows adiabatically the moving beam. In red the theoretical prediction obtained from equation 3.12.

local one where we measure the residual trapping frequency $f(z_0)$ at a certain position z_0, and a global measurement, where the result is a residual trapping frequency averaged in a finite spatial domain $z_0 \pm \delta z$. We performed both of them.

The local measurement we made is the following. We measured the trapping frequency of the radial beam (a beam that propagates along x with a waist of 10μm; see next chapter for more details) with a very small oscillation amplitude ($\simeq 1\mu$m) cancelling gravity with the optical levitation. The measured measured trapping frequency will result from the actual trapping frequency of the radial beam f_{rad} plus $f(z_0)$ provided by the gravity compensation:

$$f_{mis} = \sqrt{f_{rad}^2 + f(z_0)^2} \tag{3.13}$$

The measured trapping frequency could be even smaller than the one provided by the radial beam alone if the optical levitation beam introduces a residual anti-confinement on the atoms, i.e. $f(z_0)^2 < 0$.

We repeat the same measurement cancelling gravity via magnetic levitation making use of two coils in Anti-Helmotz configuration. Since the residual magnetic curvature is negligible, this measurement provides an estimation of f_{rad}. Notice that we measured the radial trapping frequency cancelling the gravity in order to remove the shift in the potential minimum position caused the the gravitational force. The results of the two measurements are reported in Fig. 3.12.

To measure the trapping frequency, we load a BEC in $|1,0\rangle$ state in the radial trap with gravity cancelled magnetically or optically, we then switch off the magnetic or optical gradient for a small time δt during which the atoms fall down with respect to the initial equilibrium position. When gravity compensation is turned on again, the atoms starts to oscillate in the beam at the frequency of the trapping potential. The falling time δt determines the value of the amplitude oscillation A_0 that we set to $A_0 \simeq 1\mu$m. The errors bars in the position measurements are obtained repeating the experimental sequence 3-5 times. We fit the data with a function $A_0 \cos(2\pi f t + \phi) + B$. The frequencies we measured are $f_{magnetic} = 129(1)$ Hz and $f_{optical} = 128(2)$Hz. The error bars come from the χ^2 estimation between the experimental data and the fitted model. The main result is that the two measured frequencies are compatible within the error bars. One can then conclude that we can set an upper limit
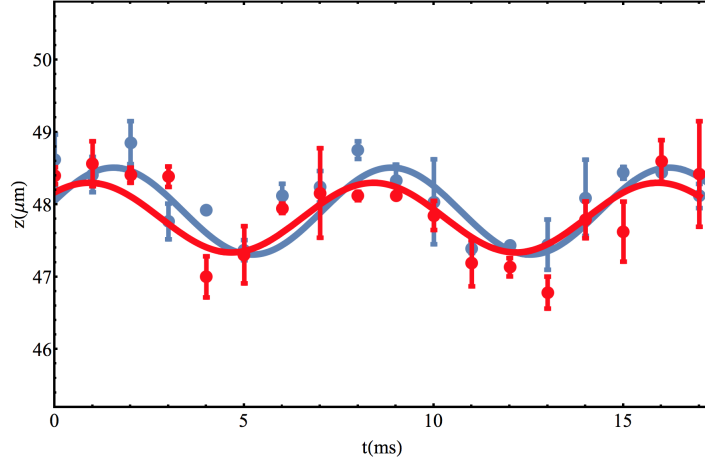
Figure 3.12: Measurement of the local residual trapping frequency of the optical levitation. The blue and red points represent the measured vertical position of the BEC oscillating inside the radial beam in presence of magnetic or optical gravity compensation respectively. The curves correspond to the fitting functions described in the text to deduce the values of the trapping frequency f_{magn} and f_{opt}.

for the curvature in the system, which is given by the discrepancy in the measurements and corresponds to $|\nu < 16|$Hz.

The second measurement we perform on the atoms predict information about a global
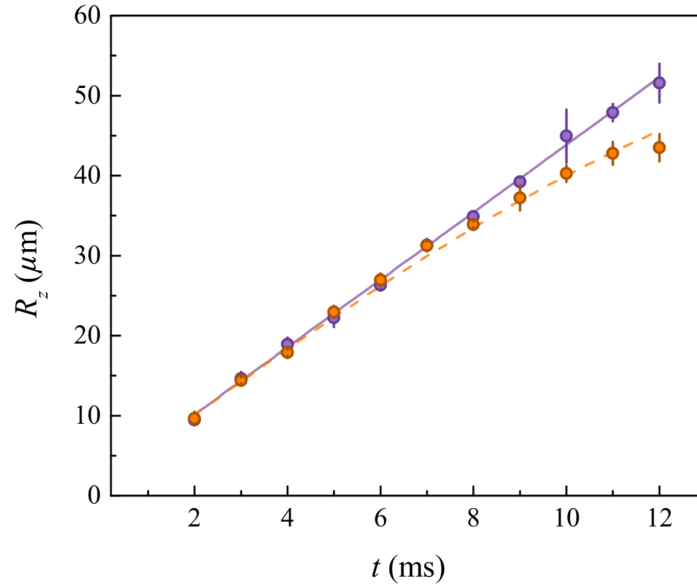

Figure 3.13: Global measurement of the residual trapping frequency. Expansion of a BEC in the levitating potential (orange dots) vs free space (purple dots). We measure the Thomas Fermi radius along the vertical direction after releasing a BEC from its dipole trap. The purple points correspond to the free-space evolution, while the orange ones to the expansion in the levitating potential. The theoretical curves are the result of the evolution calculated from the Gross-Pitaevskii equation in free-space (solid purple) and with a vertical confinement of 12Hz (dashed orange)

curvature. We compare the expansion of a Bose-Einstein condensate in $|1,1\rangle$ with $a =7.5\ a_0$ in the levitating potential and in free space. In figure 3.13 we report the measured Thomas-Fermi radius of the cloud along the vertical direction, as a function of the expansion time.

We compare them to the theoretical curves corresponding to the expansion of the BEC in free space and in a harmonic potential $V(z) = 1/2 m \omega_z^2 z^2$. When the Thomas Fermi radius in the vertical direction becomes larger then 30 μm we observe a deviation between the expansion in free fall and in the levitating potential. We then numerically simulate the expansion of the cloud in a harmonic trap for different values of ω_z. We observe a good agreement between the data taken in the optical levitating potential and the expansion where we set $\omega_z = 2\pi 12$Hz. This measurement is mostly sensitive to the curvature at large distances, so that it also provides only an upper bound to the effective confinement experienced by the droplets around $z = 0$. Consider in addition that the droplet size is much smaller than 30 μm. The residual confinement along the other two directions is very weak and it can be calculated considering the time-averaged potential at $z = 0$:

$$V(x, y, z = 0) = V_0 e^{-2y^2/w_y^2} \int_0^1 dt e^{-2(z_0(t)^2/w_z^2)} \simeq \frac{1}{3} V_0^e - 2y^2/w_y^2 \tag{3.14}$$

Considering the experimental parameters $w_y = 1$mm, $w_z = 23\mu$m and $P = 3$ W, we find that $\omega_x = 2\pi \times 3$ Hz and $\omega_y = 2\pi \times 2$ Hz.

Chapter 4

Experimental realization of a single quantum droplet

In this chapter I will discuss the results concerning the experimental realization and characterization of a quantum droplet made with a mixture of atoms in two hyperfine levels of ^{39}K. Most of the results presented here have been published in [12]. In the first part of the Chapter I will shortly recall some details about the experimental sequence we use to reach quantum degeneracy, after that, in Sec. 4.2, I will present all the steps used to create the quantum droplet. In Section 4.3 I will discuss the optimization of the imaging used to probe dense atomic clouds. In Sections 4.4 and 4.5 we will report the experimental results we obtained in comparison with Petrov's theory and with numerical simulations.

4.1   Production of the degenerate gas

In our laboratory we produce a degenerate gas of ^{39}K atoms using essentially three cooling stages. A schematic view of the experimental apparatus is reported in Fig. 4.1. The first cooling stage is performed making use of a $2D^+$ Magneto Optical Trap (MOT) that is used to collect atoms from the background and to create a cold atomic beam toward the second chamber. The second stage is the 3D MOT where the atoms are trapped and successively cooled below the Doppler limit to a few tens of μK. Atoms are then trapped in a magnetic quadrupole trap provided by a couple of anti-Helmotz movable coils that we use to magnetically transport the atoms into the final cell, the so called science chamber. A more detailed explanation of the first two cooling stages can be found in [80, 81, 82].

After the magnetic transport the atomic cloud is spin polarized because the only low-field seeker state of the ground state many-fold $F = 1$ is $|1, -1\rangle$. The last cooling stage to reach Bose-Einstein condensation cannot be performed in a quadrupole trap, due to the presence of a Ramsauer minimum in the elastic cross section of ^{39}K, which occurs for collision energies of 400 μK. For this reason, once the atoms reach the last chamber, we trap them in a very deep optical trap provided by a IPG-photonics YLR-100-LP-AC ytterbium fiber laser. This laser can provide up to 100 W of laser power at a central wavelength of 1064 nm, with an emission linewidth of 2 nm. The laser is focused close to the center of the magnetic trap, keeping a small displacement in order to avoid losses caused by Majorana spin-flips. Before starting the evaporation, the optical trap is turned on for 2s with a power of $\simeq$30 W that optimizes the trapped atom number to a maximum value of $\simeq 30\ 10^6$. The atomic cloud is then evaporatively cooled to quantum degeneracy. The evaporation sequence last 3 seconds with the power of the IPG varying from 30 W to about 5 mW and tuning the inter-particle interactions with the magnetic Feshbach resonance centred at 33.6 G. In the first 2 s the IPG is turned on at the maximum power, the scattering length is set to $a = 16\ a_0$. While decreasing the power we ramp the interaction up to $\simeq 150\ a_0$. To increase the trapping
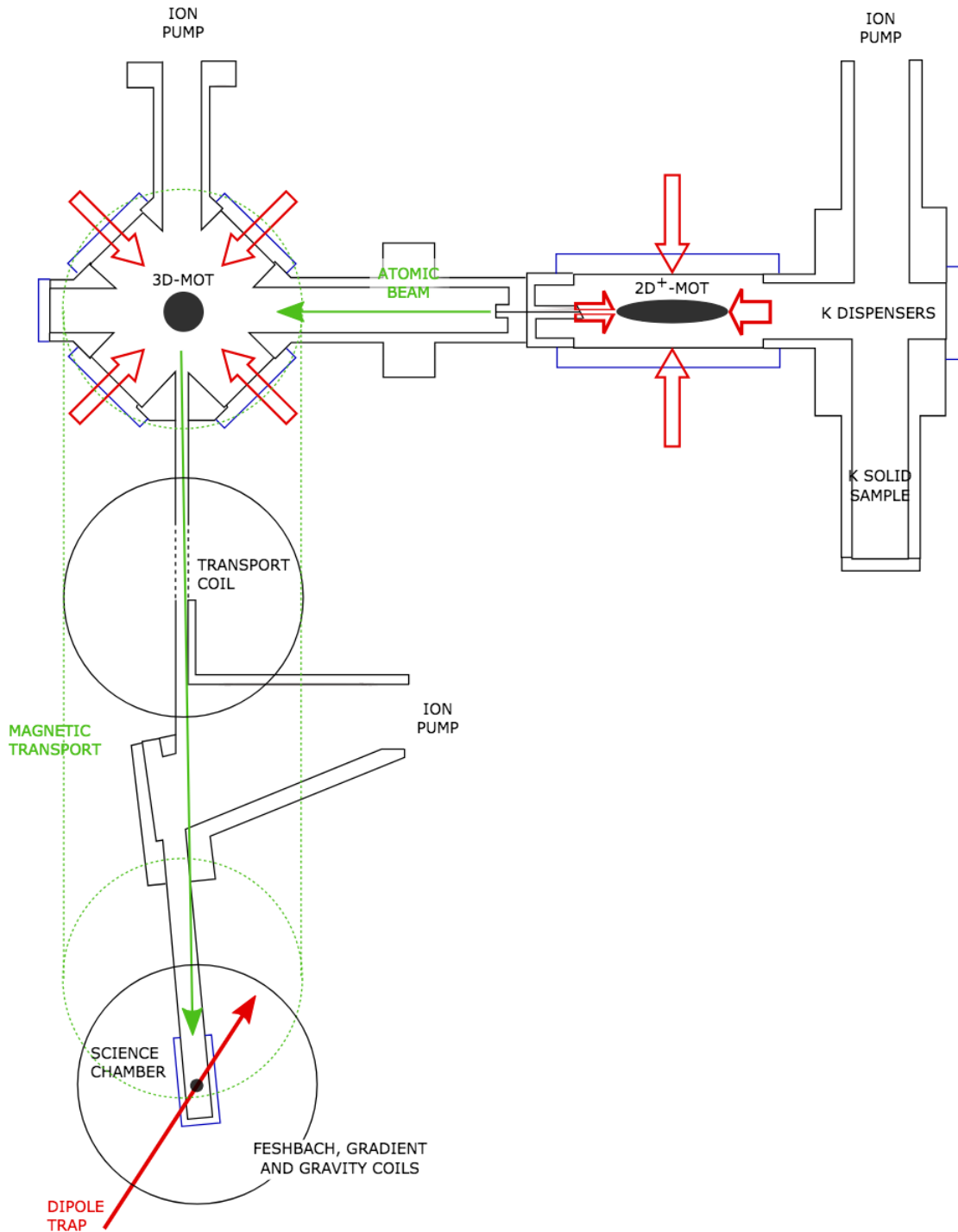
Figure 4.1: Schematic view of the experimental set up, including the three chambers and the three ion pumps. Image taken from [83].

confinement along the longitudinal direction of the IPG beam, we use a magnetic curvature . At the end of the evaporative sequence we successfully create a BEC with an atom number $N \simeq 10^6$ and a negligible non-condensed part (smaller than 10% of the total atom number).

4.2 Experimental sequence

After the creation of a BEC, we increase the value of the magnetic field up to $\simeq 55$ G turning off the magnetic curvature used during the evaporation. The BEC is transferred into a more isotropic optical trap descibed in Sec 4.2.1. Finally we set the magnetic field B to a specific value we create a 50%-50% mixture in the levels $|1, -1\rangle$ and $|1, 0\rangle$ by applying a radio frequency RF pulse (Sect 4.2.3).

4.2.1 Trap geometry

The BEC is trapped using three far-detuned infrared beams (see Fig. 4.2). The first one is called Radial beam and it propagates along the x direction perpendicular to the imaging direction (y) and it has a waist of 10 μm. The second one is the IPG beam used for the evaporation. It propagates in the x-y plane with an angle of about $\pi/4$ with respect to the imaging beam and the radial one. Finally, in order to load the atoms in an isotropic trap, we add an elliptical beam propagating in the vertical direction (z) with waists of $w_x = 39(3)\mu$m and $w_y = 105(5)\mu$m. The Radial and the vertical beams are provided by the same laser source, i.e. a Mephisto MOPA. Interference between them is prevented because the two beams are diffracted on different orders of their AOMs. In addition to these beams we add also the levitating potential introduced in the previous chapter. The latter propagates along the x direction, superimposed to the Radial beam.

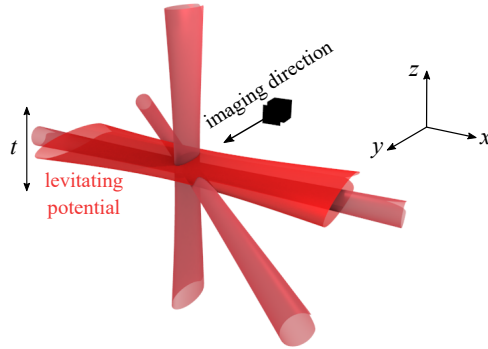For the experiment explained in this chapter the measured trapping frequency on the

Figure 4.2: Schematic representation of the laser beams composing the optical trap. All the beams used here are far-detuned infrared beam at 1064 nm.

resulting crossed trap are the following:

$$\omega_x = \sqrt{\omega_{Vert}^2 + \frac{1}{2}\omega_{IPG}^2} = 2\pi \times 195(10) Hz \tag{4.1}$$

$$\omega_y = \sqrt{\omega_{Rad}^2 + \frac{1}{2}\omega_{IPG}^2} = 2\pi \times 180(10) Hz \tag{4.2}$$

$$\omega_z = \sqrt{\omega_{Rad}^2 + \omega_{IPG}^2} = 2\pi \times 220(10) Hz \tag{4.3}$$

In the experimental sequence we transfer adiabatically the atoms from the IPG to the crossed dipole trap, while switching off the magnetic curvature used during the evaporation and tuning the homogeneous Feshbach field in the target region around $\simeq 56$G. At the end of the sequence the atom number in the BEC is $\simeq 500 \times 10^3$.

4.2.2 Collisional properties of ^{39}K

Collisional properties of ^{39}K have been well characterized from both an experimentally and theoretically point of view in [84].

The condition of negative MF energy and $|\delta g| << g = \sqrt{g_{11}g_{22}}$ are simultaneously fulfilled working with the states $|1,-1\rangle$, called state 2, and $|1,0\rangle$, called state 1, below a critical magnetic field of $B_C \simeq 56.86$ G. In panel a) of Fig. 4.3 all the scattering lengths for the two states are reported in a magnetic field range close to B_C. While a_{22} and a_{12} remain essentially constant in the considered region, a_{11} varies due to a Feshbach resonance centered at $\simeq 59.3G$.

In panel b) of Fig. 4.3, we report the expected phase diagram for the Bose-Bose mixture as a function of the magnetic field and of the atom number, obtained according to the theory presented in Chapter 2. For magnetic field larger than the critical one, the system is stable according to the MF and it is in a miscible gaseous phase. For $B < B_C$ the phase of the system depends on the atom number: if $N > N_C(B)$ the self-bound state can form, otherwise the system is again gaseous but it is stabilized by the LHY term against the collapse. We refer to that phase as LHY gas. The line describing the critical atom number is evaluated as $N_C = 22.55(n_1^0(B) + n_2^0(B)\xi(B)^3)$.

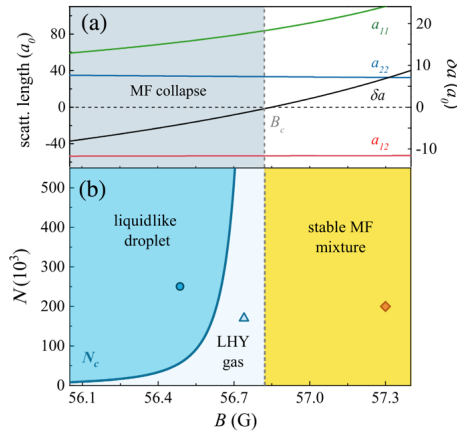Fig. 4.3 b) shows why ^{39}K is an appropriate candidate for studying quantum droplets.

Figure 4.3: (a) Intra- and interspecies scattering lengths between the hyperfine states $|1,0\rangle$ and $|1,-1\rangle$ of ^{39}K. The resulting MF energy of the mixture is proportional to the effective scattering length δa which becomes negative below $B \simeq 56.88$ G. (b)Phase diagram for the mixture as a function of the atom number N and of the magnetic field B.

Up to now, it is the only system where mixture droplets could be studied. The drawback of this atomic species is related to three-body losses in the state $|1,0\rangle$, as we will discuss in the following. Mixture droplets could also be investigated using heteronuclear mixtures. A possibility in this sense could be the bosonic mixture ^{87}Rb-^{39}K both atoms in the states $|1,-1\rangle$. It was proved experimentally [85] the existence of a Feshbach resonance for the interspecies interactions close to $B = 117.56$ G that could be used to achieve the correct interaction to form the droplet. Another system recently proposed is the mixture ^{23}Na-^{39}K. In this case it has been experimentally observed [86] that in broad region of magnetic field between $B \simeq 115$ G and $B \simeq 135$ G $\delta g < 0$ and small compared to g_{Na-Na} and g_{K-K}. The main advantage of the heteronuclear solution is that the lifetime of the system is expected to be much larger than in our case.

4.2.3 Creation of a Bose-Bose mixture

A crucial step in the formation of quantum droplets it the creation of the mixture. After loading the BEC in state 2 in the crossed trap, we transfer half of the atoms in state $|1,0\rangle$ using a $\pi/2$ pulse, achieved coupling the two states with an RF signal. Note that this procedure is in general not adiabatic and creates excitations in the sample. Despite that we choose this technique because it is faster with respect to adiabatic transfer which is crucial in order to limit the effect of three-body losses during the formation of the mixture. With the RF pulse we can create a balanced mixture in a few tens of μs. The $\pi/2$ pulse is applied using an RF generator and an attenuator, driven by a TTL, that we use as switch. Note that although the rising time of the RF is very fast, the complete switching off of the RF occurs in about $50\mu s$. An experimental measurement of the switching off time is reported in Fig. 4.4. To measure the transferred fraction we perform a Stern-Gerlach (SG) experiment: we separate the two species by applying a magnetic gradient. The force acting on each hyperfine level is opposite due to the opposite magnetic moments of $|1,0\rangle$ and $|1,-1\rangle$.

After the pulse the mixture is in a coherent superposition of the two hyperfine states: $\frac{|1,-1\rangle + |1,0\rangle}{\sqrt{2}}$. To measure the Rabi frequency, as well as the coherence time, we measured the transferred fraction as a function of time, keeping the coupling on, and we fit the data with a damped sinusoidal oscillation (Fig. 4.4 a-b). We measured a Rabi frequency of the order of 10 KHz and a coherence time of 450 μs. We conclude that the coherence does not play an important role in the long-time dynamics of the system which evolves for up to 20 ms.

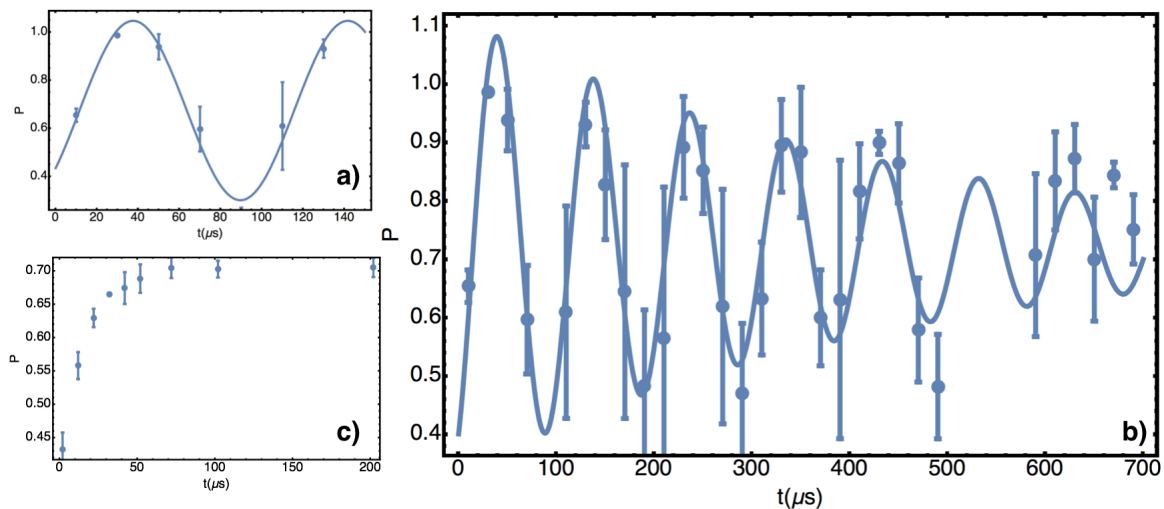RF spectroscopy is also used to calibrate the magnetic field. Note that, since the proper-

Figure 4.4: (a) Rabi oscillation between the two internal states. (b) Measurement of the coherence time in the mixture. (c) Measurement of the switching off time of the RF pulse. P is the ratio between the transferred atoms and the total atom number $N_1/(N_1 + N_2)$.

ties of the droplet critically depend on the scattering length and thus on the magnetic field, we need to calibrate it with great accuracy taking in account collisional shift [87]. We can roughly estimate its effect: as already pointed out in the fist chapter, the MF energy density of a Bose-Bose mixture is given by

$$e_{MF} = \frac{4\pi\hbar^2}{m}(\frac{1}{2}a_{11}n_1^2 + \frac{1}{2}a_{22}n_2^2 + a_{12}n_1n_2)$$ (4.4)

From Eq. 4.4 we can calculate the chemical potential of both components:

$$\mu_1 = \frac{\delta e}{\delta n_1} = \frac{4\pi\hbar^2}{m}(a_{11}n_1 + a_{12}n_2)$$ (4.5)

$$\mu_2 = \frac{\delta e}{\delta n_2} = \frac{4\pi\hbar^2}{m}(a_{22}n_2 + a_{12}n_1) \tag{4.6}$$

The collisional shift can be estimated as:

$$\Delta f_{12} = \mu_2 - \mu_1 = \frac{2\hbar}{m}n(a_{22} - a_{11} + f(2a_{12} - a_{11} - a_{22})) \tag{4.7}$$

where $n = n_1 + n_2$ is the total density and $f = (n_1 - n_2)/n$. Note that during the transfer, the value of f passes form $f = 1$ when $n_1 = n$ to $f = 0$ when the mixture is balanced. The collisional shift for $f = 0$, depends only on $(a_{22} - a_{11})$ while for the initial condition, $f = 1$, on $2(a_{12} - a_{11})$. In the magnetic field window where the droplet is expected, this second term is larger then the first. For this reason we evaluate the collisional shift for $f = 1$, considering that as the most relevant. Considering the geometry of the trap described before and using $400 \, 10^3$ atoms, we get a collisional shift of about 10 KHz. To confirm this result we perform RF spectroscopy on a BEC and on a thermal cloud at the same magnetic field. Note that in principle, at the same density, the thermal cloud is affected by a collisional shift larger by a factor 2 respect to the BEC where we have an anti-bunching effect due to Bose statistic. Experimentally the shift is much smaller in the thermal cloud because the density is generally one order of magnitude lower than the BEC. For this reason the transition measured using the thermal cloud is not significantly affected by the collisional shift. In Fig. 4.5 we report the collisional shift measured in our experimental condition at a magnetic field $B \simeq 56.56G$. The blue curve is a Lorentzian fit to the data acquired with a thermal cloud, while the black data and curve are related to the measurement with a BEC. The shift between the two resonances is 11 KHz compatible with the estimation described above.

Note that the collisional shift could depend in general also on the LHY energy. This could
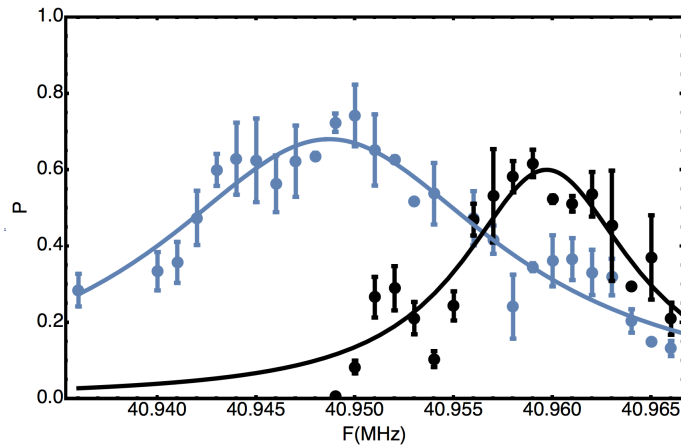

Figure 4.5: Measurement of the collisional shift. The blue points and the relative Lorenzian fit are obtained with the RF spectroscopy on a thermal cloud while the black data and curve correspond to the BEC. The measured shift is 11 KHz. Again P is the ratio between the transferred atoms and the total atom number $N_1/(N_1 + N_2)$

be a suitable tool to study the beyond-mean-field contribution, as recently pointed out in the theoretical paper [88].

4.3 Absorption imaging of dense atomic clouds

The equilibrium density of a quantum droplet reaches values of $10^{14} - 10^{15}cm^{-3}$ that is larger than the typical density of the BECs. To make a comparison, consider that the density of $400 \, 10^3$ atoms in the Thomas Fermi approximation ($a_s = 34a_0$ which is the case of state 2) trapped in an harmonic potential of 200Hz, is two orders of magnitude smaller. In this

section, after briefly discussing how absorption imaging works, I will describe how we can adapt the absorption imaging technique to probe such a dense system. Note that, in principle, to probe systems characterized by high optical density, other imaging techniques like phase contrast [89] or Faraday rotation [90] are in general more appropriate.

4.3.1 Absorption imaging and saturation effects

In the limit of low density and in the rotating wave approximation, an atomic cloud is characterized by a complex index of refraction given by [91]:

$$n_{ref} = 1 + \frac{\sigma_0 n \lambda}{4\pi}\left(\frac{i}{1+\delta^2} - \frac{\delta}{1+\delta}\right) \tag{4.8}$$

where $\sigma_0 = 3\lambda^2/2\pi$ is the resonant cross section for a two level atom, $\delta = 2(\omega - \omega_0)/\Gamma$ is the detuning of the probe light from the atomic resonance ω_0 in units of half linewidth Γ and n is the atomic density. Integrating the previous equation along the imaging direction one obtains the well-known Lambert-Beer law for the transmissibility of the light through the atomic sample:

$$T = \ln[I_{out}/I_0] = -\frac{n_{col}\sigma_0}{2}\frac{1}{1+\delta^2} \tag{4.9}$$

where $n_{col}(x, z) = \int n(x, y, z)dy$ is called column density. Note that light absorption depends only on the imaginary part of the refractive index. The real part of the latter, that is equal to zero for resonant light, imprints on the probing light a phase difference that is used in the non-destructive techniques cited above. Absorption imaging works by directly measuring the quantity T introduced in Eq. 4.9. This is done acquiring three different images: $I_w(x, z)$ detects the intensity of the probe light in the presence of the atomic cloud, $I_{wo}(x, z)$ without atoms and $I_{dark}(x, z)$ measures the background signal without both light and atoms. According to the the Lambert-Beer law we have $T =$

4.3.2 Optimization of the imaging system

In the following I describe the main problems we had to solve before using this partial transfer absorption imaging technique to accurately detect the droplet density profiles. Before introducing them, I would like to stress that understanding the interaction between near resonant light and a dense atomic samples is challenging and it is subject of specific of experimental [92, 93] and theoretical studies [94]. The measurements performed and reported here do not have the purpose of studying these phenomena. Our goal is to optimize the imaging sequence to perform reliable measurements of the droplet size.

4.3.2.1 Heating effect

The first parameter to optimize is the duration of the repumper pulse τ_{rep}. To study it we measure the size of the droplet as a function of τ_{rep}. Results are reported in Fig. 4.6. The size increases on pulse duration larger than 10μs while for smaller values the dependence from the pulse duration seems negligible. The observed effect can be explained, at least qualitatively, by considering heating effects due to the spontaneous emission of photons when the atoms decay from the $F' = 2$ state, that are reabsorbed by the neighboring atoms [95, 96]. For each scattering event, an atom acquires a random kick in momentum space given by $p_{rec} = \hbar k$, where $k = 2\pi/\lambda$ with λ the wavelength of the radiation. The atom, of mass m, thus acquires a recoil velocity of $v_{rec} = \hbar k/m$, in a random direction. This leads to a Brownian motion in momentum space, with a root mean square velocity transferred to the atoms given by:

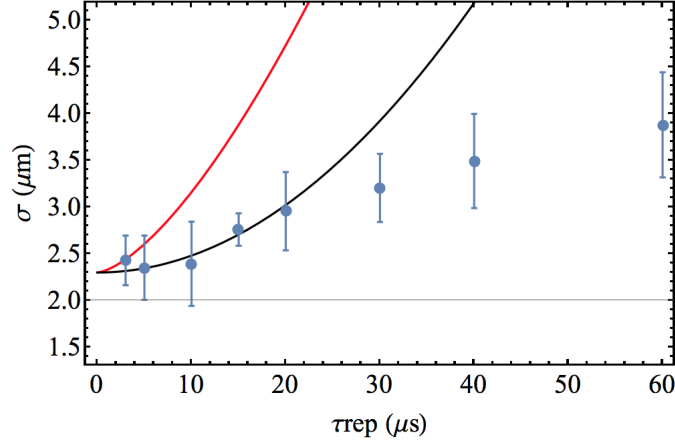$$v_{rms} = \frac{v_{rec}}{3}\sqrt{N_{photons}} \tag{4.10}$$

Figure 4.6: Comparison between the experimental data (blue points) describing how the droplet size changes as a function of the duration of the repumper pulse and the two models described in the text. The red curve describes the heating effect given by Eqs. 4.13 while the black one by Eq.4.15 (calculated for $I \simeq 10 I sat$ and $\Delta = 260$ MHz, which are the experimental parameters used for the repumper beam).

where $N_{photons}(t)$ is the number of photons scattered in the time interval t. This leads to an average displacement of each atom given by:

$$\Delta x_{rms} = \frac{v_{rms}}{3} \tau_{rep} \tag{4.11}$$

The scattered number of photons $N_{photons}(\tau_{rep})$ can be estimated as:

$$N_{photons} = \tau_{rep} \gamma \tag{4.12}$$

where $1/\gamma$ is the lifetime of the excited state [95]. This expression assumes that every re-emitted photons is re-absorbed by the atoms. In this limit the increase in the cloud size scales as $\tau_{rep}^{3/2}$ and it does not depend on the intensity of the probe beam:

$$dx_{rms} = \frac{1}{3} \sqrt{N_{photons}} v_{rec} \tau_{rep} = \frac{1}{3} \sqrt{\gamma} v_{rec} \tau_{rep} t^{3/2} \tag{4.13}$$

Since we are interested in the recoil heating produced by the repumper light, that in our case is far from resonance, the expression 4.12 is probably an overestimation of the number of scattering events per atom.

To better estimate the number of scattering events, we can assume that the number of atoms excited is $\Gamma_{scattering} \tau_{rep}$ where:

$$\Gamma_{scattering} = \frac{\Gamma}{2} \frac{I}{1 + I + 4\Delta^2/\Gamma^2} \tag{4.14}$$

where I is the intensity of the probe beam in units of the saturation intensity.

The photon produced by the decay of the excited atom is resonant according to the dressed picture of atom-light interaction. In this second limit the increase in size of the atomic cloud is given by:

$$dx_{rms} = \frac{1}{3} \sqrt{N_{photons}} v_{rec} \Delta t = \frac{1}{3} \sqrt{\Gamma_{scattering} \gamma} v_{rec} \tau_{rep}^2 \tag{4.15}$$

In this second approximation, the increase in size of atomic cloud depends on the intensity of the probe beam. Both models presented here are reported in Fig. 4.6. As we can see the second model fits better the experimental data for small duration of the repumper pulse.

Even if we cannot write down a model that exactly represents the experimental data on the whole range of τ_{rep}, these models help us to have at least a qualitative idea of the observed effect. To our purpose it is sufficient to know that below $\tau_{rep} = 10\mu$s this heating effect is negligible. We adopt exactly $\tau_{rep} = 10\mu$s to maximize the signal-to-noise ratio.

4.3.2.2 Switching-off of the magnetic field

As already mentioned, in order to perform absorption imaging we need to switch-off the magnetic field, so that both hyperfine states in the droplet become resonant with the imaging light. During the switching-off of the magnetic field the inter and infra-species scattering length in the mixture change due to the presence of Feshbach resonances. The switching-off time is however finite and during this time the atomic system evolves changing its size. Indeed, the switching-off of the magnetic field acts differently on the two hyperfine levels. The state $|1, -1\rangle$ passes through a Feshbach resonance centered at $B \simeq 35$ G , thus reaching extremely large values of a_{22}, which leads to an expansion of the cloud. On the other side, a_{11} becomes negative, so that the cloud is expected to contract.

In previous experiments performed with the same experimental apparatus[97, 98, 99], a switching time of $t_{switch} \simeq 500\mu$s was required before all magnetic fields were completely turned off. Given the much lower densities of the BECs studied in those experiments, the long switching time of the magnetic field did not have a significant effect on the measured size. In the case of the droplet, because of the small size and higher density, a significant effect was instead observed.

We experimentally reduce t_{switch} to 80 μs identifying and removing the major sources of eddy currents. In this condition we measure the size of a mixture as a function of the ratio between the two species. Results are reported in Fig. 4.7. To experimentally creates the mixture with a tunable ratio N_1/N_{tot}, we apply to the BEC in the state $|2\rangle$ a resonant RF pulse of different duration.

In order to better understand the effect of the switching-off of the magnetic field, we per-
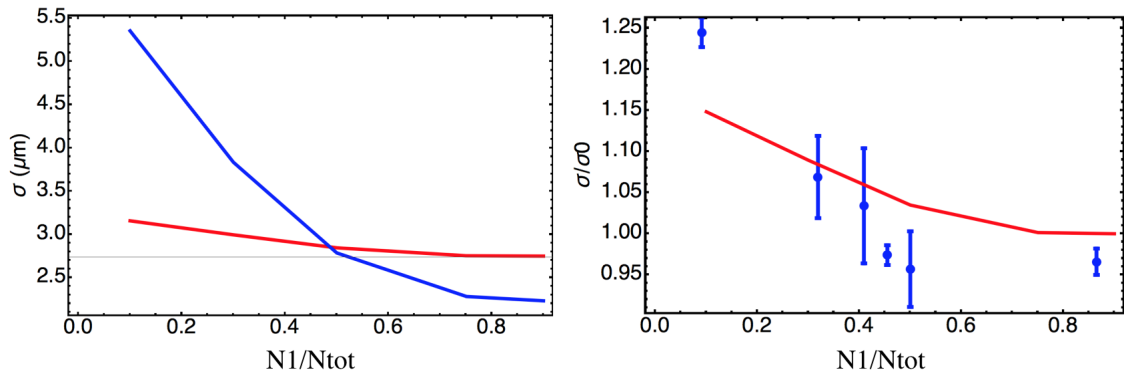

Figure 4.7: a) Simulated size after switching off the magnetic field in 500 μs (blue) and 80 μs (red) as a function of the population imbalance N_1/N_{tot}. b) Experimental data for the same quantity compared to the simulation performed, with $t_{switch} = 80\mu$s.

formed a numerical simulation of the evolution of a BEC mixture for different values of the parameter N_1/N_{tot} after ramping linearly in time the Feshbach field from a typical working value, $B = 56.45G$, to zero. In panel a) of Fig. 4.7 we report the results of the simulation for the two different durations of the ramp, $T_1 = 500\mu$s and $T_2 = 80\mu$s. As expected in system is mostly in the state $|1\rangle$ a the measured size is smaller than the initial one. In the opposite limit the effect of the magnetic field is to increase the system size. The effects is much larger on the state $|2\rangle$ that crosses a Feshbach resonance. Both these effects are much more evident

if the magnetic field is turned off in 500 μs.

In panel b) of Fig. 4.7 we report the measured size after switching off the magnetic field in T_2 and we compare it with the simulated curve. The simulation is based on a time dependent two-components Gross-Pitaevskii equation.

In conclusion, performing the imaging sequence with a switching-off time of 80 μs after switching-off the magnetic field, a systematic error on the measured size of the atomic cloud is introduced. This effect depends on the fraction of atoms in the two states composing the mixture, and it results to be negligible in the typical droplet configuration, where $N_1/N_{tot} \simeq 0.4$.

4.3.2.3 Resolution of the imaging system

The expected sizes of the droplets are pretty small, ranging from 1-3μm in the region of the magnetic field we consider. The measured width of a gaussian density profile is always increased by the imaging resolution δ defined as the $1/\sqrt{e}$ of the point spread function (PSF), as.

$$\sigma^2_{meas} = \sigma^2_{real} + \delta^2 \tag{4.16}$$

This derives from the convolution of the cloud with the PSF of the imaging system, which defines its finite resolution:

$$n_{img}(x,z) = n_{real}(x,z) * PSF(x,z) \tag{4.17}$$

The droplet size can be then deduced as:

$$\sigma_{real} = \sqrt{\sigma^2_{meas} - \delta^2} \tag{4.18}$$

The nominal resolution of the imaging system depends on the numerical aperture of the microscope objective used as the first lens of the imaging system. It has been estimated performing ex-situ measurements of the minimum observed distance between two nanoscale objects and it corresponds to $\delta_{nom} = 0.6\mu$m. The actual resolution of the imaging system is larger than the nominal one because it is sensitive to optical misalignments. To get an upper bound of the actual resolution, we load a weakly interacting cloud into a strong confining optical trap and we measure its size along the most compressed direction. Fitting the density distribution with a gaussian function we achieve a minimum variance σ equal to $0.8 \pm 0.1\mu$m. We decided to use this values for the estimation of the resolution of our imaging system, which is defined as $\delta_{res} = 0.8^{+0.1}_{-0.2}\mu$m.

4.4 Experimental results

A first characterization of the mixture is performed by exploring the phase diagram of Fig. 4.3 b). We prepare the mixture as explained in Sect. 4.2.3. At the end of the RF pulse we switch on the optical levitation and we switch off the optical trap and we let the mixture expand in free space. We detect the density profiles after a variable waiting time and measure the averaged size of the cloud $\sigma = \sqrt{\sigma_x \sigma_y}$. In Fig. 4.8 we report the evolution of the mixture in the three different regions of the phase diagram. We observe that both the repulsive MF and the LHY gas expand in time (upper raw of the density). Oppositely in the droplet region the cloud remains self-bound (lower raw).

We want to characterize the droplet phase measuring three observables: the size σ_{eq}, the critical atom number N_C and the ratio N_1/N_2 between the two states composing the self-bound cloud. These three quantities depend on the inter and intra-species interactions, and thus on the magnetic field. To measure the atom number as well as the composition between the two states, we perform a Stern-Gerlach (SG) experiment. In this way we can fit the two
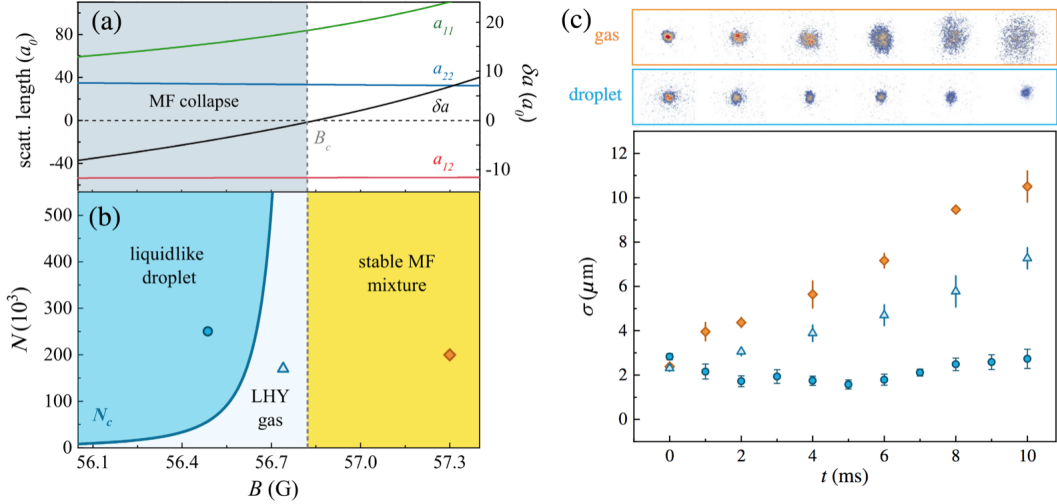
Figure 4.8: a) Intra- and interspecies scattering lengths between the hyperfine states $|1, -1\rangle$ and $|1, 0\rangle$ of ^{39}K, tuned by an external magnetic field B via Feshbach resonances. The resulting MF energy of the mixture is proportional to the effective scattering length δa, which becomes negative at $B_C = 56.86$G. (b)Phase diagram for the mixture as a function of the atom number N and of the magnetic field B. (c) Evolution of the cloud in free space for three different points of the phase diagram in (b). The upper rows show the difference between the evolution of the density profiles in the gas and droplet phases. Inset: Schematic representation of the geometry of the experiment.

atomic clouds separately, and measure the atom numbers N_1 and N_2. During this process the uniform Feshbach magnetic field is also increased. This is done so that the Stern-Gerlach separation occurs at a magnetic field where the mixture is out of the droplet phase and the splitting is easier, due to the reduced attractive interaction. The experimental sequence for both the SG experiment is summarized in Fig. 4.9 b.

Typical experimental results for the three observables under study are reported in Fig. 4.10 for a magnetic field of 56.45(0.1)G. As it is possible to see in panel a), the size of the system σ, after a fast reduction in the first milliseconds of dynamics, remains more or less constant up to a critical time t_C that in that case is close to 7ms. For $t > t_C$ the system expands. This behavior can be understood comparing the evolution of the system size to the one of the total atom number $N(t) = N_1 + N_2$ reported in panel b). The droplet quickly loses atoms for $t < t_C$, due to the three-body recombinations affecting essentially state 1. The losses in a mixture are provided by four channels. As reported in Appendix one we estimate all of them finding that the largest is $K3_{111} = 5 \times 10^{-27} cm^6/s$. The other three are more then one order of magnitude smaller then $K3_{111}$.

At $t \simeq t_C$ the atom number of the system becomes smaller then N_C, the critical atom number required to create a quantum droplet. The system naturally experiences a liquid-to-gas transition and exits from the droplet phase, as it is highlighted in the inset of Fig. 4.10 b), where the arrow shows the trajectory of the system in the phase-diagram.

Three-body recombination is not the only loss channel affecting the quantum droplet. The other mechanism that is necessary to take into account is indeed the stabilization of the ratio N_1/N_2. As described in the Chapter 2, the system forms a quantum droplet if the atom number of the two components satisfies a well defined ratio: $N_1/N_2 = \sqrt{a_{22}/a_{11}}$. In general this value depends on the magnetic field, but changes very slowly with it and it is always $\simeq 0.7$. The system can sustain small variations of the population imbalance up to a maximum deviation of $\delta N_i/N_i \simeq |\delta a|/a_{ii}$. Any excess of atoms beyond this threshold is not bound to the droplet, and expands like a gas. The theoretical population imbalance, as well
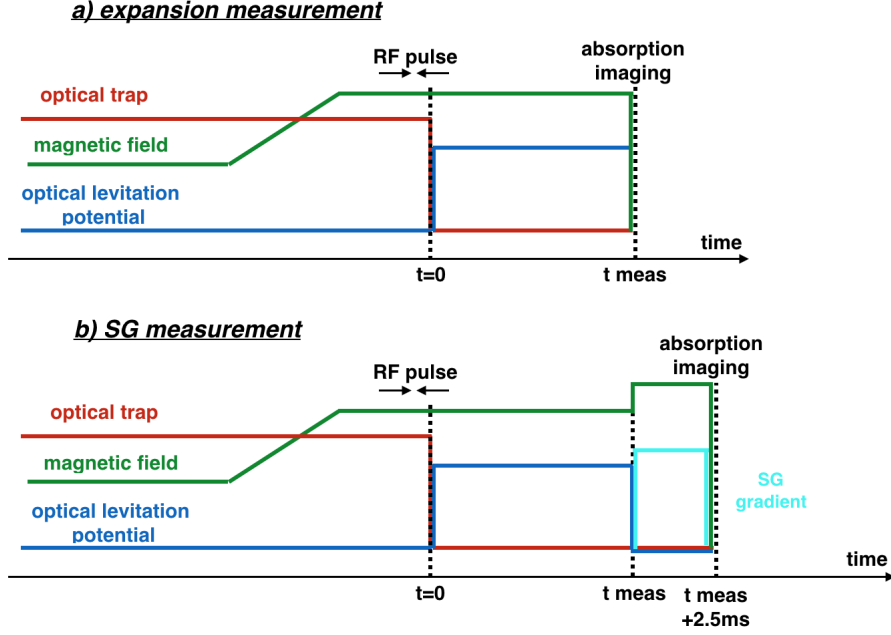
Figure 4.9: Experimental sequence for both measurement schemes performed. a) measurement of the droplet size: after having performed the evaporation in the optical trap, the BEC in $|1, -1\rangle$ is transferred into an isotropic dipole trap (red), the magnetic field is ramped to a value that fulfills the collisional constrains necessary to reach the droplet phase. We then create the mixture making use of a $\pi/2$ RF pulse. At the end of it we switch off all the traps and we acquire the density profile after a variable time t_{meas}. b) SG experiment. The sequence is the same as in a) until $t = t_{meas}$, at this time we increase the magnetic field going out from the droplet regime and we shine a magnetic gradient to separate the two clouds. Absorption imaging is performed after 2.5ms from t_{meas}, at this time the two clouds are spatially separated.

as the maximum deviation, is reported in panel c) of Fig. 4.10. Taking into account this mechanism we can better understand the evolution of the atom number. We start from a balanced mixture with a population imbalance $\simeq 1$ and so larger than the equilibrium one. This value has been chosen in order to maximize the lifetime of the system. Due to the three-body losses, N_1 drops quickly and for this reason the population imbalance becomes smaller than 0.7. At this point also this second losses channel comes into play: the droplet releases atoms in state 2 to keep the population imbalance close to the equilibrium value. The difference between the two losses mechanisms is that in the three-body losses atoms acquire a huge momentum in the inelastic collision and so are expelled from the system, while the second one forces atoms in state 2 to evaporate away from the droplet appearing as a thermal cloud around the self-bound state. For this reason we fit the density profile acquired in both the droplet expansion and SG measurements procedure with a double gaussian distribution:

$$n(x, z) = A_1 e^{-(x-x_0)^2/2\sigma_x^2 - (z-z_0)^2/2\sigma_z^2} + A_2 e^{-(x-x_0)^2/2\Sigma_x^2 - (z-z_0)^2/2\Sigma_z^2} \tag{4.19}$$

where $\sigma = \sqrt{\sigma_x \sigma_z}$ represents the measured droplet size while $\Sigma = \sqrt{\Sigma_x \Sigma_z}$ is the size of the unbounded thermal cloud. The droplet atom number is estimated by the integral of the fitted gaussian function and for this reason, it is proportional to $A_1 \sigma_x \sigma_y$.
In principle the self-bound state should be affected by another loss channel provided by the so-called "self evaporation" described in Chapter 2. According to this mechanism a droplet is expected to expel atoms to dissipate the excitation energy. Atoms released in this way should increment the cloud surrounding the self-bound state. However, since three-body
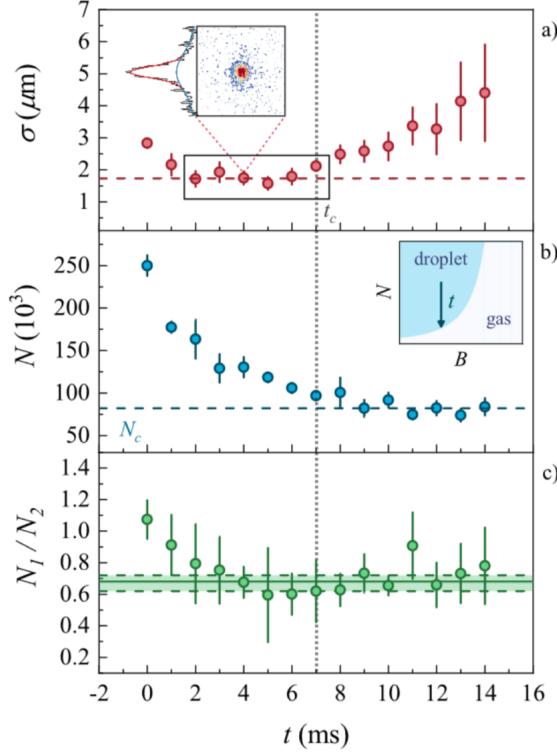
51

Figure 4.10: Time evolution of $\sigma(t)$ (a), N (b), and the ratio N_1/N_2 (c) in the droplet phase at B=54.45 G. The inset in (a) reports the density profile of the droplet after some expansion time, together with the fitted bimodal function described in the text. In the inset in (b), we draw a sketch of the trajectory followed by the system in the mixture phase diagram during the time evolution, due to three-body losses. The dashed line in (a) is the average of σ on the plateau identified by the rectangle. The dashed line in (b) is the critical atom number N_C, measured as the average of N for $t > t_C$. In (c), the solid line represents the theoretical equilibrium value $N_1/N_2 = \sqrt{a_{22}/a_{11}}$, and the green area between the dashed lines includes the allowed deviations $\delta N_i/N_i$(see the first chapeter). The error bars represent the statistical uncertainty and correspond to one standard deviation.

losses denominate the loss dynamics observed so far, it has not been possible to clearly distinguish a self-evaporation contribution.

When the system exits from the droplet phase, all the losses mechanism are stopped. As it is possible to see in Fig. 4.10, as well as in Fig. 4.11, after t_C the atom number and the population imbalance remain constant. For this reason, in order to compare the experimental data with the equilibrium properties described in Petrov's paper, we can define the following variables. The critical atom number is measured as the averaged of $N(t)$ for t larger then t_C. The equilibrium population imbalance is obtained on the average of $N_1/N_2(t)$ for t larger than t_C. The droplet equilibrium size is measured as the averaged size during the plateau highlighted by the rectangle in Fig. 4.10 and Fig. 4.11. The boundaries of the plateau are defined as those points where the size at the next/previous time exceeds the average on the plateau by more than its standard deviation. In Fig. 4.12 we report the experimental data describing the equilibrium properties defined here, above in comparison with the Petrov's theory. In particular in the panel a) the measured size is compared to the theoretical expectations for $N_C \leq N \leq 2N_C$ (red colored area). In panel b) we plot the measured critical atom number and the theoretical N_C for stable (solid line) and metastable droplet (dashed line), i.e. $\tilde{N} = 22.55$ and $\tilde{N} = 18.65$ respectively. Finally in panel c)
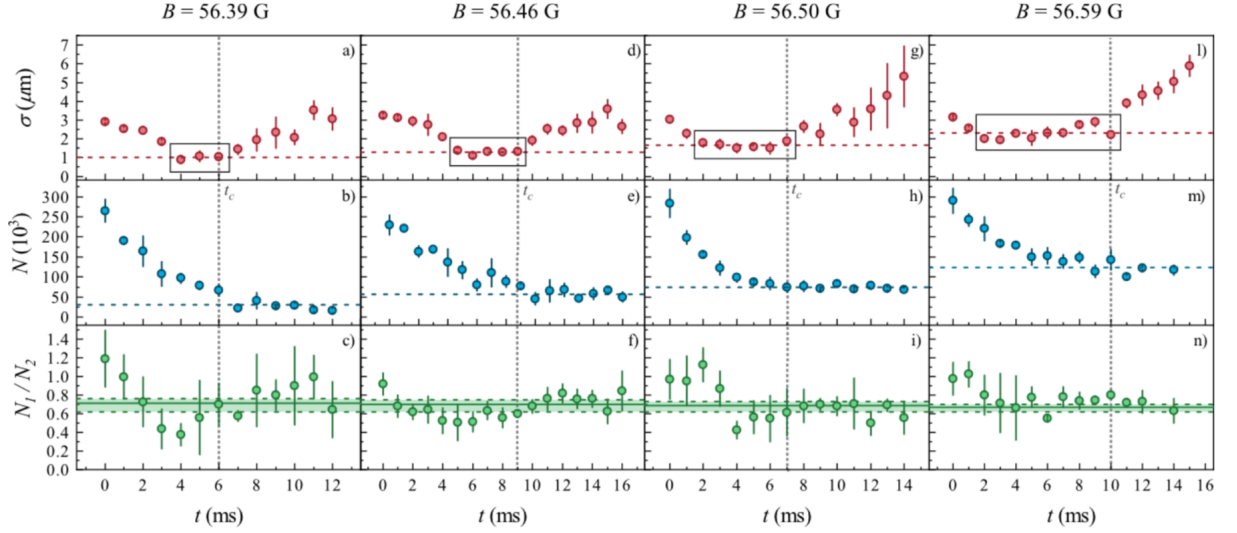
Figure 4.11: We report here the experimental data acquired for different values of the magnetic field. In the upper raw are reported the evolutions of the droplet size, in the central one $N_{tot}(t)$ while in the bottom raw the dynamics of the population imbalance.

we compare the equilibrium population imbalance obtained from our experimental data to the theoretical one $N_1/N_2 = \sqrt{a_{22}/a_{11}}$ taking into account the allowed deviation $\delta N_i/N_i \simeq |\delta a|/a_{ii}$.

As it is possible to see, we find a good agreement with the theoretical predictions, which provides the first experimental confirmation of the theoretical model proposed in [5]. In addition the results presented here represent the first observation of a self-bound mixture in 3D free space. The successful creation of symmetrical quantum droplets is confirmed by the measured aspect ratio σ_x/σ_z of the order of 1 (see Fig. 4.12 panel a) which is always close to 1.

Before concluding this section, I would like to mention that the experimental sequence we use is slightly different for different values of the magnetic field. For $B \geq 56.54$G we switch off the trap at the end of the RF pulse. For smaller values of B, i.e. 56.39 and 56.46G, the cloud is released from the trap before the end of the RF pulse. In this way the mixture completes its formation out of the trap. This is done in order to slow down the dynamics and better characterize the droplet properties. Indeed, for lower magnetic field values the effective scattering length $|\delta a|$ becomes larger and for this reason the system experiences a very fast contraction. As the density increases the losses due to three-body recombination are also increased, so that slowing down the contraction allows to increase the droplet lifetime.

4.5 Dynamical evolution of the droplet

In Fig. 4.11, we observe a dynamical evolution of the size also during the droplet phase before t_c. The mixture is indeed prepared out of equilibrium, the initial size being larger than the droplet nominal size. In addition to that, N is decreasing due to losses, so that σ needs to decrease to preserve the droplet equilibrium density. To understand the timescales of this dynamics and verify if what we observe is compatible with the predictions of Petrov's model, we perform a numerical simulation, using the model introduced in Section 2.3.

To reproduce the preparation of the mixture of the experiment, we start from a condensate in state $|2\rangle$ in the ground state of the external trapping V_{ext}, corresponding to the crossed dipole trap of the experiment, and then we transfer half of the population to state $|1\rangle$, at $t = 0$. The subsequent evolution is obtained by solving Eq. 2.68. We observe the evolution
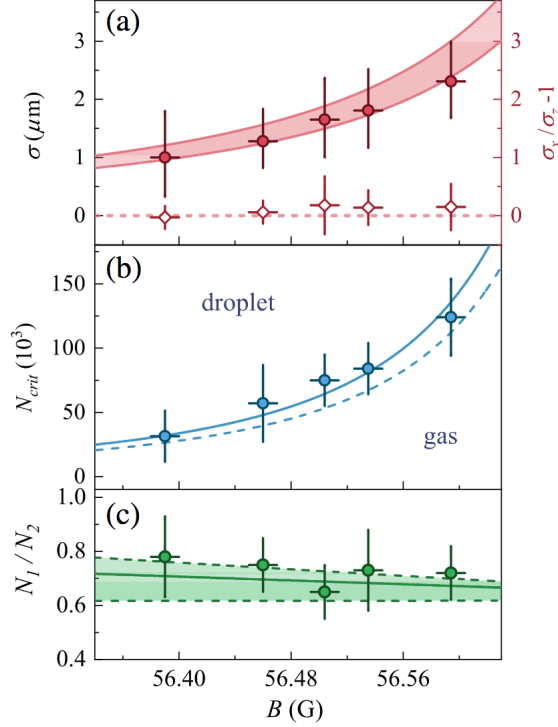
Figure 4.12: Measured values of σ (a), N_C (b) and N_1/N_2 (c) as a function of the magnetic field B. In (a), we also report the aspect ratio σ_x/σ_y (diamonds). The colored area in (a) corresponds to the theoretical prediction for σ $N_C \leq N \leq 2N_C$. The curves in (b) correspond to the predicted critical atom number for the metastable (dashed) and stable (solid) self-bound solutions. In (c), the theoretical curves are obtained as $N_1/N_2 = \sqrt{a_{22}/a_{11}}$ taking into account the allowed deviation $\delta N_i/N_i \simeq |\delta a|/a_{ii}$. The vertical error bars correspond to the statistical uncertainty. The horizontal ones are due to the uncertainty in the magnetic field calibration. All error bars correspond to one standard deviation.

of the mixture, and we fit the density profiles as in the experiment. As shown in Fig. 4.13, in the first part of the evolution, up to more or less 8 ms, we find a very good agreement with the data. At larger times, while in the experiment we observe a transition to the gas phase, the mixture is still self-bound in the simulation. A better agreement at large times is obtained by increasing the value of K_{111} to twice its measured value (dotted line), which is still compatible with the error bar in the measurement of the loss rate (see Appendix 1).

We also compare the observed evolution with the equilibrium droplet size predicted in Petrov's theory. We calculate the droplet radius $R/\sqrt{2}$, where R is defined according to Chapter 2, as a function of the measured atom number at each time (dashed line). The behavior of $\sigma(t)$ is thus explained by a contraction of the mixture to its equilibrium size plus an oscillation on top of that.

Interestingly, despite the limited lifetime, the contraction dynamics is fast enough to allow us to observe the droplet close to its equilibrium configuration. This justifies the comparison with the results of Petrov's theory performed in the previous section.

In Fig. 4.14 we also report the comparison between the data for $\sigma(t)$ and the result of the numerical simulations for all the measured values of B. When the mixture is created in the dipole trap, i.e. for $B > 56.5G$, the simplified model used in the simulations does not take into account the fast initial contraction of the cloud which happens during the RF transfer. For this reason we need to introduce a shift Δt to superimpose at short times the theoretical curve on the experimental data. It is typically $\Delta t \simeq 1ms$. For the smallest fields, where the
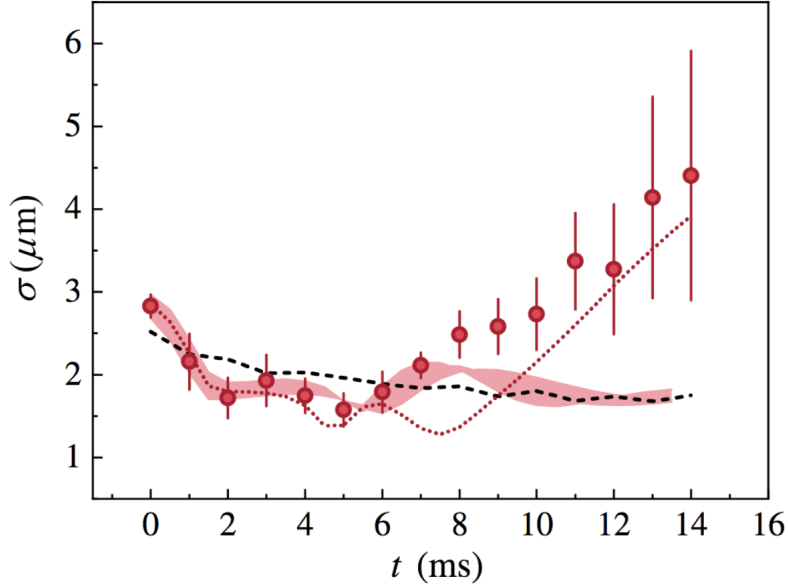
Figure 4.13: Evolution of the droplet size σ for B=56.54(1) G compared with the numerical simulation for $N = 250(50)\ 10^3$ atoms, $K_{111}/3! = 9 \mathrm{x} 10^{-28} cm^6/s$ (colored area), $N = 250\ 10^3$ and $K_{111}/3! = 18 \mathrm{x} 10^{-28} cm^6/s$ (dotted line). The dashed line is the equilibrium size according to Petrov's theory, calculated as explained in the text.

mixture is formed out of the trap, $\Delta t = 0$ due to the slowest initial contraction.

While in the initial part of the time evolution the simulations always reproduce pretty well the dynamics observed in the experiment, we find that at large times the agreement changes as a function of the magnetic field B. For the smallest B, the result of the simulation is compatible with the experimental data within the error bars (Fig. 4.14 a). For larger magnetic fields, we need to increase the value of K_{111} in the simulations to reproduce the droplet-to-gas transition observed in the experiment. For the data shown in Fig. 4.13 (B= 56.54(1)G), as well as for B=56.46(1)G, Fig. 4.14 b, and B=56.50(1), Fig. 4.14 c, we obtain a good agreement with the data by setting K_{111} to a value which is still compatible with the uncertainty in the experimental measurement of the loss rate. For the largest B, however, even setting K_{111} to the largest value within the experimental error bars is not sufficient to reproduce the final expansion.

We conclude that a proper modeling of the losses in the system would require a detailed measurement of all the three-body loss rates in the mixture as a function of the magnetic field and also as a function of the density. The densities in the droplet are indeed so large that avalanche effects as described in [42] might come into play. Such a detailed analysis is certainly demanding and far beyond the purposes of this work. Numerical simulations are mainly used here to characterize the typical time scales in the droplet dynamics, which are only slightly modified by losses.

A possible additional source of losses could also be related to the time-averaged optical levitation. The modulation frequency used so far is only slightly larger than the minimum threshold for heating, discussed in Section 3.3. Further investigations on this issue would be necessary to verify the possible relevance of this effect on the lifetime of the droplet.
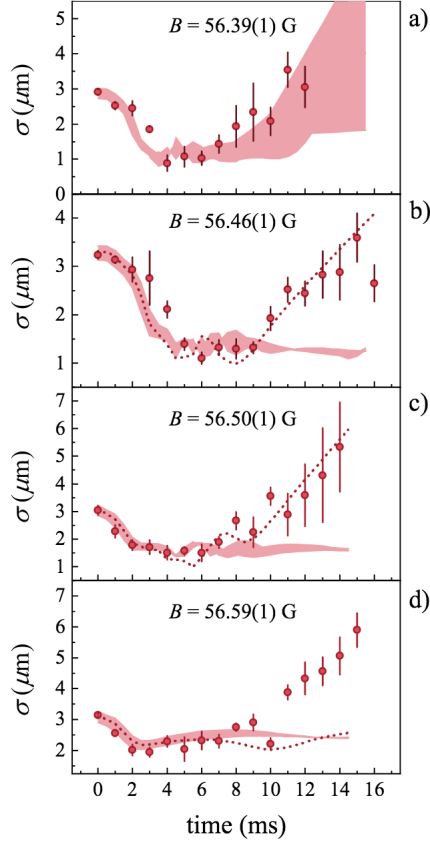
Figure 4.14: Evolution of the size $\sigma(t)$ for different values of B compared with the results of the numerical simulations for the experimental atom number N (considering also the experimental uncertainty) and $K_{111}/3! = 9 \times 10^{-28} cm^6/s$ (colored area). The dotted lines correspond to the simulations for the experimental N and $K_{111}/3! = 14 \times 10^{-28} cm^6/s$ in b) and $K_{111}/3! = 18 \times 10^{-28} cm^6/s$ (c-d).

4.6   Quadrupole oscillations

The measurements reported so far were done for characterizing the equilibrium properties of the droplet. We would like to address the dynamical behavior of this system. The first thing we tried was to measure its collective excitations.

The observation of the monopole mode is complicated by the occurrence of self-evaporation. Indeed for this phenomenon we expect a significant damping of the oscillation in clouds with atom numbers up to 40 times the critical atom number. Since we typically work with smaller clouds, the monopole mode is expected to be always damped. For this reasons in the data previously shown, we can not see any clear oscillation.

We have then also tried to study higher angular momentum modes, such as the quadrupole mode.
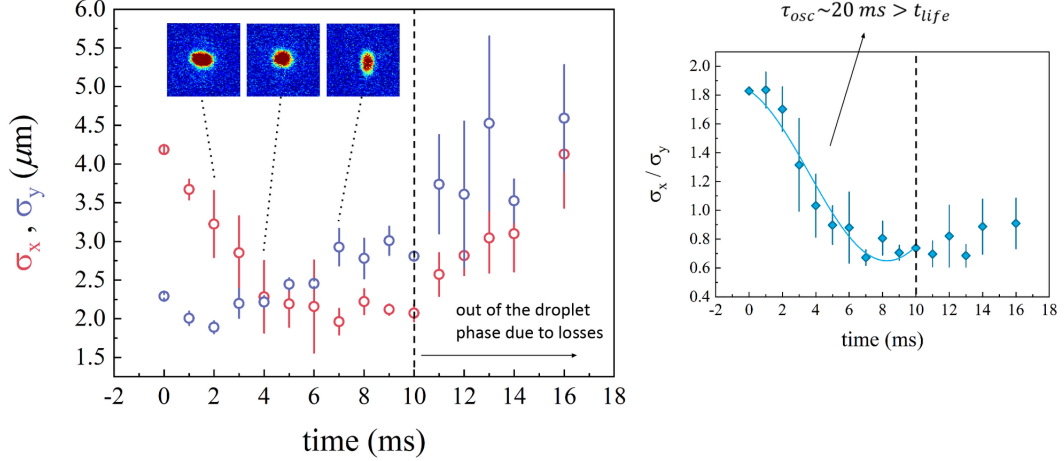
Figure 4.15: Quadrupole oscillation: the system created in an anisotropic trap undergoes oscillation of the aspect ratio. We can clearly observe an inversion of the aspect ratio but we never observe any complete oscillation.

To excite the quadrupole mode we create the initial BEC in state $|2\rangle$, in an-isotropic trap. We then prepare the mixture as usual and we release the system from the trap. In Fig. 4.15 we report the measured values of σ_x, σ_y and of the aspect ratio σ_x/σ_z. We clearly observe an inversion of the aspect ratio and this suggests that the system oscillates under a quadrupole-like oscillation. We cannot characterize a full oscillation, because its period is larger than the lifetime of the system: at $t = 8$ms the aspect ratio is inverted but at $t = 10$ms the liquid-to-gas phase transition occurs and the system starts to expand.

In conclusion, the quantum droplet realized using a mixture of ^{39}K BECs in free space seems not to be a suitable choice to explore the peculiar excitation spectrum predicted for the self-bound system. The three-body losses indeed dramatically affect the lifetime of the system, preventing a complete characterization of such phenomenon. Maybe working in a pure 1D system could help in this sense since the three-body correlation function is reduced with respect to the 3D case [100], so that the expected lifetime should be larger. In 1D anyway the peculiar feature of self-evaporation should not be present, so that one should try to work in 3D with a different atomic species.

Nevertheless, in the next Chapter, we will show that, despite the large limitation coming from the three-body losses, there are still other possible ways to explore the dynamics of quantum droplets: one only needs to find a probe that works on a timescale faster than that of three-body losses.

Chapter 5

Collisions between quantum droplets

In this chapter I report on the experimental study about collisions between two quantum droplets. This kind of experiments are interesting in order to address some properties of the colliding objects, like their energy scales and their liquid-like nature.

To study collisions between quantum drops we implemented on the experimental system a new optical setup that makes use of a repulsive barrier to create two spatially separated BECs (see Sect. 5.1). In Sect. 5.2 I report the experimental sequence used to imprint a controlled and tunable relative velocity to the separate clouds. After that I introduce the experimental results obtained for the collisions (see Sect 5.3). The discussion of the results and the comparison with theoretical predictions is discussed in Sect. 5.4.

5.1 Creation of two colliding droplets

5.1.1 Green barrier

To create a repulsive barrier able to split the initial condensate into two parts, we use green light at 532nm obtained doubling infrared (IR) light at 1064nm, by second harmonic generation. The optical setup is depicted in Fig. 5.1. The IR light coming from a Mephisto Mopa, after passing through an optical isolator, is focused by a $f = 50$mm lens inside a non-linear crystal. After optimizing the coupling of the input IR light in the crystal as discussed in a previous thesis [101], we obtain up to 2 W of green light, starting with $\simeq 18$W of IR light.

The green and the IR light are then collimated by a second lens with $f = 50$mm and then the two wavelengths are separated by two dichroic mirrors. The IR light is coupled into a high power optical-fiber for the optical gravity compensation described in Chapter 3. The green light instead passes through an AOM used for intensity stabilization and then it is coupled into another optical-fiber. At the fiber output the beam waist is $\simeq 900 \mu$m. The optical setup for the realization of the barrier is very simple: with two cylindrical lenses we magnify the beam along one direction by a factor 8, obtaining a waist of 7mm in the largest direction. The beam is then focused on the atoms by a 300mm cylindrical lens.

The green barrier propagates vertically (z axis) parallel to the vertical IR beam, and it is focused along the x axis (Fig. 5.2 b). The expected waist is $w_x \simeq_x 10 \mu$m. Along the other horizontal direction (y) the beam has a large waist $w_y \simeq 1$ mm.

The last lens that focuses the beam on the atoms is mounted on a translational stage, that we use to position accurately the focus of the beam onto the atoms. To verify the alignment of the beam on the atoms we perform the following measurement: first we measure the trapping frequency of vertical IR beam along the x direction finding $\omega_{IR} = 2\pi \times 73(3)$Hz. Then we rise up the barrier splitting the BEC in two parts and we measure the trapping frequencies

in each of the two wells, finding on average $\omega_{DW} = 2\pi \times 147(2)$Hz. From the knowledge of the power in the two laser beams we can deduce the effective waists at the atoms position. We estimate $w_{IR} \simeq 40\mu$m and $w_{green} = 14(5)\mu$m. The deviation from the expected value con be due to a non perfect alignment on the atoms, which is compatible with the precision of our alignment technique. This discrepancy could also be caused by aberrations of the lens we use.
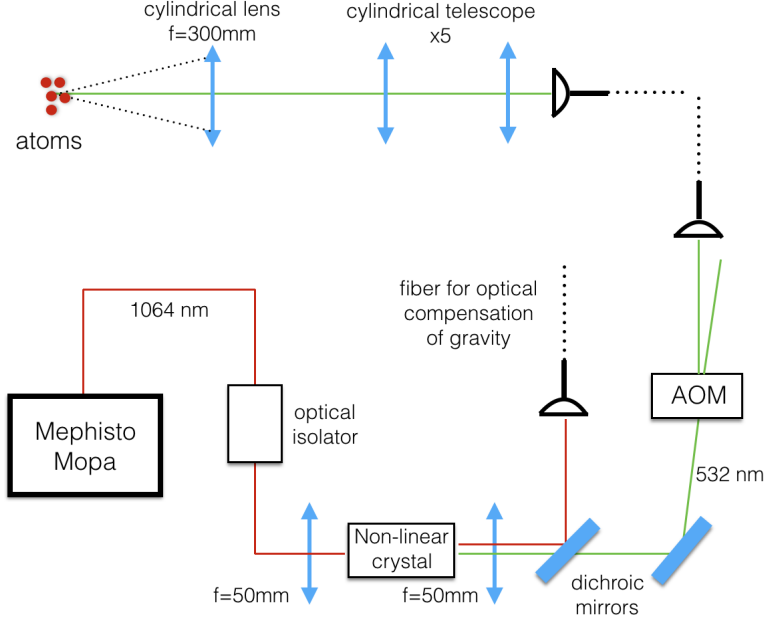
Figure 5.1: Optical set up for the creation of the green barrier as explained in the text

5.1.2 Preparation of two droplets

The sequence to produce two separate droplets is similar to that of a single droplet described in Chapter 4, with the addition of the double-well potential. We start from a BEC in state $|1, -1\rangle$ in the IPG beam. After reaching condensation, we adiabatically turn off the magnetic curvature while rising up the radial beam and the double-well potential provided by the combination of the vertical IR and of the green barrier. After that we, switch off the IPG so that the harmonic confinement along the x axis is provided only by the vertical beam, resulting in a shallower trapping frequency. The chemical potential of the BEC in the Thomas-Fermi regime is then smaller and it is easier to split the cloud in two parts. The drawback is that the residual confinement in the vertical direction is not sufficient to prevent the atoms from falling out of the trap under the effect of gravity. To solve this we optically compensate for gravity during the switching off of the IPG beam, by ramping up the optical time-averaged potential. The experimental sequence used to load the double-well potential as well as a schematic representation of the trap is reported in Fig. 5.2.

At the end of this sequence the geometry of the trap is a double-well potential along x plus a radial confinement in the y-z directions. The trapping frequency in each well depends on the exact value of the barrier height and it ranges between 100 and 170Hz. While the radial trapping frequency is $\omega_{rad} \simeq 2\pi \times 200$Hz. While loading the atoms in the double-well potential, the magnetic field is ramped to a desired target value and finally the mixture is created on both sides of the double-well, by applying the same RF pulse described in Section 4.2.3.
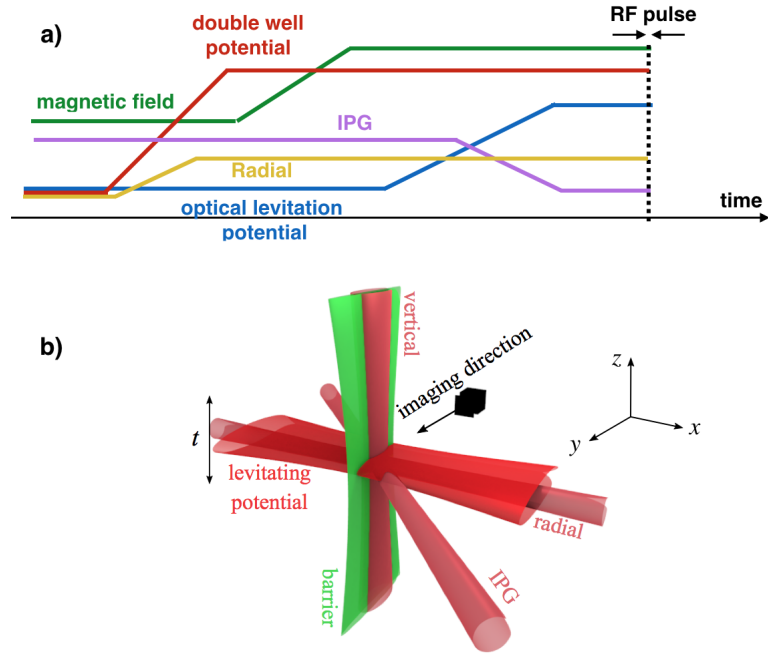
Figure 5.2: a) Experimental sequence for the creation of the two spatially separated BECs. b) Pictorial representation of the trap geometry.

5.1.3 Relative velocity

In order to study collisions, we need to imprint a controlled relative velocity to the droplets. After creating the two separate drops as described above, we turn off all the trapping potentials except for the vertical IR beam. We keep the two clouds in this shallow harmonic trap ($\omega_x = 2\pi \times 93(5)$Hz) for a variable time ΔT, during which they accelerate towards each other due to the opposite forces that attract them towards the center of the trap. After ΔT the vertical beam is turned off, so that the droplets keep moving along x at constant velocity and eventually collide. The experimental sequence is schematically reported in Fig. 5.3. We can then tune the velocity by changing ΔT: the longer ΔT the larger v_x, as long as ΔT is smaller than a quarter of the oscillation period: $\Delta T < 1/4\nu_{IR} \simeq 2.5$ms.
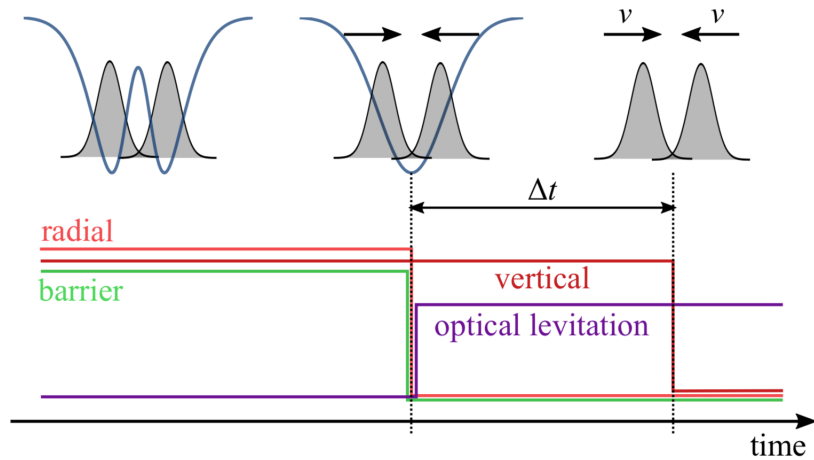

Figure 5.3: Experimental sequence for imprinting a relative velocity to two quantum droplets.

60

5.2   Results of the collisions

5.2.1   Merging vs separation

The outcomes of the collision are mainly two:

- merging: for small velocities, the two droplets stay together after the collision, forming a larger droplet. An example of merging is reported in Fig. 5.4 a).

- separation: for larger velocities, after the collision the two droplets separate again and keep moving in opposite directions, passing through each other. An example of separation is reported in Fig. 5.5 a). We can identify two different situations belonging to this category: elastic scattering when the output velocity is essentially equal to the input one and inelastic scattering where the final velocity is smaller than the initial one.

To characterize the relevant parameters of the collision, we fit the density profiles obtained from absorption imaging, using either a two dimensional double-gaussian function:

$$n(x, z) = A_1 e^{-(x-x_1)^2/2\sigma_{x,1}^2 - (z-z_1)^2/2\sigma_{z,1}^2} + A_2 e^{-(x-x_2)^2/2\sigma_{x,2}^2 - (z-z_2)^2/2\sigma_{z,2}^2} \tag{5.1}$$

,if it is possible to identify two separate density peaks, or a 2D single gaussian function.

$$n(x, z) = A e^{-(x-x_0)^2/2\sigma_x^2 - (z-z_0)^2/2\sigma_z^2} \tag{5.2}$$

In the case of two separate droplets we estimate the average sizes as $\sigma_L = \sqrt{\sigma_{x,1}\sigma_{z,1}}$ and $\sigma_R = \sqrt{\sigma_{x,2}\sigma_{z,2}}$, the distance $d(t) = x_1(t) - x_2(t)$ and the atom number from the integral of the two gaussians, $N_i \propto \sigma_{i,z}\sigma_{i,x}A_i$ (See Appendix 2 for the discussion of atom number calibration). In the case of merging, the average size is $\sigma = \sqrt{\sigma_x\sigma_z}$, $N \propto A\sqrt{\sigma_x\sigma_z}$ while $d = 0$.

In light of these definitions we can discuss with more details the different regimes reported in Fig. 5.4 and 5.5. In Fig. 5.4 after the collision the measured relative distance, represented in the panel b) by the blue diamonds, is compatible with zero. In Fig. 5.5 the distance between the droplets reaches $d = 0$ at the collision time, but then it increases again indicating the following separation. For both cases, we also monitor the evolution of the averaged size σ. This measurement is important to verify if the mixture is still in the self-bound phase during the whole collisional dynamics. From panels c) of both Fig 5.4 and 5.5, we see that there is a finite window between the collision and the droplet-to-gas transition where we can distinguish the outcome of the collision. Finally in panel d) we report the evolution of $N(t)$ that we use to define the atom number at the collision.

In order to characterize the outcomes of the collision as a function of N and v, we need to measure both quantities. We define the atom number at the collision N_{coll} as the atom number at the time when the centers of the two colliding drops are superimposed. To measure it we perform a linear fit of the distance as a function of time during the first part of the collisional dynamics, when the droplets are approaching each others and we can clearly distinguish two peaks in the density profile. From this we can get an estimation of the relative velocity v_{coll} and of the starting distance d_0. The collision time is then given by $t_c = d_0/v_{coll}$. We estimate $N_{coll} = N(t_C)$ by performing a linear interpolation between the two closest data points.

5.2.2   Measurement of the relative velocity

In order to have an independent measurement of the relative velocity, where the trajectory followed by each droplet is not influenced by the presence of the other, we use the following strategy (sketched in Fig. 5.6). The basic idea is to repeat the sequence of Fig. 5.3, but having a single droplet at a time. In order to load the BEC in a single well, we increase the
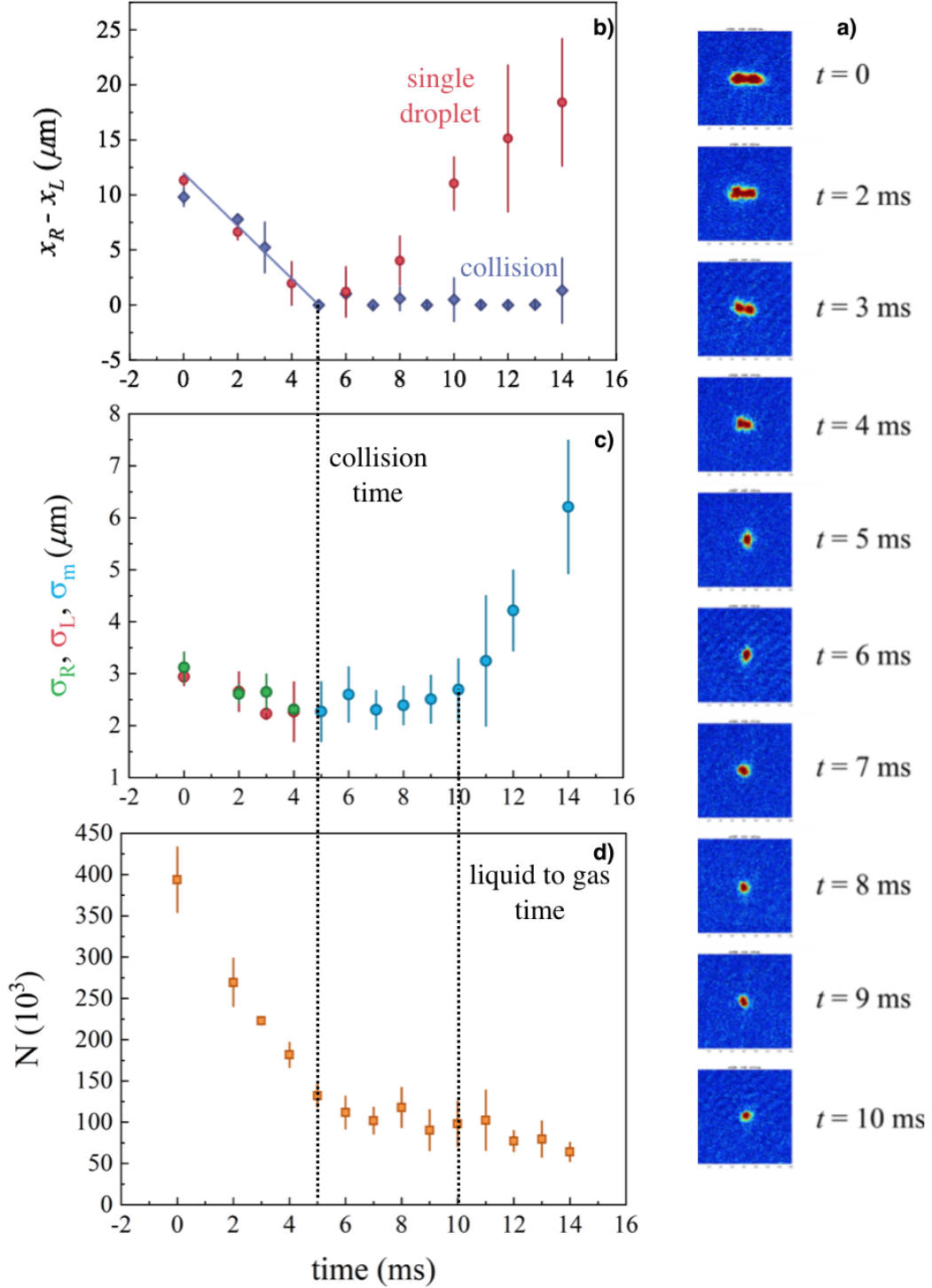
Figure 5.4: Example of a collision between quantum droplets belonging to the merging regime. In the column on the right a) we report some density profiles showing the collisional dynamics typical for the merging case. In the upper panel b) is reported the measured distance during the collision (blue diamonds) in comparison with the one obtained measuring the position of a single droplet at time (red dots). In the central panel c) is depicted the system size evaluated from a gaussian fit of the density profile. In the lower panel d) we can find the measured values of the atom number. Here $v_{coll} = 2.3 mm/s$

height of the green barrier and we move it away from the center of the harmonic confinement
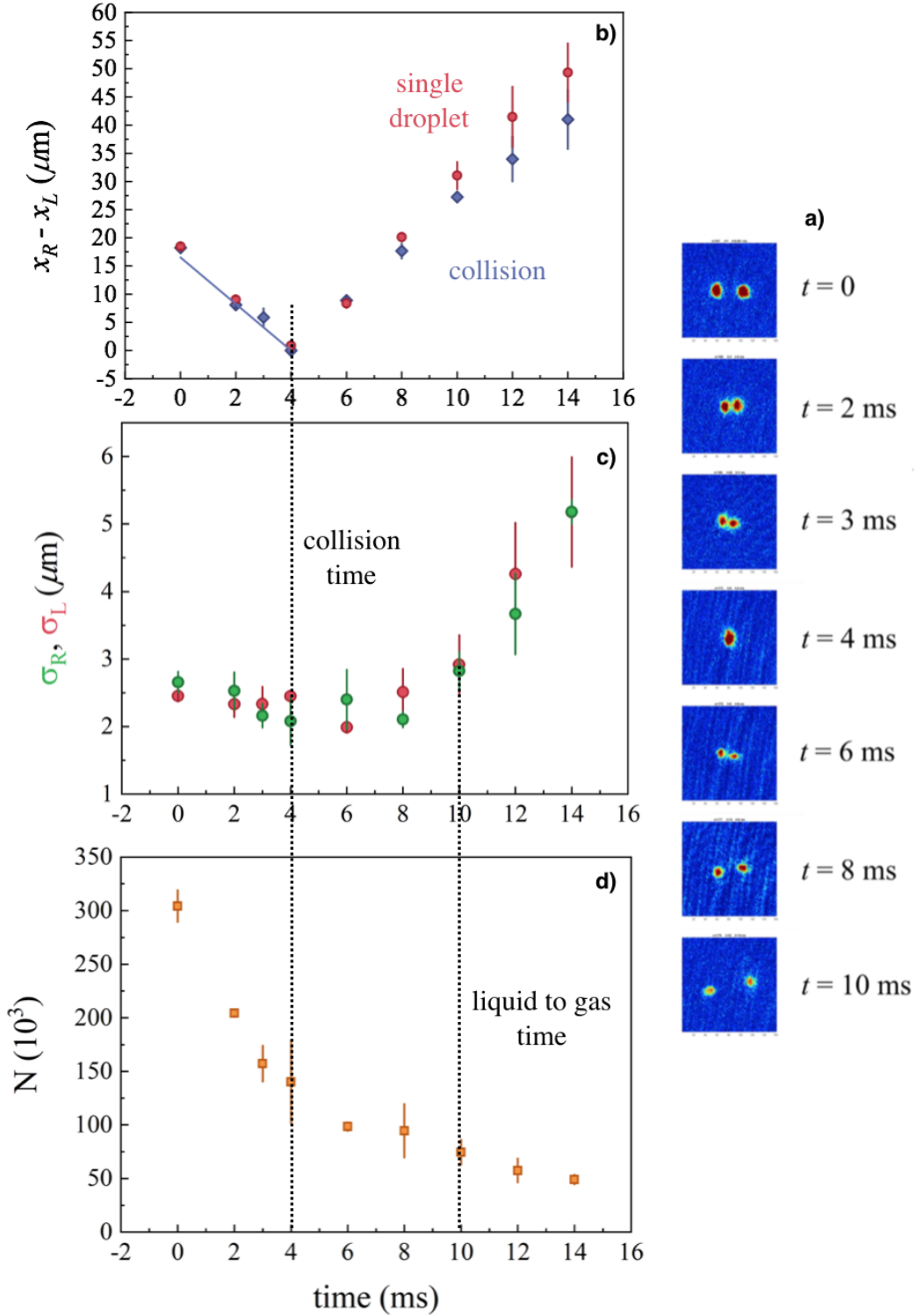
Figure 5.5: Example of a collision between quantum droplets belonging to the separation regime. The panels report the same data as the corresponding ones in Fig. 5.5. Here $v_{coll} = 3.5mm/s$.

provided by the vertical IR beam. In this way the resulting double well potential obtained is imbalanced and all the atoms occupy a single well of the potential but its position is superimposed to that of the corresponding well in the previous configuration (left column of Fig. 5.6). At this point, we follow the same procedure as in the collision measurement. Using

the same vertical trapping potential and the same ΔT, the velocity provided to each droplet will be the same as in the collision (central and right columns of Fig. 5.6).

We measure the position of each droplet as a function of time, as reported, for example, in
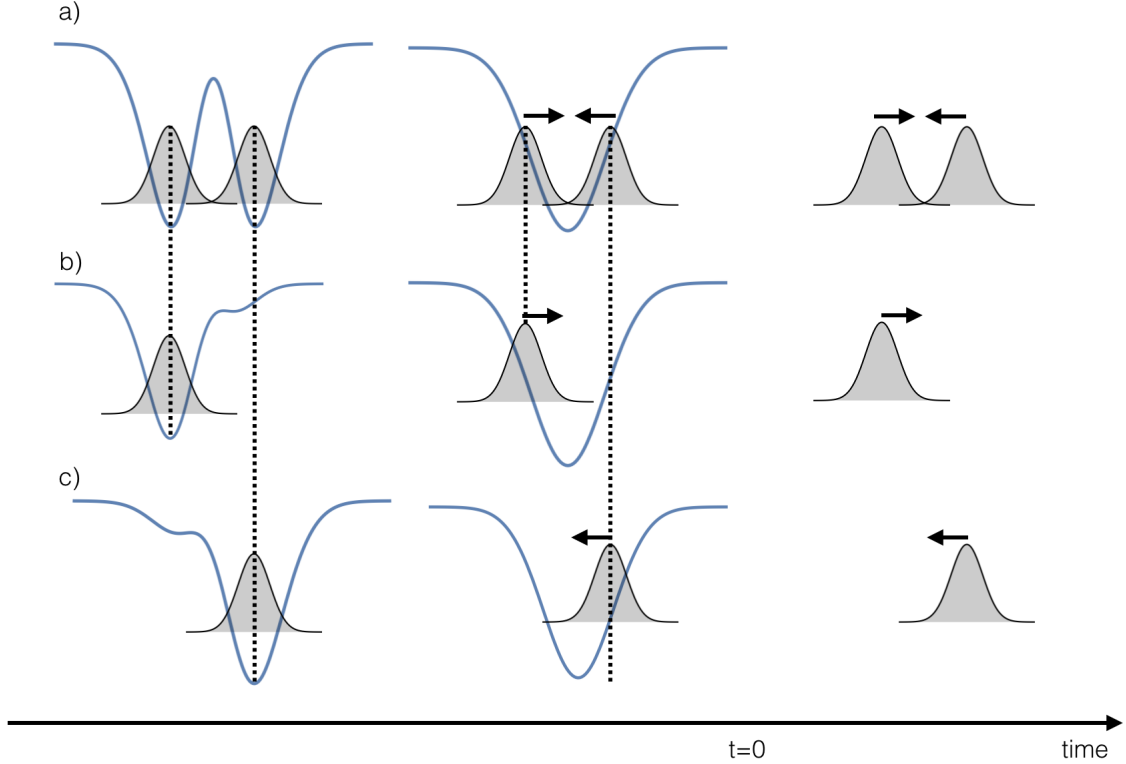

Figure 5.6: a) experimental sequence that we use to study the collision between two droplets. In b) and c) we load the un-balanced double well potential with the BEC that occupies respectively the left and the right well. Changing the barrier high we move the BEC until it is in the same position of the left or right minimum of the potential used in the collision experiment.

Fig. 5.7. Here, t= 0 corresponds to the moment in which the vertical trap is switched off. We evaluate the distance $d(t) = x_R(t) - x_L(t)$ (L for the left-side droplet, R for the right one) and we estimate the value of the relative velocity v_{rel} by performing a linear fit to the data. A typical measurement of the relative velocity between the two clouds is reported in Fig. 5.7. In the specific case of Fig. 5.7, $\Delta T =$1ms and the measured $v_{rel} = 2.8\mu$m/ms. The red dots of panel a) of both Fig. 5.4 and 5.5 represent the experimental distance measured using the technique described above.

The relative velocity we can access ranges from 0.5 to 6 μm/ms, changing ΔT between 0.4 and 1.5ms. The velocity acquired depends not only on ΔT but also on the barrier height: increasing it corresponds to placing the droplets further away from the center of the harmonic potential, so that the force provided by the potential is larger.

We calibrate the dependence of the relative velocity on the intensity of the green barrier and on ΔT. Before switching off the barrier, each droplet is displaced by a distance x_0 from the minimum of the potential provided by the vertical IR beam. Assuming that x_0 is small compared to the waist of the IR beam, we can assume that the potential is harmonic: $V_{IR}(x) = \frac{1}{2}m\omega^2x^2$. This approximation is expected to be valid, since typically $x_0 \simeq 5-10\mu$m, while the waist of the IR beam is $\simeq 40\mu$m. The motion of each droplet inside this potential is then described by the following equation of motion: $x(t) = x_0\cos(\omega t)$ for the position and
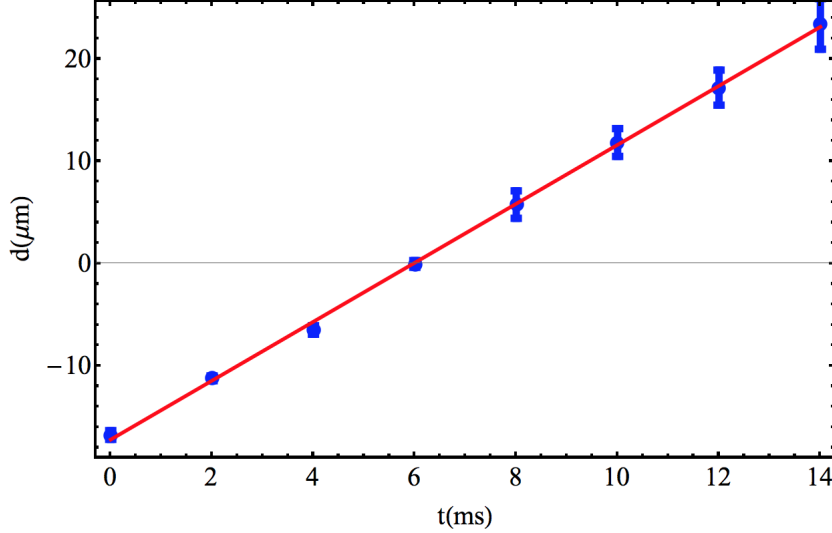
Figure 5.7: An example of measurement of the relative velocity using $\Delta T = 1$ms. The fitted velocity is 2.8μm/ms

$x'(t) = -x_0\omega\sin(\omega t)$ for the velocity, where ω is the harmonic trapping frequency associated to the vertical IR beam along x in absence of the green repulsive barrier. As long as $\Delta t\omega << 1$, the velocity of each droplet is $v = x_0\omega^2\Delta T$.

The relative velocity between the two droplets is then given by:

$$v_{rel} = 2x_0\omega^2\Delta T \qquad (5.3)$$

It scales linearly with ΔT and x_0 while it scales quadratically with the trapping frequency ω. In the experiment we fix the value of $\omega = 2\pi \times 93(3)$Hz and we change ΔT and x_0 to tune the relative velocity. The starting position can be tuned via the barrier height g. The double-well potential along the x direction can be written as:

$$V(x,g) = -V_{IR}e^{-2x^2/w_{IR}^2} + ge^{-2x^2/w_{green}^2} \qquad (5.4)$$

where V_{IR} is the potential depth provided by the IR vertical beam, that we keep constant in the experiment. With a bit of algebra it is possible to calculate the positions of the two potential minima:

$$x_0 = \pm\sqrt{\frac{1}{2}\ln(\frac{gw_{IR}^2}{V_{IR}w_{green}^2})\frac{w_{green}^2w_{IR}^2}{w_{IR}^2 - w_{green}^2}} \qquad (5.5)$$

That can be simplified as:

$$x_0 = \pm\alpha\sqrt{\ln(\beta g)} \qquad (5.6)$$

where the two constants α and β only depend on the waists of the beams and on the intensity of the IR beam. In the last equation, g is in arbitrary units since we can include all the physical constants in the definition of β. For simplicity we use the analog signal in the feedback loop for the intensity stabilization of the green light as a convenient unit to measure the barrier height. In Fig. 5.8 we report the experimental measurement of the initial distance between the two clouds $2x_0$ as a function of the barrier height. The blue curve is the result of a fit to the data using Eq. 5.6. We observe that the experimental data are well reproduced by the model introduced above.

We can now study the dependence of the relative velocity on ΔT. In Fig. 5.9, I report the experimental data for the measured relative velocities obtained with different ΔT. The three colors correspond to three different values of the barrier height. The lines represent the
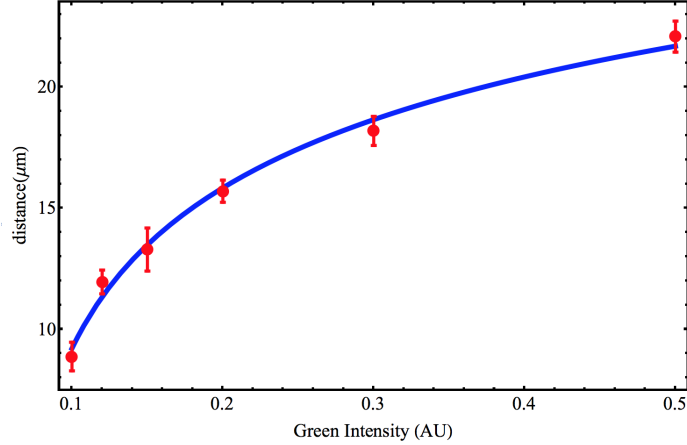
Figure 5.8: Red points: experimental measurement of the separation between the two droplets as a function of the barrier height keeping the harmonic confinement provided by the vertical IR beam constant.

corresponding expected velocities evaluated with Eq. 5.3 where x_0 is calculated using the fitted parameters of Fig. 5.8. The error bars in Fig.5.9 are the statistical uncertainties coming from different repetitions of the same measurement. Also in this case the experimental data well reproduces the model discussed above, indicating that we have a good control on the imprinted relative velocity.

At this point we have two different estimations of the relative velocity. The first one is
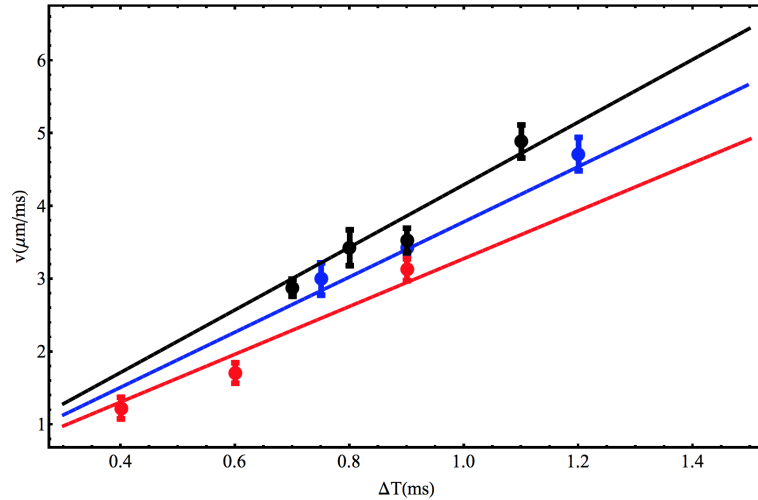
Figure 5.9: Calibration of the relative velocity as a function of ΔT. The three different data set are measured for different values of the barrier height. The lines are the calculated velocities between the two clouds coming from the simple harmonic oscillator model discussed in the text.

provided by v_{coll}, obtained from the first ms of the collisional dynamics and v_{rel} measured with the technique explained here. The two measurements do not always give the same results. The discrepancy between these two measurements could be generated by several effects such as a drift between the two laser beams forming the double-well potentials. Since we do not observe any systematic deviation between the two measurements which could be attributed to a deviation in the droplets trajectory due to the presence of the other during the collision measurement, we conclude that v_{coll} provides a better estimation for the actual

velocity during the collision. We use the measured v_{rel} to estimate the uncertainty on v_{coll}. Defining the velocity discrepancy as $\Delta v = (v_{coll} - v_{kick})/v_{coll}$, we attribute an error to the measurement of v_{coll} by fitting with a gaussian distribution the histogram of Δv and using as estimator of the error of v_{coll} the variance of this gaussian. The result does not depend on the binning of Δv and it is of the order of 20% of v_{coll}. The histogram of the relative velocity as well as the related fit is reported in Fig. 5.10.
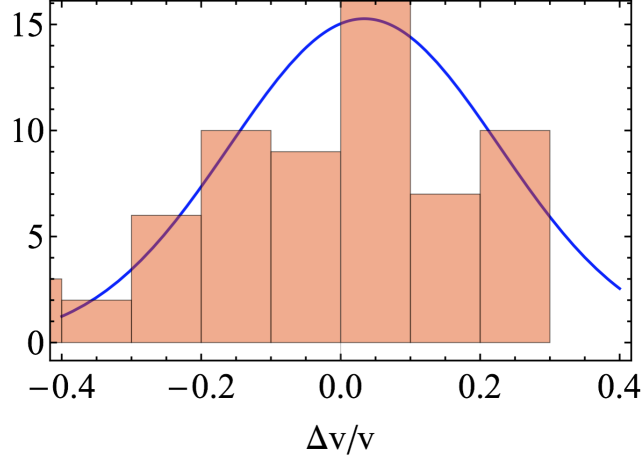

Figure 5.10: Histogram of ΔT and the relative gaussian fit from which we estimate the uncertainty on v_{coll}.

5.2.3 Critical velocity

The results of Section 5.2.1 suggest the existence of a critical velocity separating the two observed regimes: merging for $v < v_C$ and separation for $v > v_C$. In order to detect the position of the threshold and maybe its dependence on the relevant energies scales of the system, we take several datasets as a function of the velocity v_{coll} and of the collision atom number N. Note that, due to strong three-body losses in the system, we can tune the number of atoms at the collision time, N_{coll}. For example, in order to have the same N_{coll} in spite of the different v, the distance at $t = 0$ can be increased proportionally to v_{coll}. In order to explore a broader range of atom numbers, we can also tune an additional parameter, i.e., the magnetic field B. As a matter of fact, if we consider the rescaled units introduced in [5]:

$$\tau = \hbar \frac{3}{2} \frac{\sqrt{g_{11}} + \sqrt{g_{22}}}{|\delta g| n_1^0 \sqrt{g_{11}}} \tag{5.7}$$

$$\xi = \sqrt{\frac{\hbar \tau}{m}} \tag{5.8}$$

and

$$n_1^0 = \frac{25\pi}{1024} \frac{(a_{12} + \sqrt{a_{11} a_{22}})^2}{a_{11} a_{22} \sqrt{a_{11}} (\sqrt{a_{22}} + \sqrt{a_{11}})^5} \tag{5.9}$$

that is the equilibrium density of atoms in the state 1, we can define a rescaled atom number as:

$$\tilde{N} = \frac{N}{n_1^0 (1 + \sqrt{g_{11}/g_{22}}) \xi^3} \tag{5.10}$$

which depends on the magnetic field via the intra and inter species coupling constants g_{ij}. The parameter $\tilde{N}$ is the one that defines the shape of the colliding wavefunction and for this reason it is the parameter that actually distinguishes the compressible regime, characterized

by a gaussian-like density profile, from the incompressible one where the system displays instead a clear flat-top profile. For this reason we decide to describe the outcomes of the collision as a function of the adimensional units. The velocity between the clouds is then rescaled as:

$$\tilde{v} = v\frac{\tau}{\xi} \tag{5.11}$$

The experimental results for different values of the droplet velocity $\tilde{v}$, defined as $\tilde{v}_{coll}/2e$, and the total atom number at the collision $\tilde{N}$ is reported in Fig. 5.11. The blue dots represent the separation regime, according to the definition reported in Section 5.2.1, while the red ones represent the occurrence of the merging. We can clearly observe the existence of a critical velocity v_C that in general depends on the atom number. In particular for small atom numbers v_C is an increasing function of the atom number. This behavior continues up to $\tilde{N} \simeq 130$, where this dependence seems to be inverted.

The error bars are calculated as follows. For the measurement of the atom number $\tilde{N}$ the
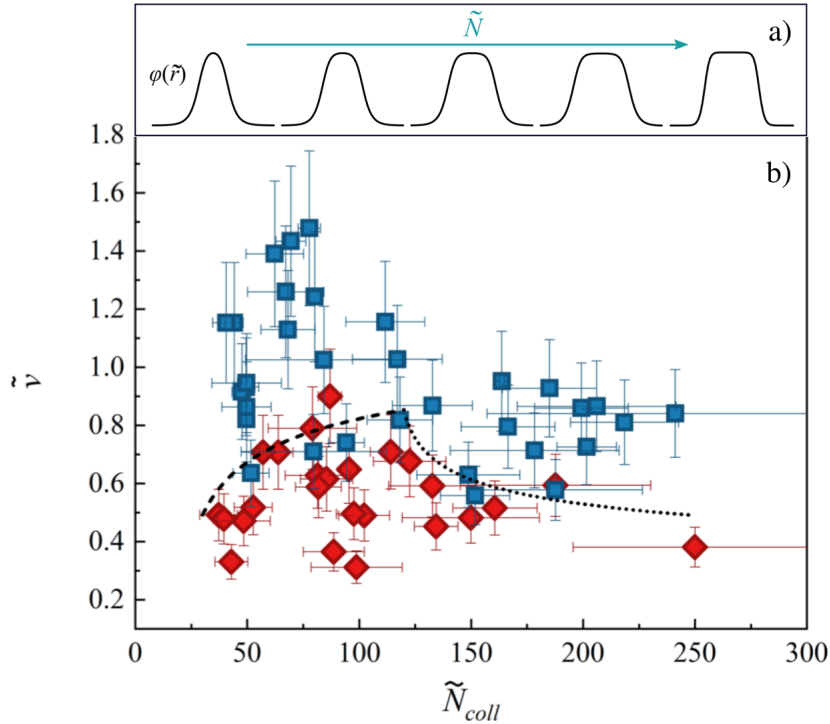
Figure 5.11: Collision regimes as a function of the rescaled velocity $\tilde{v}$ and atom number $\tilde{N}$. Reds corresponds to merging, blue to separation.

error budget takes into account the systemic error provided by the definition of N_{coll}, the calibration of the atom number with the detuned repumper and finally of the an uncertainty on the magnetic field of about 14mG. For the velocity instead, we consider the systematic error due to the difference between v_{coll} and v_{rel}, already discussed in Section 5.2.2 and the uncertainty on magnetic field which enters in the definition of $\tilde{v}$.

5.3 Discussion of the results and comparison with theory

In this final section, we will discuss the comparison between the experimental data and the theory. I would like to stress that all these considerations are preliminary and under investigation.

Despite this, the change in the dependence of $\tilde{v}_C$ on $\tilde{N}$ we observed is very clear and it has

interesting implications that I would like to discuss. I will first try to justify the observed behavior using simple energetic considerations and then I will introduce the ongoing comparison with numerical simulations. Finally I will mention one effect that could affect the collisional dynamics and that will probably require further consideration.

5.3.1 Energetic considerations

In this section I will present a very simple and intuitive picture to justify the observed behavior of $\tilde{v_C}(\tilde{N})$ in Fig. 5.11, based on energetic considerations.

Let us first discuss the regime of large atom number. In this limit, the droplet reaches its saturation density and then it develops an incompressible bulk with uniform density distinguished from a surface where the density decreases to zero (see sketch in Fig. 5.11). I will consider all the quantities in adimensional unities but, for simplicity, I will write them without the $\sim$. The initial energy of the two separated colliding droplets is provided by the binding energy plus the kinetic energy relative to their motions

$$E_{in} = 2E_{bind}(N/2) + E_{Kin} \tag{5.12}$$

where N is the total atom number and E_{bind} the binding energy introduced in Section 2.3. If the two droplets merge in a single one, we expect that the final energy will be given by the binding energy of the merged droplet plus some excitation energy. Since we are considering incompressible droplets, we suppose that the excitation of the droplet will correspond to some surface modes, whose energy will depend on the surface energy E_S (see Section 2.2.4). We thus have:

$$E_{fin} = E_{bind}(N) + E_{exc}(E_S) \tag{5.13}$$

As already introduced in Section 2.2.3, we can decompose the binding energy according to the liquid-drop model: $E_{bind}(N) = E_B N + E_S N^{2/3} + E_C N^{1/3}$. Neglecting the curvature term, that is negligible in the limit of large N, and by imposing energy conservation we get:

$$2E_B(N/2) + 2E_S(N/2)^{2/3} + E_{Kin} = E_B(N) + E_S(N)^{2/3} + E_{exc}(E_S) \tag{5.14}$$

The contribution of the bulk energy is cancelled because $E_B(N) = 2E_B(N/2)$. We can then conclude that the relevant energy scales in the large N regime are just the kinetic energy and the surface energy. We can thus use the same Weber number criterion already introduced in the context of classical drops (see Section 2.5) to predict the critical condition for merging. Imposing $E_{kin} \simeq E_S N^{2/3}$, we get the following scaling of the critical velocity with N:

$$v_c(N) \propto N^{-1/6} \tag{5.15}$$

This scaling is represented by the dotted line in Fig 5.11.

Concerning, instead, the case of small N, energetic considerations are a bit more difficult. Indeed, in this regime, the liquid-drop model is no longer valid and the excitation spectrum of the droplet is not trivial. In order to justify the increasing trend of v_C with $\tilde{N}$, we can first consider the simple case of the scattering between a single atom and the droplet. In this picture, due to its negative chemical potential, the droplet plays the role of an attractive potential well for the incoming atom. The probability that it gets trapped in the self-bound state depends on its velocity. Increasing the atom number inside the droplet corresponds to a deeper potential well, so that the atom needs a larger velocity to be able to escape from the droplet. More quantitatively, we can say that in this regime the relevant energy scales is the total binding energy. We can thus guess that the critical velocity can be obtained by imposing $E_{kin} \simeq E_{bind}$ which means

$$v_c(N) = \sqrt{2\frac{E_{bind}(N)}{N}} \tag{5.16}$$

which is represented by the dashed line in Fig. 5.11.

Although the discussion reported here represents a very simplified model of the complex collisional dynamics, we observe that these energetic considerations reproduce pretty well the experimental data of Fig. 5.11, meaning that at least the qualitative outcomes of binary collisions are mainly driven by these energy scales.

5.3.2 Numerical simulations

In order to better understand the complex phenomenon of the collision between two quantum droplets, we perform dynamical simulations of the system in collaboration with the theoretical group of Trento (Dr. A. Gallemì, Dr. A. Recati). These simulations have been performed
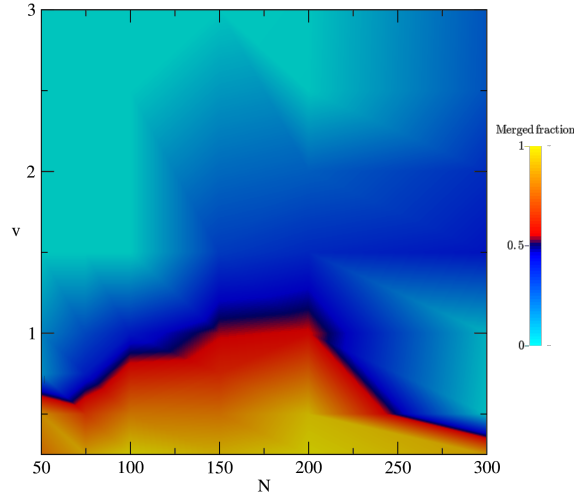

Figure 5.12: Merging fraction in the phase diagram $\tilde{v}$, $\tilde{N}$

using the a-dimensional modified Gross-Pitaevski equation from [5]:

$$i\frac{\partial}{\partial t}\phi = (-\frac{1}{2}\nabla^2 - 3|\phi|^2 + \frac{5}{2}|\phi|^3)\phi \qquad (5.17)$$

We prepare two quantum droplets with $\tilde{N}/2$ atoms each, separated by a certain distance $\tilde{d}$ to ensure that there is no overlapping between their wavefunction. We provide them a certain velocity $\tilde{v}$, so that they move towards each other. We let them evolve according to Eq. 5.17 and then we observe the result of the collision. The velocity is inserted as a phase kx with k such that $1/2mNv^2 = \hbar^2 k^2/2m$. In the rescaled units of Petrov (using the definition of τ and ξ of Eqs. 5.7 and 5.8) we have $kx = \tilde{v}\tilde{x}$. The initial wave-function is thus provided by:

$$\phi(\tilde{x},\tilde{y},\tilde{z}) = \phi_0(\frac{\tilde{N}}{2},\tilde{x} - \tilde{d}/2,\tilde{y},\tilde{z})e^{i\tilde{v}\tilde{x}} + \phi_0(\frac{\tilde{N}}{2},\tilde{x} + \tilde{d}/2,\tilde{y},\tilde{z})e^{-i\tilde{v}\tilde{x}} \qquad (5.18)$$

where $\phi_0(\frac{\tilde{N}}{2})$ is the ground state wave-function for a quantum droplet with $\tilde{N}/2$ atoms. In order to distinguish between the merging and separation regimes, we compute the fraction of atoms that remain in the center of mass of the collision, that we identify as the "merged fraction". A color plot of the merged fraction is reported in Fig. 5.12.

The theoretical phase diagram clearly shows two different scaling of $\tilde{v}_c$, analogously to the experimental results, but the crossing over between the compressible and incompressible regime occurs at larger atoms number $\tilde{N} \simeq 200$. Trying to deduce an a-priori criterion for the onset of the incompressible regime, we could look at the dependence of the chemical potential on the atom number $\tilde{N}$. In the incompressible regime one indeed expects that the chemical potential scales as $\tilde{N}^{-1/3}$. According to the liquid drop model discussed in Chapter 2, this

condition is fulfilled for atom numbers larger than $\tilde{N} \simeq 200$, in good agreement with the theoretical results of Fig. 5.12. In this limit indeed the energy contribution provided by the curvature term $E_C \tilde{N}^{1/3}$ becomes negligible with respect to the energy hosted by the surface and the bulk of the droplet.

Interestingly, in this limit quantum droplets behave analogously to a classical liquid and the Gross-Pitaevskii equation fully recovers the hydrodynamic evolution observed in the collision between classical drops. In the simulations we indeed observe the same stages of the collisional dynamics as observed for example in [59] (see Fig. 5.13): the formation of a neck connecting the two drops, the stretching in the direction perpendicular to the collision axis and finally depending on whether the surface tension is large enough to balance the velocity flux created in this stage or not, merging or separation occur.

Differently from simulations, experimental data display a maximum of $\tilde{v}_c$ around $\tilde{N} \simeq 130$.
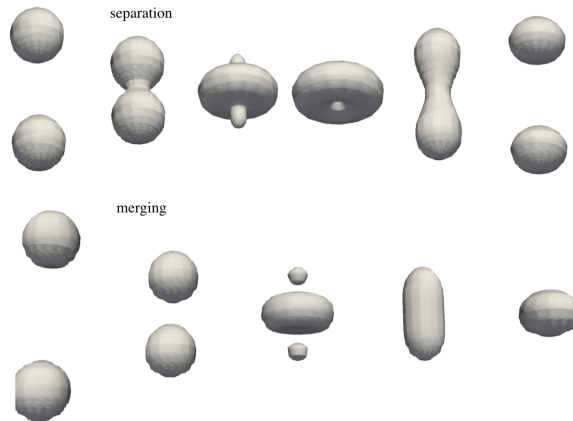

Figure 5.13: Above some snapshoots of a simulations where the two colliding drops pass through each other. As it is possible to see, the kinetic energy flow is not compensated by the surface tension and for this reason appears an hole in the density profile. As a consequence the merging is prevented. Oppositely, below the kinetic flow is compensated by the surface tension and thus no toroidal profile appears in the dynamics , i.e. the two drops merge.

In order to understand this discrepancy we need to characterize the effect of the three body losses . We then inserted in the GPE of Eq. 5.17 a dispersive term provided by $-K|\phi|^4$. We choose the value of K that better reproduces the experimental decay. This is certainly an approximation for the actual loss dynamics described in Chapter 4, where different loss channels for the two species were identified, but it could help us to understand the effect of losses during the collision.

We analyzed the result of the simulations in the presence of three-body recombinations with the same qualitative criterion used in the experiment to distinguish between merging and separation. The corresponding results are reported in Fig. 5.14, in comparison with the experimental ones. We observe that the addition of three-body losses in the simulation is sufficient to shift the onset of the incompressible regime to values of $\tilde{N}$ comparable to the experimental one and the overall behavior of $\tilde{v}_c$ is in this case in very good agreement with the experimental results.

Although this first preliminary comparison between the experiment and the numerical simulation seems to confirm the qualitative picture obtained with the energetic consideration of the previous section, a more detailed analysis is still under way. The effect of losses, for example, requires some careful considerations. We are currently performing more quantitative estimations of their effect in order to exclude that the decrease of $\tilde{v}_c$ at large atom number is justified by an increase in the three-body losses corresponding to the increased density and
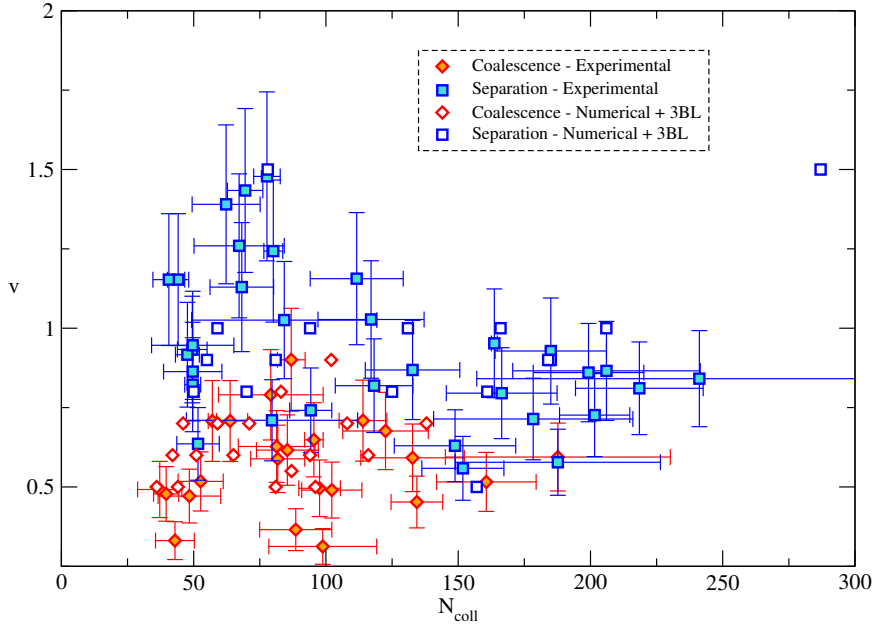
Figure 5.14: Comparison between experimental data and numerical simulations including three-body recombination. The filled blue or red points represent the experimental data, while the empty ones are the numerical simulation.

not to the actual onset of the incompressible regime. In addition to this, we would like to introduce in the simulations the quenched preparation of the droplets typical of our experimental procedure, in order to consider the possible effects of the collective excitations already present in the two colliding droplets.

A more refined comparison between experiment and simulations along the direction mentioned here should allow us to provide conclusive results about the explored dynamical properties of the droplets and hopefully to report a first evidence of a liquid-like behavior.

5.3.3 Effect of the impact parameter

In the model presented in Sect. 5.1.3 and in 5.2.2, to characterize the technique used to imprint a relative and controllable velocity to the droplets, we neglected any possible misalignment of the trapping beams. Here we will evaluate the effect on the impact parameter b of a finite angle α different from $\pi/2$ between the direction of the imaging and the direction of the tight confinement in the elliptical trap provided by the vertical IR beam. We will also take into account the effect of a finite displacement of the center of the trap provided by the latter beam.

We will make use of two different reference frames. The first one has as main axes the radial beam and the imaging beam, we call these two direction as x and y respectively. The second one is provided by the two main axes of the vertical IR beam, we will call these x_1 and x_2. A sketch of the system is reported in Fig. 5.15.

The two systems of coordinates are related by:

$$x_1 = x\cos(\alpha) - y\sin(\alpha) + A \tag{5.19}$$

$$x_2 = x\sin(\alpha) + y\cos(\alpha) + B \tag{5.20}$$

where A and B represent the displacement between the centers of the two reference systems. In the limit of small displacement of the droplet from the center of the trap, we can approximate the potential provided by the vertical IR beam as:

$$V(x_1, x_2) = -V_0 + 4\pi^2 \frac{1}{2} m x_1^2 \nu_1^2 + 4\pi^2 \frac{1}{2} m x_2^2 \nu_2^2 \tag{5.21}$$
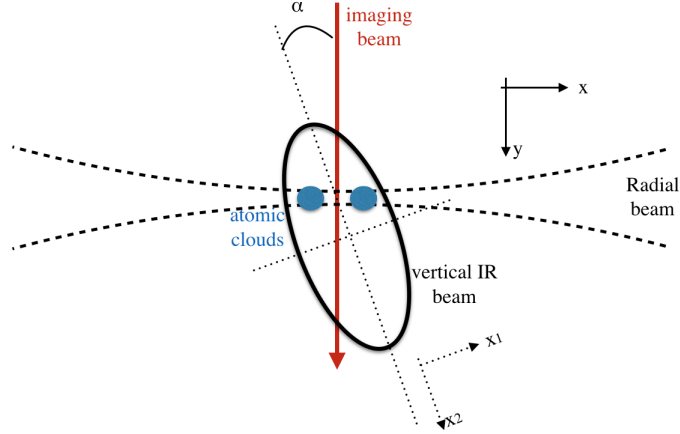
72

Figure 5.15: Sketched of the geometry of the system, we also report the two different reference systems introduced in the text.

where ν_1 and ν_2 are the trapping frequencies along the two axes of the trap. They are related by $\nu_1/\nu_2 = w_2/w_1 \simeq 3$ since the two waists of the IR beam are 39μm and 105μm respectively. Substituting Eq. 5.19 and 5.20 into Eq. 5.21, we can calculate the optical potential in the x-y coordinates, which are those used to described droplet dynamics. In the limit of $\Delta T \ll 1/\nu_1$, we can calculate the relative velocity along x and y. Supposing that the two droplets are located at t=0 at $(\pm x_0, 0)$, we get

$$v_x^R = \frac{F_x(x_0,0)}{m}\Delta T - \frac{F_x(-x_0,0)}{m}\Delta T = \Delta T(2\nu_1^2 x_0\cos^2(\alpha) + 2\nu_2^2 x_0\sin^2(\alpha)) \qquad (5.22)$$

$$v_y^R = \frac{F_y(x_0,0)}{m}\Delta T - \frac{F_y(-x_0,0)}{m}\Delta T = 2\Delta T\cos(\alpha)\sin(\alpha)(\nu_1^2 - \nu_2^2) \qquad (5.23)$$

We notice that the displacement between the center of the two reference systems (A,B) does not modify the relative velocity. From an auxiliary vertical imaging we can set an upper-bound of 10 deg to the angle α. For this reason and considering the ratio between the two waists, we can approximate in Eq. 5.22 $\cos^2(\alpha) \simeq 1$ and $\nu_2^2/\nu_1^2\sin^2(\alpha) \simeq 0$, recovering Eq.5.3 of the ideal model.
Using the same approximation in Eq. 5.23 we can estimate the distance along y between the two droplets at the collision, which corresponds to:

$$dy = \sin(2\alpha)x_0\frac{\nu_1^2 - \nu_2^2}{\nu_1^2} \qquad (5.24)$$

Considering 10 deg and a value of x_0 between $5-7.5\mu$m, we get dy in the range of $1.5-2.3\mu$m. To estimate the impact parameter, we need to compare dy with the droplet diameter D. Defining a proper value of D is not trivial because it changes in time and it also depends on the specific value of B. We can anyway obtain an upper bound to the impact parameter b, defined as in the classical drops framework, i.e., $b = dy/D$, by considering an averaged diameter of 6μm, which correspond to a b ranging from 0.2 to 0.35. As reported in Section 2.5 an impact parameter different from zero should increases the critical velocity. Despite this the system still remains in the crossing over between coalescence and near head-on separation. The effect on the critical velocity should be anyway of the order of 10% which is anyway smaller then the error of measurement of v_C we perform.

Chapter 6

Conclusions and future perspectives

In this thesis I have described the experimental realization and characterization of a quantum droplet composed by a mixture of bosonic atoms. Thanks to an innovative technique to compensate for gravity, which makes use of a time-averaged optical potential, we were able to observe the formation of this new self-bound state in free space. This allowed to perform a direct comparison between our experimental data and Petrov's theory, which was developed in homogeneous free space. In particular, we verified the existence of this state in the predicted region of inter and intra-species interactions and we found a very good agreement with theoretical predictions. This provides the first experimental confirmation of the theoretical model proposed in [5], proving that the attractive mixture is stabilized by the effect of quantum fluctuations.

Despite being extremely dilute, for large atom numbers, quantum droplets enter a liquid-like incompressible regime, highlighted by the formation of a bulk with uniform density. In the second part of this thesis we explored the crossover between compressible and incompressible regimes by observing the outcomes of the collision between two quantum droplets. For this purpose we implemented an experimental sequence aimed at creating two separate quantum droplets and at imprinting a relative velocity between them. The experimental results suggest the existence of a critical velocity v_c below which the colliding drops merge into a single one, while for larger velocities they separate after the collision. This critical threshold in general depends on the total atom number N and it was found to be an increasing function of N in the compressible regime, while it decreases with N in the opposite incompressible limit. Observing the two different scalings of the critical velocity with the atom number and comparing them with the results of simple energetic considerations and of accurate numerical simulations, we were able to get an insight on the relevant energy scales of the quantum droplets and to obtain the first evidence of their liquid-like behavior in the large N regime. A detailed analysis of these collision measurements is still ongoing and a precise comparison with theory will allow us in the near future to get conclusive results about the explored dynamical properties.

Since the investigation of quantum droplets is a very recent topic in the ultracold atoms community, the experimental observation of several predicted properties is still missing. One of the most interesting and peculiar among them is the so-called self-evaporation. This exotic phenomenon is related to a property of the excitation spectrum of the droplet in the small atom number regime, where the discrete collective excitations are much higher in energy than the particle emission threshold, so that the droplet is expected to automatically evaporate excitations and cool down to zero temperature. The observation of such phenomenon could pave the way to the use of quantum droplets as coolant of other atomic systems like, for example, a fermionic impurity [102]. During my thesis, we tried to study collective oscillations of a quantum droplet to explore its excitation spectrum. The main limitation in our system is related to three-body recombinations, which reduce the lifetime of the droplet before it

undergoes a liquid-to-gas transition when its critical atom number is reached. Due to this effect, the available time window is too short to observe a complete collective excitation of the droplet, as shown at the end of Chapter 4. Other mixtures, like the heteronuclear K-Na mixture studied in [86], could be suitable candidates for the study of such phenomena, due to possibly reduced three-body loss rates. Note that in this case the compensation of gravity would be challenging because it would require to use laser light at a magic wavelength or to implement combined optical and magnetic gradients.

It would also be interesting to investigate the effect of a Rabi coupling between the two components of the mixture. It has been theoretically predicted that the coupling affects the properties of the system and that there exists an energetic instability above a critical Rabi frequency that provokes the evaporation of the droplet [103]. This state has not been observed so far and it can be easily accessed with our setup.

Another promising perspective of our work is to study the formation of quantum droplets in reduced dimensionality. Several theoretical studies have been carried out about this topic discussing the condition for the droplet formation in a pure 1D or 2D systems [104, 105]. In reduced dimensionality the system could have a longer lifetimes, thanks to the reduction of the three-body correlation g_3 in 2D or 1D with respect to the 3D case [100].

An open question regarding the physics of quantum droplets concerns their superfluid properties. Since it is composed by a mixture of BECs, one would guess that the quantum droplet maintains its superfluid nature. Nevertheless the problem is still challenging from both a theoretical and an experimental point of view, because of the finite size of the system. Several techniques, already applied to BECs, could be used to probe the superfluid nature of quantum droplets, like stirring [106] and vortex enucleation [107]. The difficulty in the application of such techniques is related to the very small size of the droplets, which is of the order of 1-3μm. Another possibility to study the superfluid properties is provided by investigation of the early stages of the merging between two droplets. The dynamics of the merging indeed depends on the viscosity of the bulk and it is thus speeded up in the case of superfluid bulks, as already observed with helium clusters [72]. In addition to this, the collisional dynamics between two droplets could be affected by very interesting phenomena related to the interplay of two superfluid components, such as the Andreev-Bashkin effect [108, 109], which were theoretically predicted but so far never tested in experiments.

Chapter 7

Sensitivity function of an atomic interferometer

We are currently working on the realization of an optical lattice with large effective spacing. We can use this system for several proposes, ranging from atom interferometry to the generation of non-classical states.

A fundamental question is to understand how the environmental noise affects the performance of the interferometer. Introducing the so-called sensitivity function $g(t)$ we will estimate the effect of the noise on the system caused by vibrations and frequencies fluctuations of the trapping lasers.

In the first section I will introduce the experimental schemes that we want to implement in order to create non classical states and to realize a trapped atom interferometer. In the second section, I will define $g(t)$ and calculate if for both the experiment considered. Finally, in the last parts of the Chapter, I will apply these functions to some real noise spectral function discussing the sensitivity of our setup.

7.1 Trapped atom interferometry

In this section I will shortly discuss the theory of a BEC in a double well potential.

7.1.1 Two mode approximation

It is well known that a quantum harmonic oscillator has discrete eigenvalues equally separated: $E_n = \hbar\omega(n + \frac{1}{2})$. The effect of rising up a barrier is to reduce the energy difference between the ground state and the first excited one.The two-mode approximation [110, 111] consists in supposing that all other levels will have a very low population with respect to the two low-lying ones. This is valid if all the energy scales of the system (temperature, interaction energy, tunneling energy) are much lower than the separation from the other excited levels, separation which is of the order of the harmonic oscillator energy for the original trap. Using this approximation it is possible to write the many body Hamiltonian:

$$\hat{H} = \int dx \hat{\Psi}^\dagger(x)(-\frac{\hbar^2\nabla^2}{2m} + V_{ext}(x))\hat{\Psi}(x) + \frac{1}{2}\int\int dx dx' \hat{\Psi}^\dagger(x)\hat{\Psi}^\dagger(x')V_{int}(x,x')\hat{\Psi}(x)\hat{\Psi}(x')$$

$$(7.1)$$

assuming that the field operator $\hat{\Psi}$ is restricted to work just on the first and the second energy levels, i.e.:

$$\hat{\Psi} = \Psi_g \hat{a}_g + \Psi_e \hat{a}_e \qquad (7.2)$$

where $\Psi_{g,e}$ are the wave function of the ground state and of the excited state, $\hat{a}_{g,e}$ are the destruction operator of a particle in the ground state or in the first excited one and $g = \frac{4\pi\hbar^2 a}{m}$

where a in this case is the scattering length describing the interaction between two atoms. A picture of the double well potential and of its ground state and first excite one is reported in Fig. 7.1.

A more suitable base to describe the system is obtained using the wave function localized
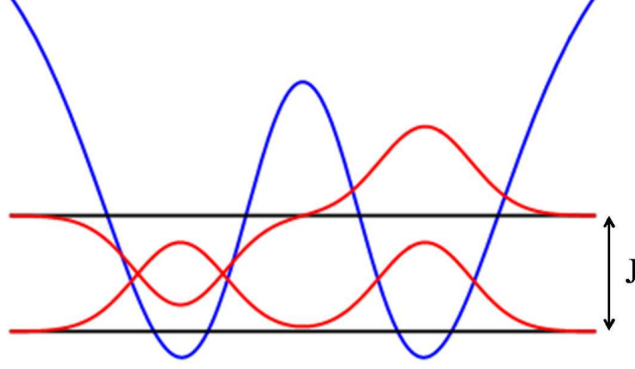

Figure 7.1: Double well potential and its ground state and first excited one. The energy difference between this two levels is the one particle tunneling J.

in the right or left well:

$$\Psi_{r,l} = \frac{1}{\sqrt{2}}(\Psi_g \pm \Psi_e) \tag{7.3}$$

$$\hat{a}_{r,l} = \frac{1}{\sqrt{2}}(\hat{a}_g \pm \hat{a}_e) \tag{7.4}$$

Using the two mode approximation in the localized basis the many body Hamiltonian in Eq. 7.1 assumes the form:

$$\hat{H} = \Delta \hat{J}_z - K \hat{J}_x + U \hat{J}_z^2 \tag{7.5}$$

where $\Delta = E_R - E_L$ is the potential imbalance between the right and left well, $K = -2 \int \Psi_R(x)(-\frac{\hbar^2}{2m}\nabla^2 + V(x))\Psi_L(x)dx$ is called the tunneling term and physically represents the energy gain that the system acquires if an atom hops from one well to the other. Finally $U = g \int |\Psi_{l,r}(x)|^4 dx$ is the interaction energy. The operators in the previous Hamiltonian are obtained as a combination of the creation and annihilation operators:

$$\hat{J}_z = \frac{\hat{a}_L^\dagger \hat{a}_L - \hat{a}_R^\dagger \hat{a}_R}{2} \tag{7.6}$$

$$\hat{J}_x = \frac{\hat{a}_L^\dagger \hat{a}_R + \hat{a}_R^\dagger \hat{a}_L}{2} \tag{7.7}$$

$$\hat{J}_y = \frac{\hat{a}_L^\dagger \hat{a}_R - \hat{a}_R^\dagger \hat{a}_L}{2i} \tag{7.8}$$

this three operators represents the group SU2 (or SO3) since $i[\hat{J}_i, \hat{J}_j] = \varepsilon_{ijk}\hat{J}_k$.

7.1.1.1 Generation of non-classical states - BEC splitter

Several protocols for the generation of non-classical states use the Hamiltonian reported in Eq. 7.5. Such schemes are indeed very simple: it is possible to generate non-classical states such as squeezed stated by splitting a BEC with positive or negative non linearities [112, 113, 114]. Some of them has been also realized experimentally, making use of internal degrees of freedom

of the BEC [115]. For this reason the first sequence that we will consider is provided by the simple splitting of the BEC, that occurs in a time T_1 followed by a waiting time T_2 that can be used to study the robustness of the non-classical state. Since we are interested in the evaluation of the environmental noise that affects such scheme, we will consider a non-interacting system loaded in an harmonic trap and we will study the phase fluctuations after cutting it in two parts with a barrier. As the barrier height increases, the tunneling between the two wells goes to zero. We will consider for simplicity a tunneling $K(t)$ that goes linearly to zero in a time T_1 starting from a value that is equal to the trapping frequency of the initial harmonic trap K, i.e. $K(t) = K_0(1 - t/T_1)$. We finish this sequence by measuring the relative phase between the two clouds letting the system expand and measuring the interference pattern created by the two BECs.

7.1.1.2 Ramsey atom interferometer

Another promising application of a BEC in a double well potential is the realization of a trapped atom interferometer. In this sense a possible scheme is a Ramsey type interferometer. The latter is composed by a beam splitter (BS), followed by an interrogation time T_{int} where the system acquire an interferometric phase and another BS. In the context of trapped atoms, the BS is realized in the following way [97]. We load the BEC in one well of the double well potential. If the tunneling is not negligible the atoms starts to tunnel to the neighboring well. When the population imbalance between the two wells goes to zero, the tunneling is brutally reduce to zero so that he Rabi oscillation is stopped. Now, if the system is influenced by an external force, the phase of the two clouds evolves differently and it can be measured from the population imbalance after a second BS. The phase acquired during equals to $\Delta\Phi = mLaT_{int}/\hbar$ where L is the separation between the two wells, ma the linear external force and T_{int} the interrogation time.

7.1.2 Breaking down of the adiabaticity

Both the sequences described before are characterized by a change in the Hamiltonian. We need to be sure that this modification does not introduce any excitations in the system, i.e. we require that the Hamiltonian changes slowly enougth.

In quantum mechanics an adiabatic process is characterized by a gradual modification in the Hamiltonian of a system from H_i to H_f in such a way that if the system occupies the n-th eigenstate of H_i, it will occupy the n-th eigenstate of H_f. This is known as adiabatic theorem and a demonstration of this results can be found in [116]. If the system is initially in the ground state and we brutally change its Hamiltonian of the system, we easily populate the excited state.

The breaking down of the adiabaticity in a quantum system is associated to the reduction of the energy gap between different states. Consider for instance one of the experimental proceedure under study: the splitting of the BEC. Suppose that at the begin the BEC is in the ground state of the harmonic potential. The Hamiltonian is symmetric at every time against an inversion respect to the barrier, for this reason I will only take in account even eigenfunctions. Solving the Schodinger equation it is possible to study the energy difference between the ground state and the first symmetric excited state. The result is plotted in Fig. 7.2 for a starting tunneling rate $K_0 = 2\pi 150$.

As it is possible to see, the energy gap present a minimum for a given value of the barrier height dE_{min}. By a naively point of view one can expect to break down the adiabaticity of the system ramping up the barrier in a time smaller than $\frac{h}{dE_{min}}$. For the value K_0 chosen we get $T_{adiabaticy} = 5.3$ ms.

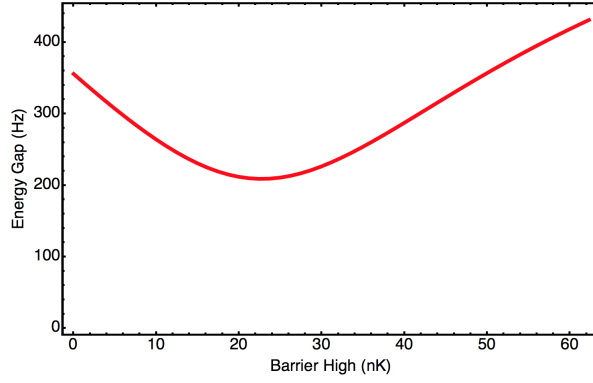To check this value, we perform a numerical simulation. We prepare the system in the ground

Figure 7.2: Energy difference in Hz between the ground state and the first symmetric excited state as a function of the barrier hight in nK.

state of an harmonic trap with trapping frequency given by K_0, then we ramp up the barrier to a residual tunneling of 5Hz. For some sampling time t_s we evaluate the probability of the system to be in the ground state during the splitting time. We report in Fig. 7.3 the results for different rising times of the barrier.

As it is possible to see, the naive explanation given before seems to work: using ramping
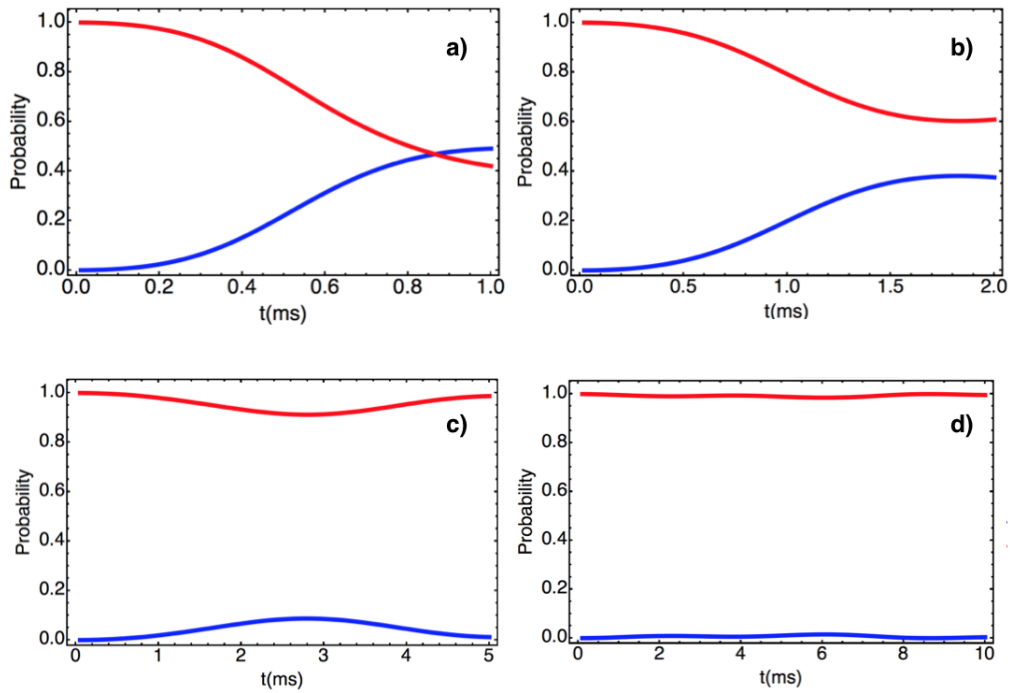
Figure 7.3: Probability of find the state in the ground state, red curve, or in the first excited one, blu curve for a rising time of: a) 1ms b) 2ms c) 5ms and d) 10ms

time larger than $T_{adiabaticy}$ the system remains in the ground state of the system for every time. For shorter time the system get excited: for instance in the case of a ramping time of 1ms we have $\simeq 0.1$ of probability to excite atoms above the first excited states.

This analysis sets a lower bound to the splitting time T_1 that corresponds to 10ms for initial trapping frequency of 150Hz in a double well of spacing 5 μm.

7.2 Sensitivity Function and weight function

In this section we will introduce the so called sensitivity function and we will discuss how it can be use to evaluate the effect of an environmental noise in a general measurement scheme. After that, we will discuss in detail the two sequences introduced before, i.e. the BEC splitter and the Ramsey interferometer.

7.2.1 Power spectral density

A random process $x(t)$ is characterized by several statistical parameter. The most important are the average $\langle x \rangle$ and the variance $\sigma_x^2 = \langle x^2 \rangle - \langle x \rangle^2$ where the average here is performed over all the possible realization of the random variable. If the process is ergodic the ensemble average can be substituted with a temporal one. Supposing that the mean value of $x(t)$ is zero, we can calculate the variance of an ergodic process as

$$\sigma_x^2 = \lim_{T \to \infty} \frac{1}{2T} \int_{-T}^{T} x(t)^2 dt = \lim_{T - \infty} \frac{1}{2T} \int_{-T}^{T} dt \int_{-\infty}^{\infty} F_x(\omega) e^{i\omega t} d\omega \int_{-\infty}^{\infty} F_x(\omega') e^{i\omega' t} d\omega' \quad (7.9)$$

where $F_x(\omega)$ is the Fourier transform of the signal $x(t)$. Exchanging the integration order and using the property of the Dirac's Delta it is possible to demonstrate that

$$\sigma_x^2 = \frac{1}{2} \int_{-\infty}^{\infty} d\omega \frac{1}{T} |F_x(\omega)|^2 \quad (7.10)$$

The power spectral density PSD $S_x(\omega)$ is define as

$$S_x(\omega) = \lim_{T \to \infty} \frac{|F_x(\omega)|^2}{T} \quad (7.11)$$

we can calculate the variance of the random process $x(t)$ using just the positive frequencies, that have physical meaning and can be measured. Using the definition in Eq. 7.11 in Eq. 7.10 we obtain:

$$\sigma_x^2 = \int_{0}^{\infty} S_x(\omega) d\omega \quad (7.12)$$

The previous calculation represents an ideal situation: in a more realistic case the average of an observable can be measured in a finite time. How this fact modifies the previous relation? A k-sim realization of the random process $x(t)$ is defined as the measure of $x(t)$ from a beginning time t_k for a time τ_k. In this case we can define a new random process $y(t)$ satisfying:

$$y(t) = \int_{-\infty}^{\infty} dt' h(t_k - t') x(t') \quad (7.13)$$

where $h(t' - t_k) = 1$ if $t_k \leq t' \leq t_k + \tau_k$ and 0 otherwise. This new random process has by definition the same statistical proprieties of $x(t)$ but is defined in an infinity time domain, so we can use the result obtained before.

$$\sigma_{x,k}^2 = \sigma_y^2 = \int_{0}^{\infty} d\omega S_y(\omega) \quad (7.14)$$

The PSD of the random process $y(t_k - t)$ can be written as a function of the PSD of $x(t)$ using the convolution theorem. In fact $y(t)$ is nothing else the convolution of $x(t)$ with $h(t_k - t)$ so $F_y(\omega)$ is the product of $F_x(\omega)$ and $F_h(\omega)$, we get finally

$$\sigma_{x,k}^2 = \int_{0}^{\infty} d\omega S_x(\omega) H(\omega) \quad (7.15)$$

where $H(\omega) = |F_h(\omega)|^2$ is called transfer function. This function takes in account of the finite duration of the measurement. In a more suitable way, as we will see, it can contain information about the sensitivity of an instrument.

7.2.2 Sensitivity Function

The sensitivity function $g(t)$ has been used for example to estimate the sensitivity of a fre falling Mach-Zehnder atom interferometer [117]. The interferometric phase is measured from the phase or in general from an observable η. Suppose that during the interferometric sequence a perturbation occurs at time t. We will consider a perturbation provided by a kick $\phi \hat{J}_z$ that physically represents the effect of some kind of noise creating a potential imbalance between the two wells $\delta(t)$. These two random variable are related by $d\phi(t) = \delta(t)dt/\hbar$ The variable ϕ related to the noise affecting the system, has not to be confused with the phase Φ that is the quantity that is measured by the interferometer. If the unperturbed sequence gives as result η_0, the effect of the noise kick is to modifies it to $\eta(t)$. We can define the sensitivity function $g(t)$ as:

$$g_\eta(t) = \lim_{\phi \to 0} \frac{\eta(t) - \eta_0}{\phi} \tag{7.16}$$

It follows from the definition of sensitivity function that:

$$\delta\eta = \int_{-\infty}^{\infty} g_\eta(t)d\phi(t) \tag{7.17}$$

and thus

$$\delta\eta = \int_{-\infty}^{\infty} g(t)\delta(t)dt \tag{7.18}$$

Expression in Eq. 7.18 is similar to the one in Eq. 7.13 where the function $h(t - t_k)$ is replaced by $g(t)$. For this reason we can use the results obtained before to get the variance of the measured quantity η:

$$\sigma_\eta^2 = \int_0^\infty d\omega S_\delta(\omega)G(\omega)d\omega \tag{7.19}$$

where $G(\omega) = |F_g(\omega)|^2$ is called the weight function related to the variable η. Note that in the BEC splitter and in the Ramsey interferometer the observables η we are involved in the measurements are the phase Φ and the population imbalance z rispectly.
By an experimental point of view, is difficult to access to the random variable $\delta(t)$. Several physical effects create a potential imbalance in a double well potential ranging from the vibrational motion of the reflecting mirrors to the frequency fluctuations of the laser sources. For almost every noise source is possible to measure the PSD and to determinate how it affects the stability of the double well potential.

7.2.3 Sensitivity function of a BEC splitter

We will now discuss the first measure scheme considered. Tunneling as function of time is given by:

$$K(t) = \begin{cases} K_0(1 - \frac{t}{T_1}) & 0 \le t \le T_1 \\ 0 & T_1 \le t \le T_1 + T_2 \end{cases} \tag{7.20}$$

The initial state vector is represented by (1,0,0) in the Bloch sphere since both the initial phase and imbalance are null. We will start considering the time during which the barrier is raised up. The evolution is basically divided in three parts: during the first, that goes from $t = 0$ to $t = t^*$ when the perturbation occurs, the Hamiltonian is just provided by the tunneling term. Since the starting state vector is an eigenstate of the Hamiltonian there is no temporal evolution. In the second part $t^* \le t \le t^* + dt$, during which the perturbation occurs, both J_x and J_z determine the dynamics of the system; in the last part from t^* to the end of the sequence, again the Hamiltonian is again proportional to J_x. If the duration of the perturbation dt is infinitesimal, we can neglect the commutator between the different

terms in the Hamiltonian that scale as dt^2 and we can evaluate the state at the end of the sequence as:

$$|\psi_{final}\rangle = \begin{pmatrix} 1 & 0 & 0 \\ 0 & cos(\theta_2) & sin(\theta_2) \\ 0 & -sin(\theta_2) & cos(\theta_2) \end{pmatrix} \begin{pmatrix} cos(\phi) & -sin(\phi) & 0 \\ sin(\phi) & cos(\phi) & 0 \\ 0 & 0 & 1 \end{pmatrix} \begin{pmatrix} 1 & 0 & 0 \\ 0 & cos(\theta_1) & sin(\theta_1) \\ 0 & -sin(\theta_1) & cos(\theta_1) \end{pmatrix} \begin{pmatrix} 1 \\ 0 \\ 0 \end{pmatrix}$$
(7.21)

where $\theta_1 = 2\int_0^{t^*} dtk(t)$ and $\theta_2 = 2\int_{t^*}^T dtk(t)$. With a little of algebra:

$$|\psi_{final}\rangle = \begin{pmatrix} cos(\phi) \\ cos(\theta_2)sen(\phi) \\ sin(\phi)sin(\theta_2) \end{pmatrix}$$
(7.22)

At the end of the sequence we can measure the phase difference between the two clouds. For this reason according to the definition of the sensitivity function in Eq. 7.16, we get:

$$g_\Phi = Cos(\theta_2) = Cos(2\int_t^T k(t')dt')$$
(7.23)

Note that the sensitivity function fo the BEC splitter depends only on the time after the perturbation. This is caused by the fact that before the perturbation occurs, the system is in an eigenstate of the Hamiltonian.

The second part of the interferometric sequence is simpler: if the tunneling is 0 any perturbation of the imbalance between the two wells has dramatic consequence on a phase measurement and by definition $g_\Phi = 1$ for $T_1 \leq t \leq T_1 + T2$.

The sensitivity function of the phase $g_\Phi(t)$ and of the population imbalance $g_z(t)$ with the tunneling introduced in Eq. 7.20, are reported in Fig. 7.4 below for $T_1 = T_2 = 100$ ms.

To estimate the standard deviation of a phase measurement after the splitting, we have
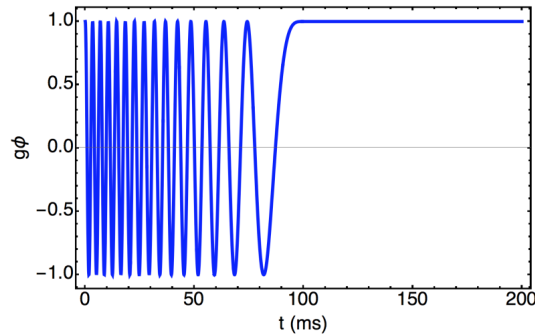

Figure 7.4: Sensitivity function for a phase measurement in a BEC splitting sequence. The curve is evaluated for $T_1 = T_2 = 100$ms.

introduced in Section 2.2 the weight function $G_\Phi(f)$ defined as the Fourier transform of the sensitivity function $g_\Phi(t)$ (see Eq. 7.19). For the case under study, is possible to evaluate analytically $G_\Phi(t)$. An example of a weight function is reported in Fig. 7.5. As it is possible to see, the behavior of the splitting scheme acts as a low pass filter with a cut-off frequency of the order of $K_0/2\pi$. For frequencies smaller than the cut-off the weight function is a plateau. It is possible to demonstrate that its value depends on $(T_1 - T_2)^2$ plus an offset that depends only on T_1. To minimize the low frequency component of a given PSD, if it is possible, the suitable choice is to take an observation time T_2 equal to the beam splitter duration T_1. In the high frequencies limit, the cut off acts as $|G_\Phi|^2 \propto 1/f^2$.
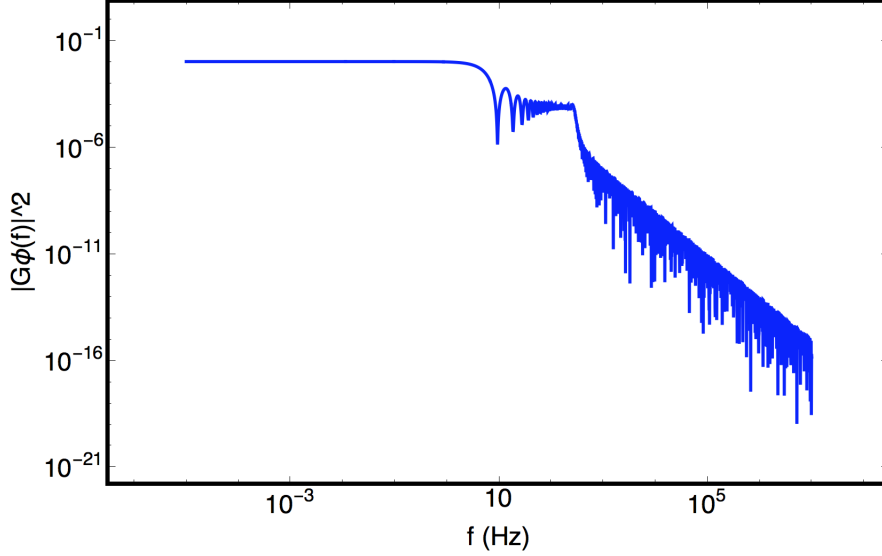
Figure 7.5: Weight function $G_\Phi(f)$ for $T_1 = T_2 = 100\text{ms}$ and a starting tunneling $K_0 = 2\pi 150\text{Hz}$.

7.2.4 Sensitivity function for Ramsey interferometer

Now we will calculate the sensitivity function for the Ramsey sequence introduced in Section 1. According to the Bloch picture, the BS is represented by a rotation of $\pi/2$ along the x direction. The phase acquisition is instead represented by a rotation of $\Delta\Phi$ along the vertical axes. The final state is then given by:

$$|\psi_{final}\rangle = \begin{pmatrix} 1 & 0 & 0 \\ 0 & 0 & 1 \\ 0 & -1 & 0 \end{pmatrix} \begin{pmatrix} cos(\Delta\Phi) & -sin(\Delta\Phi) & 0 \\ sin(\Delta\Phi) & cos(\Delta\Phi) & 0 \\ 0 & 0 & 1 \end{pmatrix} \begin{pmatrix} 1 & 0 & 0 \\ 0 & 0 & 1 \\ 0 & -1 & 0 \end{pmatrix} \begin{pmatrix} 1 \\ 0 \\ 0 \end{pmatrix} = \begin{pmatrix} sin(\Delta\Phi) \\ 0 \\ cos(\Delta\Phi) \end{pmatrix}$$
(7.24)

As before in order to calculate the sensitivity function we need to evaluate the effect of a perturbation provided by a rotation ϕ along the z direction that occurs at a time t. Without reporting all the calculations it is possible to prove that the sensitivity function of a Ramsey sequence is given by:

$$g_Z(t) = \begin{cases} Sin(2\int_0^t K(t')dt') & 0 \leq t \leq T_1 \\ 1 & T_1 \leq t \leq T_2 \\ Cos(2\int_{T_2}^t K(t')dt') & T_2 \leq t \leq T_3 \end{cases}$$
(7.25)

and zero otherwise where T_1 is the duration of the BS, $T_2 = T_1 + T_{int}$ and $T_3 = T_{int} + 2T_1$. Similar expression has been found in [118]. We can calculate the weight function $G_z(f)$ from the expression reported in Eq. 7.25, obtaining [117]:

$$G_z(f) = \frac{4i\Omega_R}{(2\pi f)^2 - \Omega_R^2} sin(\pi f(T_{int} + 2T_1))\big(cos(\pi f(T_{int} + 2T_1)) + \frac{\Omega_R}{2\pi f}sin(\pi f T_{int})\big) \quad (7.26)$$

This last expression in valid if the tunneling $K(t) = K_0 = \Omega_R = \pi/(2T_1)$ is constant during the BS.

Indeed we have generalized the results reported there for any time function describing the tunneling between the two wells. In the free falling interferometer the tunneling is constant and it is provided by the Raman beams, for this reason the time during which the tunneling pass from a finite value to zero is negligible because depends on the switching on-off time of

a laser beams. Instead in a trapped atom interferometry this time could be much larger and even comparable to the interrogation time.

We can try to understand the effect of the finite ramp time considering this simple case. Suppose to have a tunneling that start from a finite value, of $2\pi 20$Hz, and goes linearly to zero $K(t) = K_0(1 - t/T_{BS})$. In order to provide a correct BS the duration of the ramp is fixed: $T_{BS} = \pi/(2K0)$. We can compare the sensitivity function obtained whit this tunneling with an "ideal" one provided by a step-function tunneling. The results for the sensitivity function are reported in Fig. 7.6, as it is possible to see no substance differences are observed between the two functions.

Evaluating the weight function G_z for both the sensitivity function considered, we obtain similar results. In both cases the system starts to filter noise for frequency larger then K_0. In the high frequency limit $|G(g)|^2 \propto f^{-4}$ differently from the case of the BEC splitting. Additionally in the limit of small frequencies $G_z \propto f$. The weight function of a Ramsey scheme is thus similar to a band-pass filter. Some weight functions are reported in Fig. 7.13.

Another very useful scheme used in fre fallinging atom interferometers, is the Mach-Zehnder
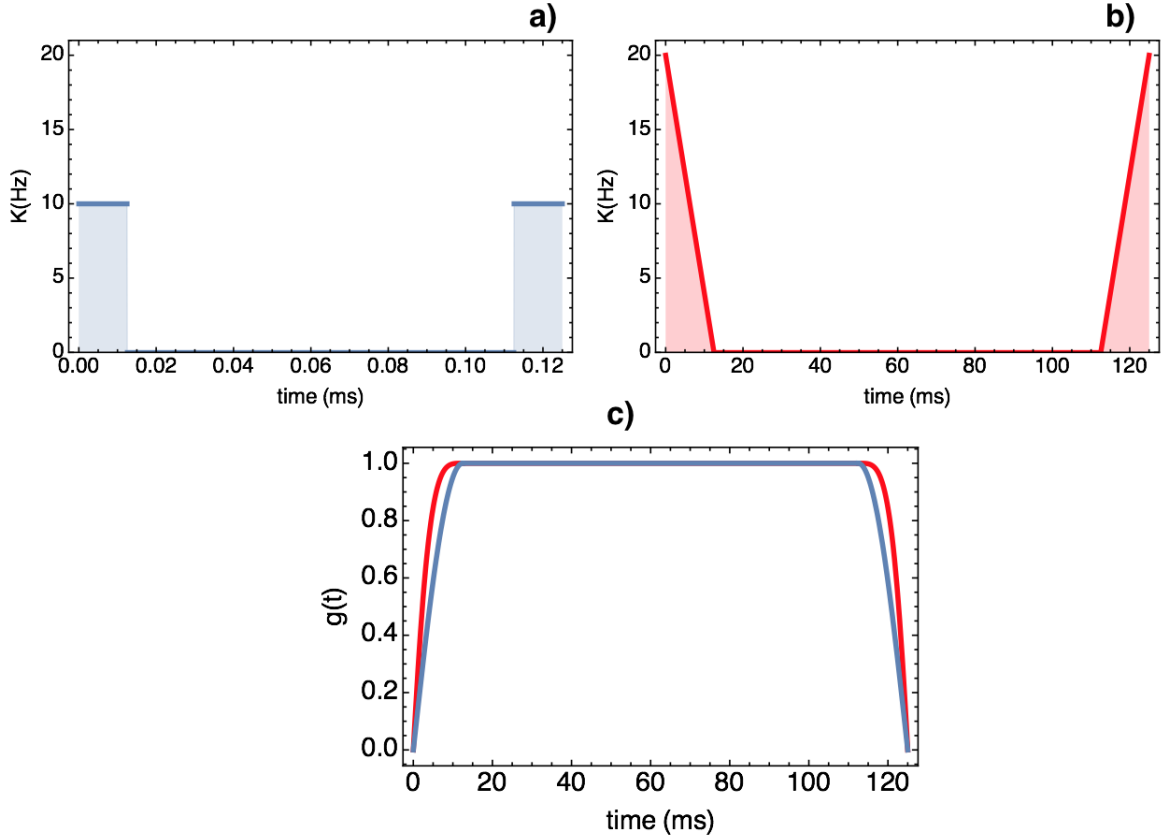

Figure 7.6: a,b) tunneling function as described in the text, c) sensitivity function evaluated with both of them.

interferometer. This works essentially as two Ramsey scheme performed consequentially, i.e. it is composed of a $\pi/2$ - π -$\pi/2$ pulses divided by two interrogation times T_{int}. In this case

the sensitivity function is given by:

$$g_Z(t) = \begin{cases} Sin(2\int_0^t K(t')dt') & 0 \le t \le T_1 \\ 1 & T_1 \le t \le T_2 \\ Cos(2\int_{T_2}^t K(t')dt') & T_2 \le t \le T_3 \\ -1 & T_3 \le t \le T_4 \\ -Sin(2\int_0^t K(t')dt') & T_4 \le t \le T_5 \end{cases} \quad (7.27)$$

and zero otherwise where T_1 is again the duration of the BS, $T_2 = T_1 + T_{int}$, $T_3 = T_{int} + 3T_1$, $T_4 = 2T_{int} + 3T_1$ and $T_5 = 2T_{int} + 4T_1$.

The expression obtained is exactly the same as in [117, 119] in here extended for a general temporal dependence of the coupling between the two modes during the BS. Note that weight function $G_z(f)$ is the same for the both Ramsey and Mach-Zehender interferometers.

7.3 Noise sources

In this section we will estimate the effect of some noise sources on the BEC splitting process described in the Section 1, using the weight function obtained in Section 2.3. We will consider two superimposed retro-reflected laser beam with wavelength 10 and 20 μm creating an array of double wells potential separated by 10μm where the wells are separated by 5μm. Although the realizability of such lattices with large spacing seems unrealistic, new ideas on the creation of effective large spacing optical lattices are under investigation.

The two main noise sources that we will consider are provided by the vibration of the reflecting mirror and by the lasers frequencies fluctuation.

7.3.1 Vibrational noise

In our case the motion of the mirror shifts the lattice position. Even if this effect does not modify the shape of the potential, it creates an effective phase shift $d\phi$ between the two modes of the interferometer. Indeed this phase shift is proportional to the acceleration of the mirror $a(t)$:

$$d\phi(t) = \frac{ma(t)Ldt}{\hbar} \quad (7.28)$$

Where L is the distance between the two wells of the double well potential.

Using Eq. 7.28 in the definition of sensitivity function reported in Eq. 7.18, we get:

$$\delta\Phi = \int_{-\infty}^{\infty} g_\phi(t)\frac{d\phi(t)}{dt}dt = \int_{-\infty}^{\infty} g(t)_\phi\frac{mLa(t)}{\hbar}dt \quad (7.29)$$

Where $g_\phi(t)$ is the sensitivity function of the BEC splitter derived in Section 2.2. We can estimate the vibration effect considering Eq. 7.29 in the frequency domain, i.e. :

$$\sigma_\Phi^2 = \int_0^\infty |G_\Phi(f)|^2 S_\phi(f)df = 2\pi \int_0^\infty (\frac{mL}{\hbar})^2 |G_\Phi(f)|^2 S_a(f)df \quad (7.30)$$

The PSDs we use to estimate the standard deviation in the measure of the relative phase after the splitting are reported in Fig. 7.7. The red curve has been measured in our lab while the blue one in Syrte Laboratory in the group of Dr. Franc Pereira Dos Santos. The vibrational noise in the second case is passively reduced. Using these PSDs, we get the standard deviation as a function of the waiting time T_2 reported in Fig. 7.8, for different values of T_1.

The most relevant part of the spectral noise is the one at low frequency since in that region the weight function does not filter any components. To better understand what is the
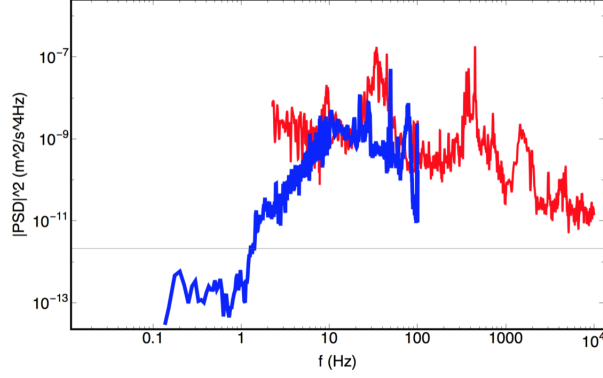
Figure 7.7: Typical PSD of vibrational noise, we use two spectra for the estimation of this noise
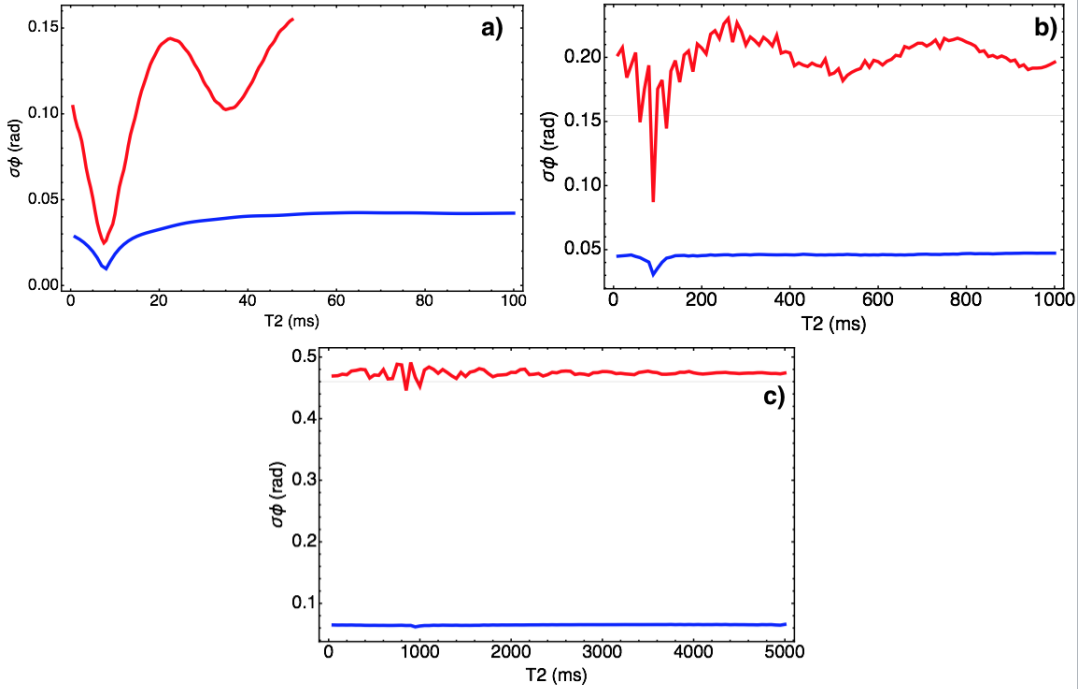

Figure 7.8: Standard deviation of a phase measurement as a function of the interrogation time T_2 for different values of T_1: a) 10ms, b) 100ms and c)1000 ms.

frequency range that mostly affects the sensitivity of system, we can consider the integral function $\sigma_\Phi(f)$ defined as:

$$\sigma_\Phi(f) = \sqrt{2\pi \int_0^f df'(\frac{mL}{\hbar})^2 G_\Phi(f) S_a(f) df'} \tag{7.31}$$

the results for the two PSD considered are reported in Fig. 7.9. As it is possible to see, the most important components of a vibrational noise are the one between 10 and 100 Hz.

To reduce the effect of the vibrational noise in an interferometric measurement, several solutions are available. In a fre falling atomic interferometer methods for reduce actively vibrational noise has been developed [120]. We are planning to install in our setup, an isolating platform from $Minus - K$ that is able to reduce passively the vibrational noise for frequencies larger than about 1Hz. For the dimensions of the platform, the possible
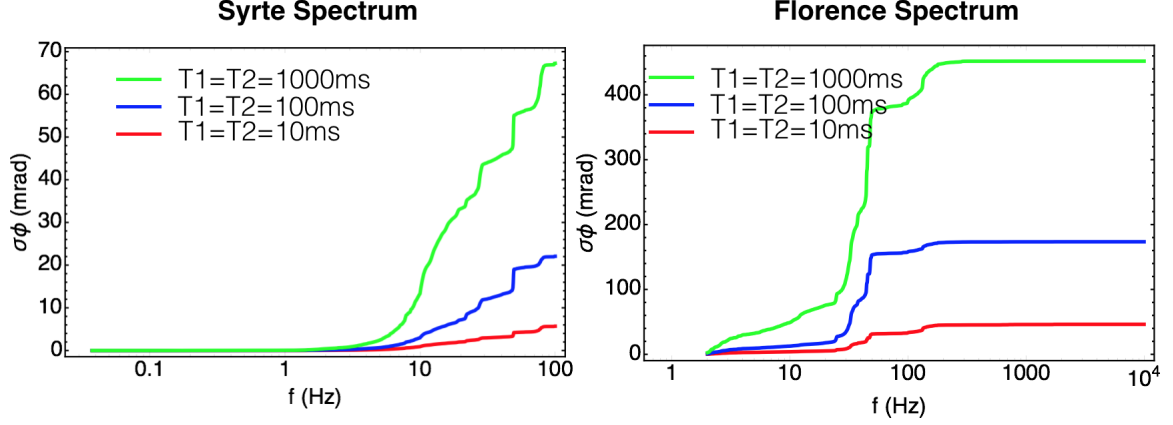
Figure 7.9: Plot of the integral function $\sigma_\Phi(f)$ for the two PSD considered. Every plot contains the results for $T_1 = 10, 100, 1000$ ms

candidates that can be easily installed in our experiment are the models LC-4 and BM-10. The model LC-4 seems to have better performances for both horizontal and vertical plane because the peak frequency is at 0.5Hz while for BM-10 is at 1.5Hz.

To have an estimation of the platform effect in our setup I convolve the noise measured with the transmissibility curve of the desired platform. It is possible to get an analytic expression of the transmissibility from the physics of the dumped harmonic oscillator. The equation of motion of this system is given by:

$$m\frac{d^2x}{dt^2} = -kx + c\frac{dx}{dt} + F_{ext}(t) \tag{7.32}$$

This equation can be solved for any external forces $F_{ext}(t)$. The dynamics of the system is governed by just one a-dimensional parameter, the so called damping ratio:

$$\zeta = \frac{c}{2\sqrt{mk}} \tag{7.33}$$

If $\zeta > 1$ the motion is called over-damped and the system returns to the steady state without oscillating; if $\zeta = 1$, the motion is called critically dumped and the system return to the steady state without oscillation in the fastest way; $\zeta < 1$ is the under dumped case and the system oscillate with an amplitude that gradually decay to zero. According to the producers, a $Minus - K$ platform acts as an under-dumped oscillator with a damping ration between $\zeta = 0.05$ and $\zeta = 0.1$ and a characteristic frequency $f_0 \simeq 0.5$Hz ($f_0 = \sqrt{k/m}$). Suppose now that the external force is provided by an harmonic oscillator with a frequency $\omega = 2\pi f$. In our case it represents an external vibrational noise at a given frequency, i.e. $F_{ext} = ma_0 e^{i\omega t}$. Using Eq. 7.32 and the definition of damping ratio, we get that:

$$\frac{dx^2}{d^2t} + 4\pi f_0 \zeta \frac{dx}{dt} + (\omega_0)^2 x = a_0 e^{i\omega t} \tag{7.34}$$

Assuming a solution that oscillates at the same frequency of the perturbation $x(t) = Ae^{i\omega t + \psi}$ and substituting it in the equation of motion it is possible to prove that

$$\begin{cases} \omega A\zeta\omega_0 = a_0 \sin(\psi) \\ A(\omega_0^2 - \omega^2) = a_0 \cos(\psi) \end{cases} \tag{7.35}$$

combining the two previous equations it is possible to get how the amplitude of the external force is dumped by the platform:

$$A = \frac{a_0}{\sqrt{(\omega\omega_0\zeta)^2 + (\omega^2 - \omega_0^2)^2}} \tag{7.36}$$

Since the amplitude of the external acceleration is given by $\omega^2 A$, we define the transmissibility $T(f)$ as:

$$T = \frac{A}{a_0} = \frac{1}{\sqrt{(\frac{\omega_0}{\omega}\zeta)^2 + (\frac{\omega^2 - \omega_0^2}{\omega^2})^2}} \tag{7.37}$$

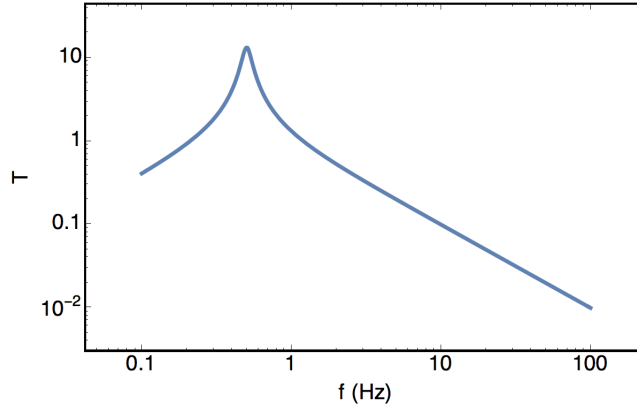the theoretical transmissibility for a $Minus - K$ platform is reported in Fig. 7.10. In order

Figure 7.10: Theoretical transmissibility of a dumped harmonic oscillator with $f_0 = 0.5$ and a dumping constant $\zeta = 0.075$

to evaluate the improvement in the sensitivity provided by the use of a passive $Minus - K$ platform, we have convolved the PSD measured with the transmissibility function reported in Fig. 7.10. Convolving the noise measured in our system with the transmissibility of a $Minus - K$ platform and using this new PSD for evaluate the standard deviation of a phase measure, we get the results reported in Fig. 7.11. As it is possible to see the standard deviation is smaller of a factor $\simeq 10$ respect to the one in Fig. 7.7. This is due to the fact that the most important components in the evaluation of the standard deviation was the frequencies between 10 and 100Hz, this components are well dumped by a $Minus - K$ platform. To better understand the effect of this platform, will be necessary in the future measuring the vibrational noise PSD for frequencies smaller than 2Hz: the peak of the transmissibility at 0.5Hz could have an important effect.

7.3.2 Frequency noise

The second noise source comes from frequency fluctuation of the lattice lasers. Since the effective large spacing optical lattice we are planning to realize, use frequency around 1064nm, we will consider as PSD of the frequency fluctuation the one provided by the specification of a Mephisto laser from Coherent. The PSD can be approximated as $S_{\Delta\nu} = \frac{10^4}{f} Hz/\sqrt{Hz}$. This behavior is indeed verified up to 10KHz, while for frequency higher that this the frequency PSD assumes a constant value a part from the appearance of some pecks corresponding to the piezoelectric resonances that are present up to $500 - 600$ KHz. For even larger frequencies the frequency PSD is filtered by the laser cavity resonance and can be considered negligible. The effect of a frequency shift $\delta\nu$ is to displace the interference pattern by:

$$\Delta x = \Delta L \frac{\delta\nu}{\nu} \tag{7.38}$$

where ΔL is the difference in the optical path of the two interfering laser beams, in our case this is of the order of 20 cm. As explained in a previous case, an atom interferometer that uses trapped atoms is sensible to the acceleration of the interference pattern and not
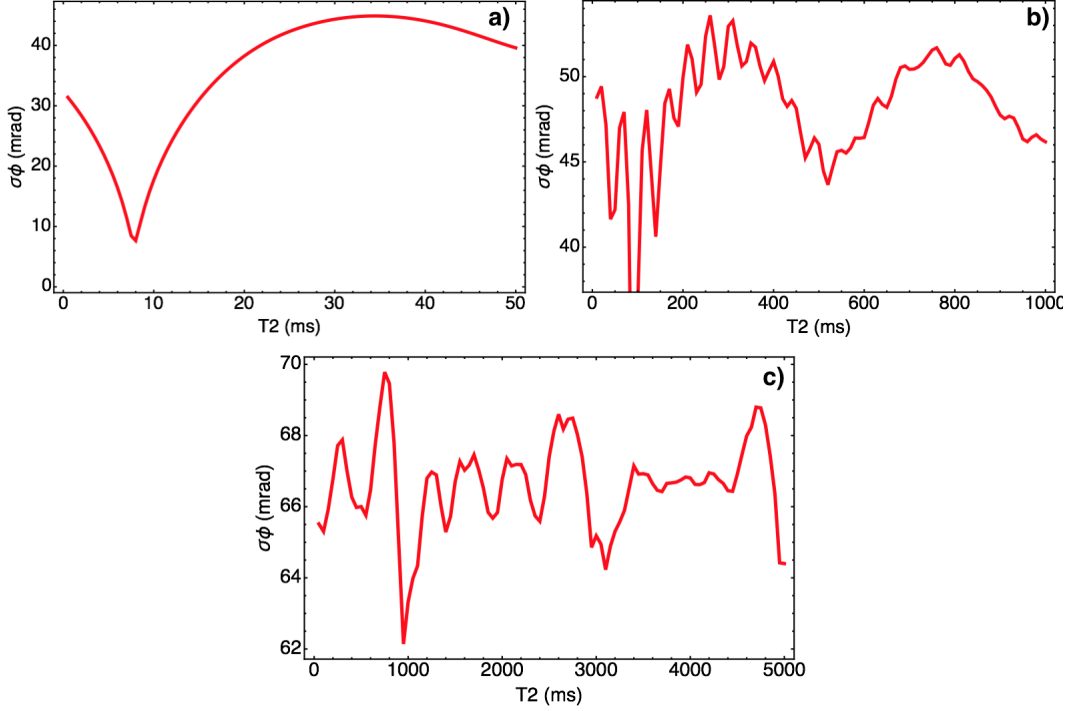
Figure 7.11: Standard deviation of a phase measurement as a function of T_2 for different splitting time T_1. The PSD considered in this section has been convolved with the theoretical transmissibility of a dumped harmonic oscillator with $f_0 = 0.5$ and a dumping constant $\zeta = 0.075$. This is a representation of the effect of a $Minus - K$ platform model LC-4.

to the displacement. For this reason we can use the results in Eq. 7.29 and its version in the frequency domain Eq. 7.30 simply substituting to the acceleration the random variable $\Delta L \frac{\delta \nu''}{\nu}$.

The PSD of the random variable $\Delta \nu''(t)$ is related to the one of $\Delta \nu(t)$ by:

$$S_{\Delta \nu''}(\omega) = \omega^4 S_{\Delta \nu}(\omega) \tag{7.39}$$

this expression could be easily obtained using the definition of PSD in Eq. 7.11, introduced in the first paragraph, and some simple properties of the Fourier transform.

Using now the PSD of the frequency noise provided by the Coherent and the weight function $G_\Phi(f)$ for our BEC splitter evaluated as in Section 2.2, is possible to calculate the standard deviation of a phase measurement associated to this noise source. The term ω^4 that appear in the evaluation of $S_{\Delta \nu''}$ has a crucial effect: for its presence $S_{\Delta \nu''} \propto f^2$. This dependence reduces a lot the contribution of the low frequency components but increases the role of higher part of the noise spectrum because this components are not filtered by the weight function. For frequency larger than $K0$, indeed, $G_\Phi(f) \propto \frac{1}{f^2}$, i.e. the integrand does not depend on the frequency so the integral is proportional to f. The integral extended to ∞ diverges but for physical reason I have evaluated the integral for the standard deviation up to a frequency $f_{max} = 1 \text{GHz}$, for larger frequency the frequency PSD is expected to be negligible.

Despite from this, evaluating the quantity:

$$\sigma_\Phi = \frac{mL \Delta L (2\pi)}{\hbar \nu} \sqrt{\int_0^{f_{max}} f^4 S_\nu(f) |G_\Phi(f)|^2 df} \tag{7.40}$$

it is possible to observe that the standard deviation is of the order of 10^{-4} rad. Results for three different splitting time T_1 are reported in Fig. 7.12.
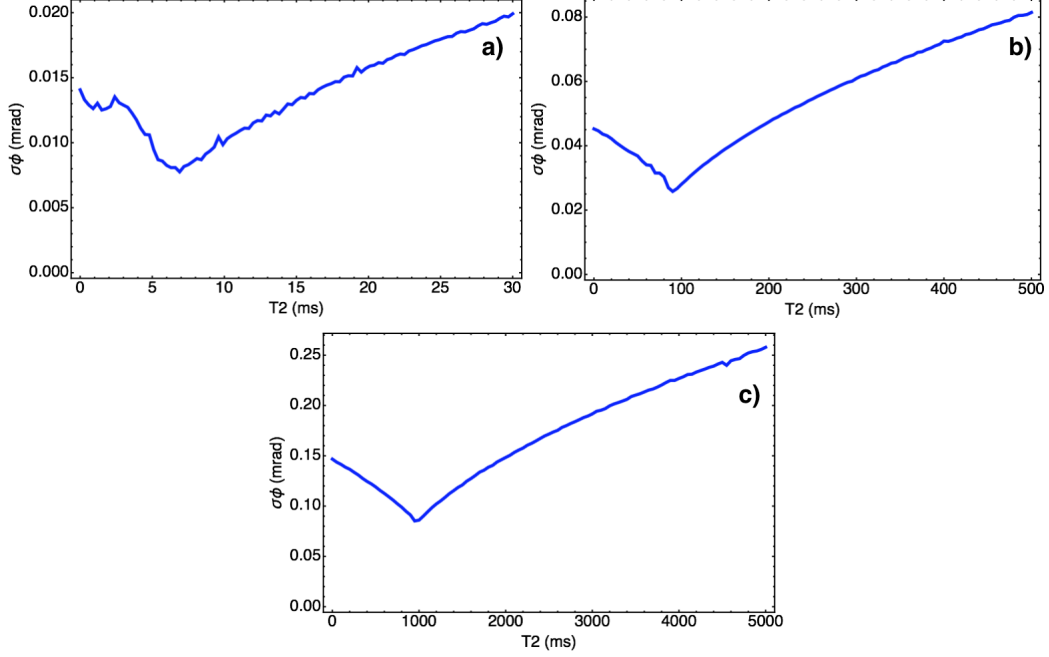
Figure 7.12: Standard deviation for a phase measurement taking in account the free fluctuation of the Mephisto frequency . The standard deviation is evaluated as a function of the interrogation time T_2. The three plots represent three different splitting time T_1: a) 10ms, b) 100 ms and c) 1000ms.

The effect of the frequency noise seems to be negligible compared to the one caused by vibrations. However for future upgrade of our experimental setup, we will have to work with lasers with performances comparable to the Mephisto laser, which is a metrological laser.

7.4 Comparison with free-fall interferometers

In this section we will use the second scheme considered in Section 1, i.e. a Ramsey interferometer. Our aim is to compare the performance of an atom interferometer that use trapped atom with the scheme with a standard fre fallinging atom interferometer. Typically the latter uses a Mach-Zehender scheme, despite from this, as reported in Section 2, Ramsey and Mach-Zehender posses the same weight function $G_z(f)$ so we can directly compare the two schemes. Having in mind the results concerning the BEC splitter discussed in Section 3, we will concentrate our analysis to the vibrational noise which seems to be the largest noise source.

The main differences between the two interferometers are provided by the time scales of the BS and the interrogation time T_{int}. Indeed the Rabi frequency in the case of free-fall interferometers is of the order of some tens of KHz and can not be reduced because of the temperature of the sample [119]. In the case of trapped atom interferometer instead it is of the order of tens of Hz, this means that the low-pass filter behavior of the weight function starts for smaller frequencies in this second case.

In addition in the trapped atom interferometer the tunneling during the BS is not brutally reduce to zero but using an adiabatic ramp. Actually, as reported in Fig. 7.6, the different tunneling as a function of time seems to introduce negligible effect. For simplicity we thus consider as weight function for both the interferometers the one reported in Eq. 7.26.

The other difference is that the two techniques are sensitive to different physical quantity. In the case of vibrational noise, the free-fall interferometers is affected by the velocity of the

mirror while the trapped atom interferometer to its acceleration. Indeed it is possible to prove in the case of the free-fall interferometer that [117]:

$$\delta\Phi = \int_\infty^\infty g_z(t)k_{eff}\frac{dz(t)}{dt}dt \tag{7.41}$$

Where z is the mirror position and k_{eff} is the effective wavenumber of the Raman beams, in the case of counter-propagating beams $k_{eff} = 2k_{laser}$. Equivalently in the Fourier domain we get:

$$\sigma_\Phi^{frefalling} = \sqrt{\int_0^\infty |G_z(f)|^2 k_{eff}\frac{S_{z''}(f)}{f^2}df} \tag{7.42}$$

where we use the relation between velocity and acceleration PSDs $S_{z'} = S_{z''}/f^2$. We will consider for this comparison, typical performances of both the interferometers: for the free-fall $T_{int} = 150$ms and a BS duration of 100μs; for the trapped one instead $T_{int} = 100$ms and a Rabi frequency of 20Hz. We report the two weight function G_z evaluated according to Eq. 7.26 in Fig. 7.13. As it is possible to see, the two weight finctions are essentially the same for small frequencies, instead at large frequencies, the low-pass filter behavior starts before in the trapped atom interferometer.

To better understand the different effect that the vibrational noise introduces on the two
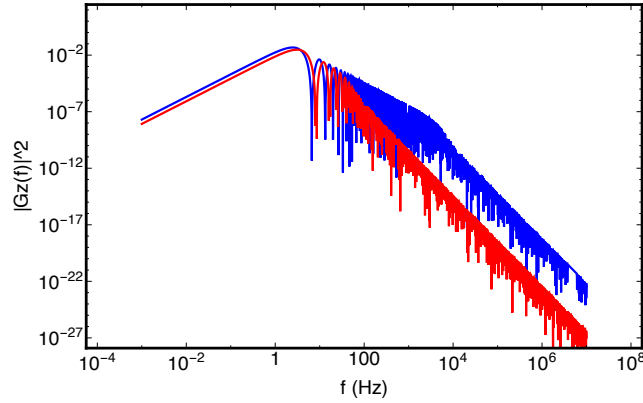

Figure 7.13: G_z for a typical performances of a free-fall atom interferometer (Blue curve) and for a trapped atom interferometer (Red curve).

interferometric techniques, we can consider the signal to noise ratio. For simplicity we will consider a measurement of the gravity g. In the case of a free-fall atom interferometer the phase acquired in this measurement is given by $\Phi_{FF} = k_{eff}gT_{int}^2$. The phase acquired by a trapped atom interferometer is instead given by $\Phi_{trap} = \frac{mLg}{\hbar}T_{int}$. For the free-fall interferometers, using Eq. 7.42, we get for the signal-to-noise ratio:

$$\frac{\Delta g}{g} = \frac{\Delta\Phi}{\Phi} = \sqrt{\int_0^\infty df|G_z(f)|^2 k_{eff}\frac{S_{z''}(f)}{f^2}\frac{1}{k_{eff}T_{int}^4 g^2}} = \sqrt{\int_0^\infty df S_{z''}(f)\chi_{FF}(f)} \tag{7.43}$$

where

$$\chi_{FF}(f) = |G_z(f)|^2\frac{1}{k_{eff}g^2 T_{int}^4 f^2} \tag{7.44}$$

In the case of trapped atom interferometer instead using Eq. 7.30, in the case of a Ramsey interferometric scheme and thus substituting G_z to G_Φ, we get:

$$\frac{\Delta g}{g} = \frac{\Delta\Phi}{\Phi} = \sqrt{\int_0^\infty df|G_z(f)|^2\frac{S_{z''}(f)}{g^2 T_{int}^2}} = \sqrt{\int_0^\infty df S_{z''}(f)\chi_{trap}(f)} \tag{7.45}$$

where

$$\chi_{trap}(f) = |G_z(f)|^2 \frac{1}{T_{int}^2 g^2} \tag{7.46}$$

The two χ functions have the physical meaning of an effective weight function. Indeed we can just convolve them with a certain acceleration PSD to get the expected signal-to-noise ratio. We report bothχ_{FF} and χ_{trap} for the specific case considered in Fig. 7.14. As it possible to see, the f^2 that is present in the definition of χ_{FF} make the free-fall interferometer much sensitive to the noise component at very small frequencies. Contrary the trapped scheme seems to be more affected by the part of the spectrum around 10Hz, close to the Rabi frequency.

Using the acceleration PSD provided by the Syrte group, we get that the signal-to-noise ratio $\Delta g/g = 0.7 \ 10^{-6}$ for the fre falling interferometer while for the trapped one is almost 10 time larger, $5 \ 10^{-6}$. Note that this is due to the fact that the signal in the fre falling case is more then 1000 times larger then in the trapped atom interferometer. Indeed the standard deviation is much smaller in this second case.
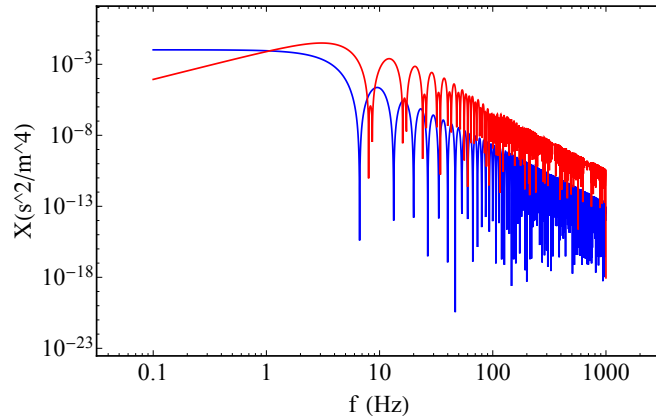

Figure 7.14: $\chi(f)$ for a typical performances of a free-fall atom interferometer (Blue curve) and for a trapped atom interferometer (Red curve).

7.5 Conclusion

In conclusion in this Chapter we have introduce a mathematical formalism that is able to recover the sensitivity function for different experimental schemes. In particular we are interested in the cases of the splitting of a BEC, which could be use for the generation of non-classical states, and of a trapped atom interferometer that makes use of a Ramsey scheme.

We then apply such functions to some realistic PSDs of two different noise source: the vibration noise of a retro-reflecting mirror and the frequency fluctuation of the laser sources. We discover that we are mainly limited by the first effect even if it can be reduce a lot using a anti-vibration platform.

Finally we compare the performance of an atom interferometer that use a free-fall Mach-Zhender scheme with a trapped atom interferometer. We found that the two sequences are mainly affected by different frequency-regions of the PSDs: the free-fall is indeed limited by the low frequencies component, smaller then 1Hz. Instead the trapped atom interferometer by the components in the region 10-20Hz.

Appendix A

Three-Body losses

In this appendix I will shortly describe the measurements performed in order to characterize the three-body recombination rate in all different channels involved in the Bose-Bose mixture we are using.

Three-body recombination is the process where two atoms form a compound while interacting with a third atom. This process is the main cause of atom losses in ultracold samples. It is possible to prove that [121]:

$$\frac{dN}{dt} = -K_3 < n^2 > N \tag{A.1}$$

In presence of three-body recombination the temperature increase is due to the preferential removal of atoms in the high-density region around the trap center:

$$\frac{dT}{dt} = \frac{K_3}{3} < n^2 > T \tag{A.2}$$

where $< n^2 >= 1/N \int n(r)^3 d^3r$ is the mean square density that depends on the system under study.

A.1   Three-Body losses in a thermal gas

The simplest case is a thermal gas in an harmonic trap. In this case it's possible to calculate the mean square density and solve the previously introduced coupled differential equations [122]. The solutions are the following:

$$N(t) = \frac{N_0}{(1 + \frac{3\beta^2 N_0^2}{T_0^3 \sqrt{27}} K_3 t)^{1/3}} \tag{A.3}$$

$$T(t) = T_0(1 + \frac{3\beta^2 N_0^2}{T_0^3 \sqrt{27}} K_3 t)^{1/9} \tag{A.4}$$

where $\beta = (m\omega^2/2\pi k_B)^{3/2}$ is a constant that depends only on the trapping frequency of the harmonic confinement.

By an experimental point of view, trapping frequencies are known with a good accuracy, $\sigma\omega/\omega \simeq 5/200$. On the contrary, the starting atom number and temperature are measured with larger uncertainties, which has the most significant effect on the uncertainty in the measurement of three-body loss rates. In the case of a single-species thermal cloud, it is possible to simplify the system of equations in Eqs. A.3-A.4, by introducing the quantity $\alpha(t) = T^3(t)/N^2(t)$. With some calculations it is possible to prove that:

$$\alpha(t) = T_0^3/N_0^2 + 3K_3\frac{\beta^2}{\sqrt{27}}t \tag{A.5}$$

From a linear fit of this quantity it is then possible to directly measure the three-body recombination coefficient knowing the trapping frequency.

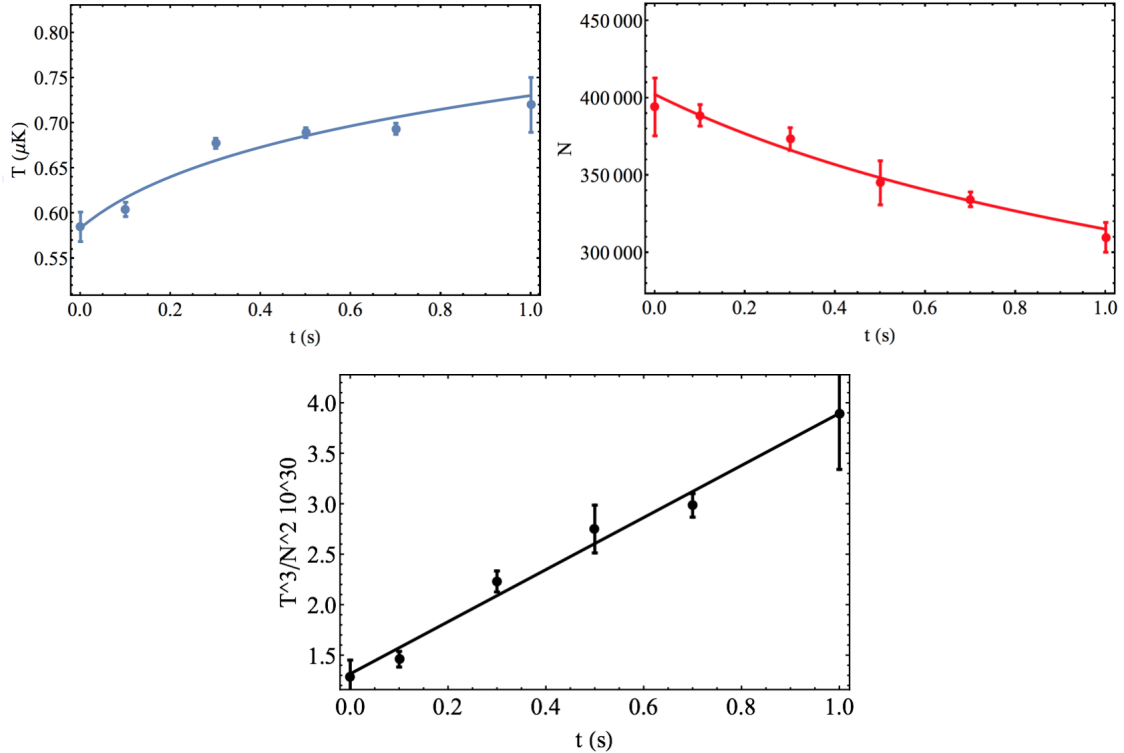We measure the evoultion of both the atom number and the temperature for single-species

Figure A.1: Atom number, temperature and the parameter α for the internal state $|1, -1\rangle$.

thermal samples in the two hyperfine states of interest, $|1, 0\rangle$ and $|1, -1\rangle$, at a magnetic field B=56.5 G. The temperature is measured from a time-of-flight expansion from $\sigma(tof) = \sqrt{\sigma_0^2 + \frac{kBT}{mK}tof^2}$, where σ_0 is the initial size of the cloud. The thermal cloud in state $|1, 0\rangle$ is produced from the one in state $|1, -1\rangle$ with an RF π pulse, performed at a magnetic field B_0 where the intra-species scattering lengths are equal so as to optimize the trasfer efficiency. The magnetic field is then adiabatically ramped to 56.5G.

For state $|1, -1\rangle$, the results are reported in Fig. A.1. We measure a three-body recombination coefficient $K_{-1-1-1} = 1.4 \times 10^{-28} cm^6/s$, with an uncertainty of a factor 2 (mainly due to a 25% uncertainty on the atom number). This value is compatible with the background three-body recombination of ^{39}K.

The losses in the other state are instead much larger since it is closer to a Feshbach resonance [84]. Results are reported in Fig. A.2. In this case we measure $K_{000} = 5.2 \times 10^{-27} cm^6/s$, again with an uncertainty of a factor 2, which is more than one order of magnitude larger than K_{-1-1-1}.

We verify the results of these measurements also using BECs.

A.2   Three-Body losses in a BEC

It is possible to analytically calculate the evolution of the mean square density due to three-body losses also for a BEC in the Thomas-Fermi limit. In this case it is possible to prove that [123]:

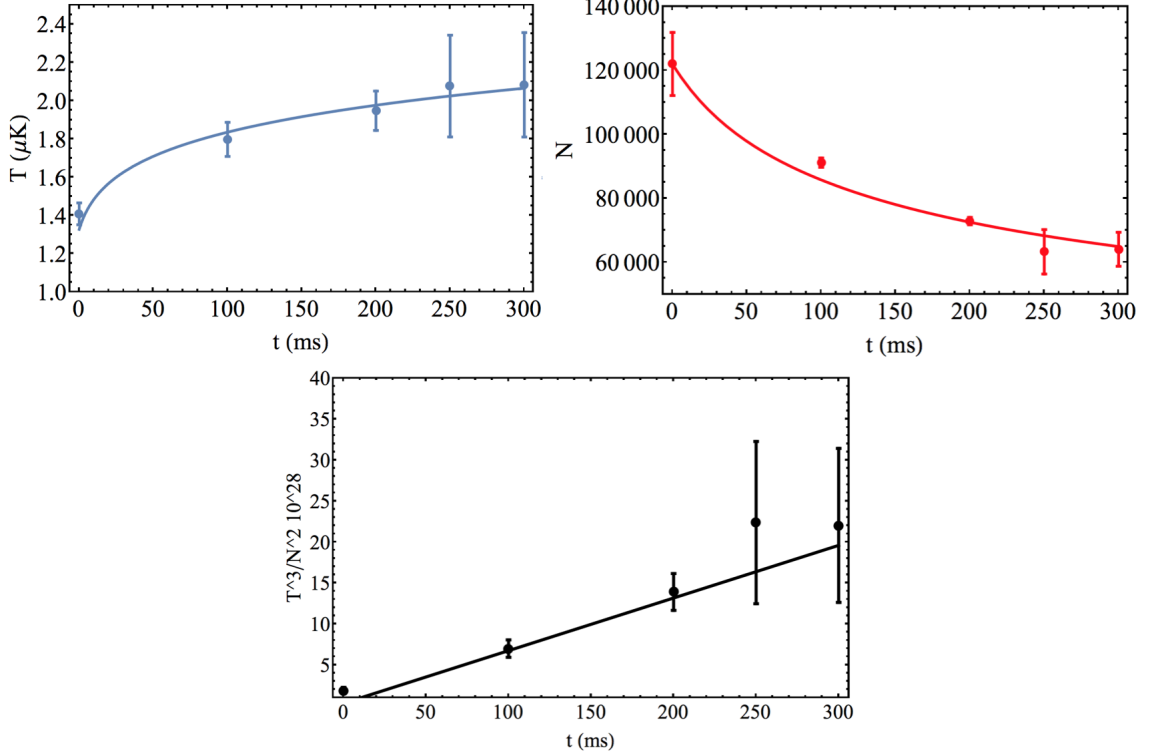$$N(t) = \frac{N_0}{(1 + 4/5K_3^{BEC}N_0^{4/5}c_3t)^{5/4}} \tag{A.6}$$

Figure A.2: Atom number, temperature and the parameter α for the internal state $|1,0\rangle$.

where $c_3 = 7/6(15^{2/5}m\omega/14\pi\hbar\sqrt{a})$. The three-body recombination coefficient $K_3^{BEC} = K_3/3!$, where the reduction by a factor 3! is due to the anti-bunching effect related to Bose statistic [124].

Results are reported in Fig. A.3 for both internal states at a magnetic field of 56.5 G. The BEC in state $|1,0\rangle$ is produced as before using a RF π pulse. In this state we measure $K_{000} = 6K_{000}^{BEC} = 3.5 \times 10^{-27}$ cm^6/s. In the $|1,-1\rangle$ state we instead measure $K_{-1-1-1} = 6K_{-1-1-1}^{BEC} = 1.1 \times 10^{-28}$ cm^6/s. Both measurements are in good agreement with the ones obtained using the thermal clouds.

A.3 Three-body losses in a mixture

Finally we want to characterize the mixed channels, i.e. the three-body losses due to scattering between two atoms in state $|1,-1\rangle$ and one in $|1,0\rangle$ and viceversa. The associated coefficients are K_{-1-10} and K_{-100} respectively.

Studies about three-body losses in a mixture have been so far performed in a hetoronuclear mixture [125], but the conditions they had there and that significantly simplified the analysis are not analogously valid in our case. We will anyway try to estimate at least the orders of magnitudes of K_{-1-10} and K_{-100}. In the mixture case the loss process is characterized by three coupled differential equations, describing the decay of the atom number in the two states and the increase of temperature, that we assume to be the same for the two species since they thermalize. For a homonuclear mixture we have:

$$\frac{dN_{-1}}{dt} = -\frac{\beta^2}{\sqrt{27}T(t)^3}\left(K_{-1-1-1}N_{-1}^3 + \frac{2}{3}K_{-1-10}N_{-1}^2 N_0 + \frac{1}{3}K_{-100}N_{-1}N_0^2\right) \tag{A.7}$$

$$\frac{dN_0}{dt} = -\frac{\beta^2}{\sqrt{27}T(t)^3}\left(K_{000}N_{-1}^3 + \frac{2}{3}K_{-100}N_0^2 N_{-1} + \frac{1}{3}K_{-1-10}N_{-1}^2 N_0\right) \tag{A.8}$$
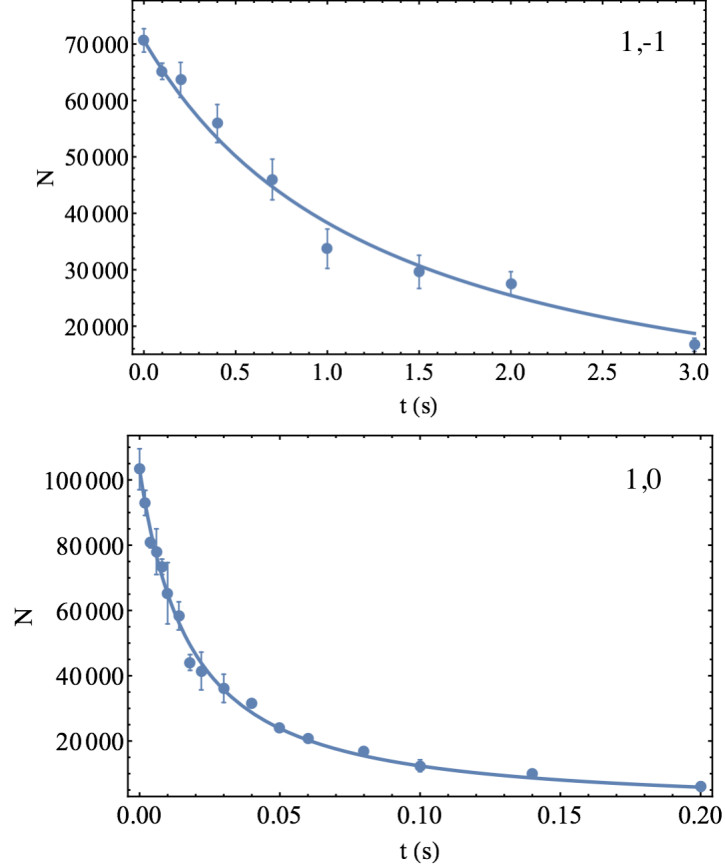
Figure A.3: Decay of a BEC in the Thomas Fermi limit due to three-body recombination. Above the measurement for the state $|1,-1\rangle$ below for the $|1,0\rangle$.

$$\frac{dT}{dt} = -\frac{\beta^2}{\sqrt{27}T(t)^2(N_{tot}(t))}(K_{000}N_{-1}^3 + K_{-100}N_0^2N_{-1} + K_{-1-10}N_{-1}^2N_0 + K_{-1-1-1}N_{-1}^3) \quad \text{(A.9)}$$

We solve numerically the system of these three coupled differential equations using the values of K_{-1-1-1} and K_{000} measured with the single-component thermal clouds, for different values of $K_{-1-1,0}$ and K_{-100}. We then choose the parameters that minimize the standard deviation from the experimental data. Results are plotted in Fig. A.4. The results depend critically on the values of K_{-1-1-1} and K_{000}. We find that the mixed channels are of the same order of magnitude of K_{-1-1-1}.

In conclusion, we find the most relevant loss channel is the one associated to K_{000} which seems to be at least one order of magnitude larger than the other three.

In the future it could be interesting to characterize with better accuracy the dependence of the three-body recombination coefficient on the magnetic field. In addition, a more careful analysis of the losses behavior at large density is still missing. For instance it could be interesting to investigate if the droplet is affected by avalanche terms that could introduce additional losses in the system.
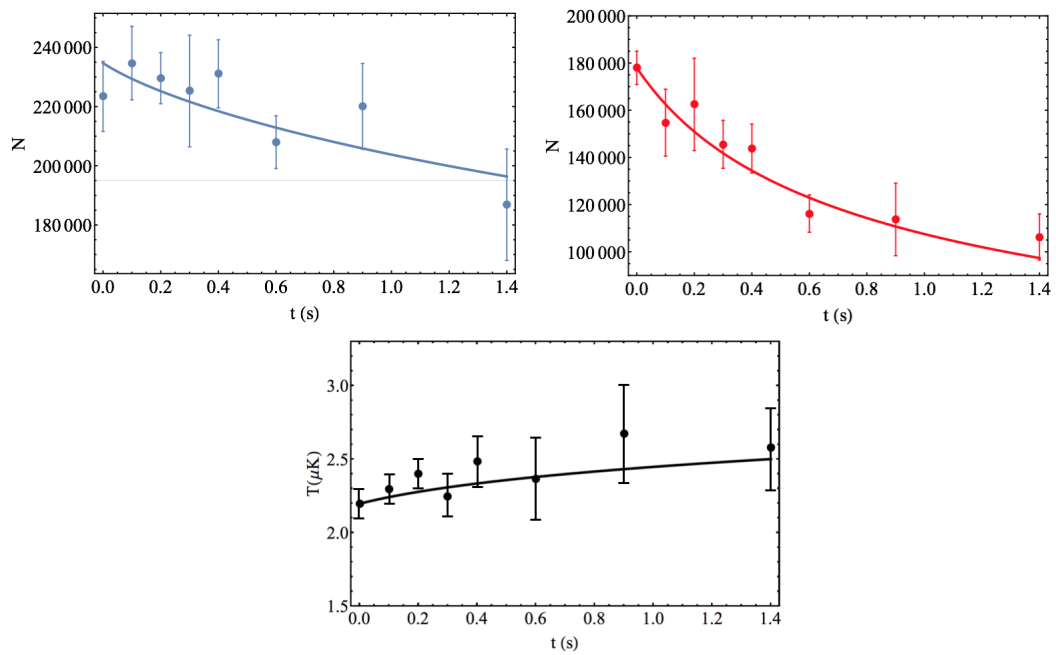
Figure A.4: In the above row is the decay of the atom number in state $|1, -1\rangle$ (left) and $|1, 0\rangle$ (right) for a thermal mixture. In the bottom row is the increase of temperature. The experimental data are reported together with the result of the system of coupled differential equations, as explained in the text.

Appendix B

Calibration of the atom number with detuned repumper light

In this appendix we discuss the method we implemented to count the atom number in the droplet, used in the droplet collision experiment.

The atom counting in our set up has been calibrated using resonant repumper light $\Delta = 0$. As already described in Chapter 4, we use in the imaging sequence detuned repumper light in order to reduce the optical density of the system. For the experiment concerning the study of a single droplet, the measurement of the atom number has been performed in TOF during the Stern-Gerlach measurement, so that densities were sufficiently low to properly count the atom number using resonant repumper light. Here we calibrate the detuned imaging technique in order to be able to count the atoms during the collisions measurements, even at high densities.

To do it we create a BEC in state $|1, -1\rangle$ and we let it expand for 8ms. After that we count the atom number with a resonant and calibrated absorption imaging, measuring $N_{BEC}^{\Delta_{rep}=0}$ with an uncertainty ΔN provided by the uncertainty in the imaging calibration and by the fluctuations of N due to the noise in the preparation of the BEC. We repeat the same procedure changing the rempumper detuning and measuring $N_{BEC}^{\Delta_{rep}}$ for every value of Δ_{rep}. As the detuning increases the signal becomes smaller compared to the noise. To increase it we reduce the TOF so that the optical density of the cloud is larger. Since we are observing the same BEC prepared in the same way, the atom number has to be the same for every value of Δ_{rep}. The ratio between $N_{BEC}^{\Delta_{rep}=0}$ and $N_{BEC}^{\Delta_{rep}}$ gives a constant $\alpha(\Delta_{rep}) = \frac{\langle N_{\Delta_{rep}=0}\rangle}{\langle N_{\Delta_{rep}}\rangle}$ that we use to get the atom number from a detuned absorption imaging.

In Fig. B.1 is reported the experimental measurement of $\alpha(\Delta_{rep})$ for different values of Δ_{rep}. The mean value $\langle \alpha(\Delta_{rep})\rangle$ is obtained as

$$\langle \alpha(\Delta_{rep})\rangle = \frac{\langle N_{\Delta_{rep}=0}\rangle}{\langle N_{\Delta_{rep}}\rangle} \tag{B.1}$$

where $\langle N_{\Delta_{rep}}\rangle$ is the mean atom number measured with a given value of the repumper detuning, obtained by averaging over 10 experimental realizations. To every $\langle N_{\Delta_{rep}}\rangle$ is associated an uncertainty $\Delta N_{\Delta_{rep}}$. To evaluate the uncertainty in the estimation of $\alpha(\Delta_{rep})$, we use a standard result in the error propagation theory for a variable that is evaluated as the ratio between two stochastic variables

$$\Delta_{\alpha(\Delta_{rep})} = \sqrt{(\Delta N_{\Delta=0}\frac{\delta\alpha}{\delta N_{\Delta=0}})^2 + (\Delta N_{\Delta}\frac{\delta\alpha}{\delta N_{\Delta}})^2} \tag{B.2}$$

The calibration performed here is valid if the intensity I_Δ of the repumper beam with a given detuning Δ does not change during the measurement acquisition. We monitor it to make
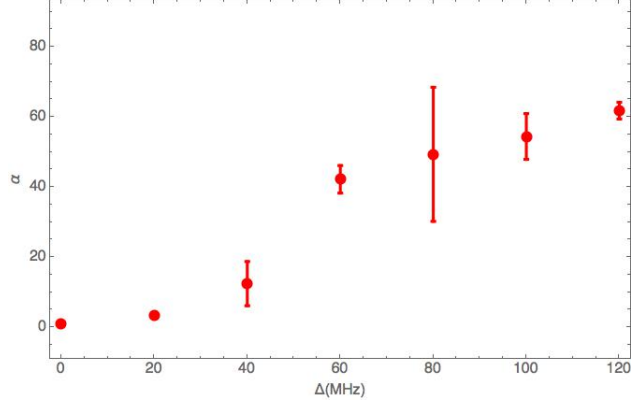
Figure B.1: Experimental measure of $\alpha(\Delta_{rep})$ with the relative error bar. Note that the detuning used in the measurement reported in Fig. 4.7 does not appear here. Although, the repumper intensity was also changed in the two measurements, so that in Fig. B1 the point at 120MHz corresponds to the same scattering rate of the repumper light as in the measurement in Fig. 4.7.

sure that it is constant over the whole measurement. We have then obtained the calibration for the atom numbere acquired via the detuned imaging as: $N = (\alpha_\Delta \pm \Delta\alpha_\Delta)N_\Delta$.

Bibliography

[1] Mike H Anderson, Jason R Ensher, Michael R Matthews, Carl E Wieman, and Eric A Cornell. Observation of bose-einstein condensation in a dilute atomic vapor. *science*, 269(5221):198–201, 1995.

[2] Kendall B Davis, M-O Mewes, Michael R Andrews, NJ Van Druten, DS Durfee, DM Kurn, and Wolfgang Ketterle. Bose-einstein condensation in a gas of sodium atoms. *Physical review letters*, 75(22):3969, 1995.

[3] Igor Ferrier-Barbut and Tilman Pfau. Quantum liquids get thin. *Science*, 359(6373):274–275, 2018.

[4] Aurel Bulgac. Dilute quantum droplets. *Physical review letters*, 89(5):050402, 2002.

[5] DS Petrov. Quantum mechanical stabilization of a collapsing bose-bose mixture. *Physical review letters*, 115(15):155302, 2015.

[6] Holger Kadau, Matthias Schmitt, Matthias Wenzel, Clarissa Wink, Thomas Maier, Igor Ferrier-Barbut, and Tilman Pfau. Observing the rosensweig instability of a quantum ferrofluid. *Nature*, 530(7589):194, 2016.

[7] Igor Ferrier-Barbut, Holger Kadau, Matthias Schmitt, Matthias Wenzel, and Tilman Pfau. Observation of quantum droplets in a strongly dipolar bose gas. *Physical review letters*, 116(21):215301, 2016.

[8] Matthias Schmitt, Matthias Wenzel, Fabian Böttcher, Igor Ferrier-Barbut, and Tilman Pfau. Self-bound droplets of a dilute magnetic quantum liquid. *Nature*, 539(7628):259, 2016.

[9] L Chomaz, S Baier, D Petter, MJ Mark, F Wächtler, Luis Santos, and F Ferlaino. Quantum-fluctuation-driven crossover from a dilute bose-einstein condensate to a macrodroplet in a dipolar quantum fluid. *Physical Review X*, 6(4):041039, 2016.

[10] CR Cabrera, L Tanzi, J Sanz, B Naylor, P Thomas, P Cheiney, and L Tarruell. Quantum liquid droplets in a mixture of bose-einstein condensates. *Science*, 359(6373):301–304, 2018.

[11] P Cheiney, CR Cabrera, J Sanz, B Naylor, L Tanzi, and L Tarruell. Bright soliton to quantum droplet transition in a mixture of bose-einstein condensates. *Physical review letters*, 120(13):135301, 2018.

[12] G. Semeghini, G. Ferioli, L. Masi, C. Mazzinghi, L. Wolswijk, F. Minardi, M. Modugno, G. Modugno, M. Inguscio, and M. Fattori. Self-bound quantum droplets of atomic mixtures in free space. *Phys. Rev. Lett.*, 120:235301, Jun 2018.

[13] J Peter Toennies and Andrey F Vilesov. Superfluid helium droplets: a uniquely cold nanomatrix for molecules and molecular complexes. *Angewandte Chemie International Edition*, 43(20):2622–2648, 2004.

[14] Manuel Barranco, Rafael Guardiola, Susana Hernández, Ricardo Mayol, Jesús Navarro, and Martí Pi. Helium nanodroplets: An overview. *Journal of low temperature physics*, 142(1-2):1, 2006.

[15] Jean Dalibard. Collisional dynamics of ultra-cold atomic gases. In *Proceedings of the International School of Physics-Enrico Fermi*, volume 321, page 14, 1999.

[16] Cheng Chin, Rudolf Grimm, Paul Julienne, and Eite Tiesinga. Feshbach resonances in ultracold gases. *Reviews of Modern Physics*, 82(2):1225, 2010.

[17] N Bogoliubov. On the theory of superfluidity. *J. Phys*, 11(1):23, 1947.

[18] Lev Pitaevskii and Sandro Stringari. *Bose-Einstein condensation and superfluidity*, volume 164. Oxford University Press, 2016.

[19] TD Lee and CN Yang. Many-body problem in quantum mechanics and quantum statistical mechanics. *Physical Review*, 105(3):1119, 1957.

[20] Tsin D Lee, Kerson Huang, and Chen N Yang. Eigenvalues and eigenfunctions of a bose system of hard spheres and its low-temperature properties. *Physical Review*, 106(6):1135, 1957.

[21] Frederic Chevy and Christophe Salomon. Strongly correlated bose gases. *Journal of Physics B: Atomic, Molecular and Optical Physics*, 49(19):192001, 2016.

[22] Philip Makotyn, Catherine E Klauss, David L Goldberger, EA Cornell, and Deborah S Jin. Universal dynamics of a degenerate unitary bose gas. *Nature Physics*, 10(2):116, 2014.

[23] Nir Navon, Swann Piatecki, Kenneth Günter, Benno Rem, Trong Canh Nguyen, Frédéric Chevy, Werner Krauth, and Christophe Salomon. Dynamics and thermodynamics of the low-temperature strongly interacting bose gas. *Physical review letters*, 107(13):135301, 2011.

[24] Shina Tan. Energetics of a strongly correlated fermi gas. *Annals of Physics*, 323(12):2952–2970, 2008.

[25] Eric Braaten, Daekyoung Kang, and Lucas Platter. Universal relations for identical bosons from three-body physics. *Physical review letters*, 106(15):153005, 2011.

[26] RJ Wild, P Makotyn, JM Pino, EA Cornell, and DS Jin. Measurements of tan's contact in an atomic bose-einstein condensate. *Physical review letters*, 108(14):145305, 2012.

[27] Richard J Fletcher, Raphael Lopes, Jay Man, Nir Navon, Robert P Smith, Martin W Zwierlein, and Zoran Hadzibabic. Two-and three-body contacts in the unitary bose gas. *Science*, 355(6323):377–380, 2017.

[28] R Chang, Q Bouton, H Cayla, C Qu, Alain Aspect, CI Westbrook, and D Clément. Momentum-resolved observation of thermal and quantum depletion in a bose gas. *Physical review letters*, 117(23):235303, 2016.

[29] Raphael Lopes, Christoph Eigen, Nir Navon, David Clément, Robert P Smith, and Zoran Hadzibabic. Quantum depletion of a homogeneous bose-einstein condensate. *Physical review letters*, 119(19):190404, 2017.

[30] Grigory E Volovik. *The universe in a helium droplet*, volume 117. Oxford University Press on Demand, 2003.

[31] SB Papp, JM Pino, and CE Wieman. Tunable miscibility in a dual-species bose-einstein condensate. *Physical review letters*, 101(4):040402, 2008.

[32] G Thalhammer, G Barontini, L De Sarlo, J Catani, F Minardi, and M Inguscio. Double species bose-einstein condensate with tunable interspecies interactions. *Physical review letters*, 100(21):210402, 2008.

[33] David M Larsen. Binary mixtures of dilute bose gases with repulsive interactions at low temperature. *Annals of Physics (New York)(US)*, 24, 1963.

[34] VR Pandharipande, Steven C Pieper, and RB Wiringa. Variational monte carlo calculations of ground states of liquid he 4 and he 3 drops. *Physical Review B*, 34(7):4571, 1986.

[35] Viktor Cikojević, Krešimir Dželalija, Petar Stipanović, L Vranješ Markić, and Jordi Boronat. Ultradilute quantum liquid drops. *Physical Review B*, 97(14):140502, 2018.

[36] LD Landau and EM Lifshitz. *Course of theoretical physics. vol. 6: Fluid mechanics.* London, 1959.

[37] Alberto Cappellaro, Tommaso Macrì, and Luca Salasnich. Collective modes across the soliton-droplet crossover in binary bose mixtures. *Physical Review A*, 97(5):053623, 2018.

[38] F Wächtler and L Santos. Ground-state properties and elementary excitations of quantum droplets in dipolar bose-einstein condensates. *Physical Review A*, 94(4):043618, 2016.

[39] Falk Wächtler and L Santos. Quantum filaments in dipolar bose-einstein condensates. *Physical Review A*, 93(6):061603, 2016.

[40] Chiara Menotti and Sandro Stringari. Collective oscillations of a one-dimensional trapped bose-einstein gas. *Physical Review A*, 66(4):043610, 2002.

[41] Thierry Lahaye, Jonas Metz, Bernd Froehlich, Tobias Koch, Maximilian Meister, Axel Griesmaier, Tilman Pfau, Hiroki Saito, Yuki Kawaguchi, and Masahito Ueda. d-wave collapse and explosion of a dipolar bose-einstein condensate. *Physical review letters*, 101(8):080401, 2008.

[42] J Schuster, A Marte, S Amtage, B Sang, G Rempe, and HCW Beijerinck. Avalanches in a bose-einstein condensate. *Physical review letters*, 87(17):170404, 2001.

[43] Thierry Lahaye, C Menotti, L Santos, M Lewenstein, and T Pfau. The physics of dipolar bosonic quantum gases. *Reports on Progress in Physics*, 72(12):126401, 2009.

[44] Aristeu RP Lima and Axel Pelster. Quantum fluctuations in dipolar bose gases. *Physical Review A*, 84(4):041604, 2011.

[45] Matthias Wenzel, Fabian Böttcher, Tim Langen, Igor Ferrier-Barbut, and Tilman Pfau. Striped states in a many-body system of tilted dipoles. *Physical Review A*, 96(5):053630, 2017.

[46] Igor Ferrier-Barbut, Matthias Schmitt, Matthias Wenzel, Holger Kadau, and Tilman Pfau. Liquid quantum droplets of ultracold magnetic atoms. *Journal of Physics B: Atomic, Molecular and Optical Physics*, 49(21):214004, 2016.

[47] Igor Ferrier-Barbut, Matthias Wenzel, Fabian Böttcher, Tim Langen, Mathieu Isoard, Sandro Stringari, and Tilman Pfau. Scissors mode of dipolar quantum droplets of dysprosium atoms. *Physical review letters*, 120(16):160402, 2018.

[48] Igor Ferrier-Barbut, Matthias Wenzel, Matthias Schmitt, Fabian Böttcher, and Tilman Pfau. Onset of a modulational instability in trapped dipolar bose-einstein condensates. *Physical Review A*, 97(1):011604, 2018.

[49] SK Adhikari. Statics and dynamics of a self-bound matter-wave quantum ball. *Physical Review A*, 95(2):023606, 2017.

[50] Fabio Cinti, Alberto Cappellaro, Luca Salasnich, and Tommaso Macrì. Superfluid filaments of dipolar bosons in free space. *Physical review letters*, 119(21):215302, 2017.

[51] Eunseong Kim and MHW Chan. Probable observation of a supersolid helium phase. *Nature*, 427(6971):225, 2004.

[52] Julian Léonard, Andrea Morales, Philip Zupancic, Tilman Esslinger, and Tobias Donner. Supersolid formation in a quantum gas breaking a continuous translational symmetry. *Nature*, 543(7643):87, 2017.

[53] Jun-Ru Li, Jeongwon Lee, Wujie Huang, Sean Burchesky, Boris Shteynas, Furkan Çağrı Top, Alan O Jamison, and Wolfgang Ketterle. A stripe phase with supersolid properties in spin–orbit-coupled bose–einstein condensates. *Nature*, 543(7643):91, 2017.

[54] Luca Tanzi, Eleonora Lucioni, Francesca Famà, Jacopo Catani, Andrea Fioretti, Carlo Gabbanini, and Giovanni Modugno. Observation of stable stripes in a dipolar quantum gas. *arXiv preprint arXiv:1811.02613*, 2018.

[55] Abdelâali Boudjemâa. Fluctuations and quantum self-bound droplets in a dipolar bose-bose mixture. *arXiv preprint arXiv:1809.06458*, 2018.

[56] A Trautmann, P Ilzhöfer, G Durastante, C Politi, M Sohmen, MJ Mark, and F Ferlaino. Dipolar quantum mixtures of erbium and dysprosium atoms. *arXiv preprint arXiv:1807.07555*, 2018.

[57] Kali E Wilson, Niclas Westerberg, Manuel Valiente, Callum W Duncan, Ewan M Wright, Patrik Öhberg, and Daniele Faccio. Observation of photon droplets and their dynamics. *arXiv preprint arXiv:1808.00752*, 2018.

[58] Niclas Westerberg, Kali E Wilson, Callum W Duncan, Daniele Faccio, Ewan M Wright, Patrik Öhberg, and Manuel Valiente. Self-bound droplets of light with orbital angular momentum. *arXiv preprint arXiv:1801.08539*, 2018.

[59] Yu Pan and Kazuhiko Suga. Numerical simulation of binary liquid droplet collision. *Physics of Fluids*, 17(8):082105, 2005.

[60] John William Strutt and Baron Rayleigh. *The theory of sound*. Dover, 1945.

[61] SP Lin and RD Reitz. Drop and spray formation from a liquid jet. *Annual Review of Fluid Mechanics*, 30(1):85–105, 1998.

[62] Rolf D Reitz and R Diwakar. Structure of high-pressure fuel sprays. Technical report, SAE Technical Paper, 1987.

[63] PR Brazier-Smith, SG Jennings, and J Latham. The interaction of falling water drops: coalescence. *Proc. R. Soc. Lond. A*, 326(1566):393–408, 1972.

[64] J Qian and CK Law. Regimes of coalescence and separation in droplet collision. *Journal of Fluid Mechanics*, 331:59–80, 1997.

[65] R Donangelo and LF Canto. Studies of nucleus-nucleus collisions with a schematic liquid-drop model and one-body dissipation. *Nuclear Physics A*, 451(2):349–364, 1986.

[66] M El-Nadi and A Hashem. Liquid drop model and heavy ion collisions. *Physical Review C*, 23(6):2586, 1981.

[67] Aurel Bulgac and Shi Jin. Dynamics of fragmented condensates and macroscopic entanglement. *Physical review letters*, 119(5):052501, 2017.

[68] Piotr Magierski, Kazuyuki Sekizawa, and Gabriel Wlazłowski. Novel role of superfluidity in low-energy nuclear reactions. *Physical review letters*, 119(4):042501, 2017.

[69] Jason HV Nguyen, Paul Dyke, De Luo, Boris A Malomed, and Randall G Hulet. Collisions of matter-wave solitons. *Nature Physics*, 10(12):918, 2014.

[70] Lev Khaykovich and Boris A Malomed. Deviation from one dimensionality in stationary properties and collisional dynamics of matter-wave solitons. *Physical Review A*, 74(2):023607, 2006.

[71] CL Vicente, C Kim, HJ Maris, and GM Seidel. Coalescence of levitated he ii drops. *Journal of low temperature physics*, 121(5-6):627–632, 2000.

[72] Humphrey J Maris. Analysis of the early stage of coalescence of helium drops. *Physical Review E*, 67(6):066309, 2003.

[73] GE Astrakharchik and BA Malomed. Dynamics of one-dimensional quantum droplets. *arXiv preprint arXiv:1803.07165*, 2018.

[74] Kevin Henderson, Changhyun Ryu, Calum MacCormick, and MG Boshier. Experimental demonstration of painting arbitrary and dynamic potentials for bose–einstein condensates. *New Journal of Physics*, 11(4):043030, 2009.

[75] Alexander L Gaunt, Tobias F Schmidutz, Igor Gotlibovych, Robert P Smith, and Zoran Hadzibabic. Bose-einstein condensation of atoms in a uniform potential. *Physical review letters*, 110(20):200406, 2013.

[76] G Gauthier, I Lenton, N McKay Parry, M Baker, MJ Davis, H Rubinsztein-Dunlop, and TW Neely. Configurable microscopic optical potentials for bose-einstein condensates using a digital-micromirror device. *arXiv preprint arXiv:1605.04928*, 2016.

[77] Rudolf Grimm, Matthias Weidemüller, and Yurii B Ovchinnikov. Optical dipole traps for neutral atoms. In *Advances in atomic, molecular, and optical physics*, volume 42, pages 95–170. Elsevier, 2000.

[78] DJ Berkeland, JD Miller, James C Bergquist, Wayne M Itano, and David J Wineland. Minimization of ion micromotion in a paul trap. *Journal of applied physics*, 83(10):5025–5033, 1998.

[79] Marko Cetina, Andrew T Grier, and Vladan Vuletić. Micromotion-induced limit to atom-ion sympathetic cooling in paul traps. *Physical review letters*, 109(25):253201, 2012.

[80] Manuele Landini. *A tunable Bose-Einstein condensate for quantum interferometry*. PhD thesis, University of Trento, 2012.

[81] M Landini, S Roy, L Carcagní, D Trypogeorgos, M Fattori, M Inguscio, and G Modugno. Sub-doppler laser cooling of potassium atoms. *Physical review A*, 84(4):043432, 2011.

[82] Manuele Landini, Sanjukta Roy, Giacomo Roati, Andrea Simoni, Massimo Inguscio, Giovanni Modugno, and Marco Fattori. Direct evaporative cooling of 39 k atoms to bose-einstein condensation. *Physical Review A*, 86(3):033421, 2012.

[83] Giulia Semeghini. *Ultracold atoms in three-dimensional disorder: measurement of the mobility edge and effect of weak interactions.* PhD thesis, LENS - European Laboratory for Non-Linear Spectroscopy, 2015.

[84] Chiara D'Errico, Matteo Zaccanti, Marco Fattori, Giacomo Roati, Massimo Inguscio, Giovanni Modugno, and Andrea Simoni. Feshbach resonances in ultracold 39k. *New Journal of physics*, 9(7):223, 2007.

[85] L Wacker, Nils Byg Jørgensen, D Birkmose, Ridha Horchani, Wolfgang Ertmer, Carsten Klempt, Nils Winter, Jacob Sherson, and JJ Arlt. Tunable dual-species bose-einstein condensates of k 39 and rb 87. *Physical Review A*, 92(5):053602, 2015.

[86] Torben A Schulze, Torsten Hartmann, Kai K Voges, Matthias W Gempel, Eberhard Tiemann, Alessandro Zenesini, and Silke Ospelkaus. Feshbach spectroscopy and dual-species bose-einstein condensation of na 23- k 39 mixtures. *Physical Review A*, 97(2):023623, 2018.

[87] DM Harber, HJ Lewandowski, JM McGuirk, and Eric A Cornell. Effect of cold collisions on spin coherence and resonance shifts in a magnetically trapped ultracold gas. *Physical Review A*, 66(5):053616, 2002.

[88] Nils B. Jørgensen, Georg M. Bruun, and Jan J. Arlt. Dilute fluid governed by quantum fluctuations. *Phys. Rev. Lett.*, 121:173403, Oct 2018.

[89] MR Andrews, M-O Mewes, NJ Van Druten, DS Durfee, DM Kurn, and W Ketterle. Direct, nondestructive observation of a bose condensate. *Science*, 273(5271):84–87, 1996.

[90] Miroslav Gajdacz, Poul L Pedersen, Troels Mørch, Andrew J Hilliard, Jan Arlt, and Jacob F Sherson. Non-destructive faraday imaging of dynamically controlled ultracold atoms. *Review of Scientific Instruments*, 84(8):083105, 2013.

[91] Wolfgang Ketterle, Dallin S Durfee, and DM Stamper-Kurn. Making, probing and understanding bose-einstein condensates. *arXiv preprint cond-mat/9904034*, 1999.

[92] Laura Corman, Jean-Loup Ville, Raphaël Saint-Jalm, Monika Aidelsburger, Tom Bienaimé, Sylvain Nascimbène, Jean Dalibard, and Jérôme Beugnon. Transmission of near-resonant light through a dense slab of cold atoms. *Physical Review A*, 96(5):053629, 2017.

[93] Stephan Jennewein, Mondher Besbes, NJ Schilder, SD Jenkins, Christophe Sauvan, J Ruostekoski, J-J Greffet, Yvan RP Sortais, and Antoine Browaeys. Coherent scattering of near-resonant light by a dense microscopic cold atomic cloud. *Physical review letters*, 116(23):233601, 2016.

[94] Juha Javanainen, Janne Ruostekoski, Yi Li, and Sung-Mi Yoo. Shifts of a resonance line in a dense atomic sample. *Physical review letters*, 112(11):113603, 2014.

[95] Wolfgang Muessel, Helmut Strobel, Maxime Joos, Eike Nicklas, Ion Stroescu, Jiří Tomkovič, David B Hume, and Markus K Oberthaler. Optimized absorption imaging of mesoscopic atomic clouds. *Applied Physics B*, 113(1):69–73, 2013.

[96] Michael A Joffe, Wolfgang Ketterle, Alex Martin, and David E Pritchard. Transverse cooling and deflection of an atomic beam inside a zeeman slower. *JOSA B*, 10(12):2257–2262, 1993.

[97] G Spagnolli, G Semeghini, L Masi, G Ferioli, A Trenkwalder, S Coop, M Landini, L Pezze, G Modugno, M Inguscio, et al. Crossing over from attractive to repulsive interactions in a tunneling bosonic josephson junction. *Physical review letters*, 118(23):230403, 2017.

[98] Giulia Semeghini, Manuele Landini, Patricia Castilho, Sanjukta Roy, Giacomo Spagnolli, Andreas Trenkwalder, Marco Fattori, Massimo Inguscio, and Giovanni Modugno. Measurement of the mobility edge for 3d anderson localization. *Nature Physics*, 11(7):554–559, 2015.

[99] A Trenkwalder, G Spagnolli, G Semeghini, S Coop, M Landini, P Castilho, L Pezze, G Modugno, M Inguscio, A Smerzi, et al. Quantum phase transitions with parity-symmetry breaking and hysteresis. *Nature physics*, 12(9):826, 2016.

[100] Elmar Haller, Mohamed Rabie, Manfred J Mark, Johann G Danzl, Russell Hart, Katharina Lauber, Guido Pupillo, and H-C Nägerl. Three-body correlation functions and recombination rates for bosons in three dimensions and one dimension. *Physical review letters*, 107(23):230404, 2011.

[101] Giovanni Giusti. Collision between quantum droplets, 2018.

[102] Matthias Wenzel, Tilman Pfau, and Igor Ferrier-Barbut. A fermionic impurity in a dipolar quantum droplet. *Physica Scripta*, 93(10):104004, 2018.

[103] Alberto Cappellaro, Tommaso Macrì, Giovanni F Bertacco, and Luca Salasnich. Equation of state and self-bound droplet in rabi-coupled bose mixtures. *Scientific reports*, 7(1):13358, 2017.

[104] DS Petrov and GE Astrakharchik. Ultradilute low-dimensional liquids. *Physical review letters*, 117(10):100401, 2016.

[105] Paweł Ziń, Maciej Pylak, Tomasz Wasak, Mariusz Gajda, and Zbigniew Idziaszek. Quantum bose-bose droplets at a dimensional crossover. *arXiv preprint arXiv:1805.11186*, 2018.

[106] C Raman, M Köhl, R Onofrio, DS Durfee, CE Kuklewicz, Z Hadzibabic, and W Ketterle. Evidence for a critical velocity in a bose-einstein condensed gas. *Physical Review Letters*, 83(13):2502, 1999.

[107] Martin W Zwierlein, Jamil R Abo-Shaeer, Andre Schirotzek, Christian H Schunck, and Wolfgang Ketterle. Vortices and superfluidity in a strongly interacting fermi gas. *Nature*, 435(7045):1047, 2005.

[108] Jacopo Nespolo, Grigori E Astrakharchik, and Alessio Recati. Andreev–bashkin effect in superfluid cold gases mixtures. *New Journal of Physics*, 19(12):125005, 2017.

[109] Luca Parisi, GE Astrakharchik, and Stefano Giorgini. Spin dynamics and andreev-bashkin effect in mixtures of one-dimensional bose gases. *arXiv preprint arXiv:1801.03446*, 2018.

[110] GJ Milburn, J Corney, Ewan M Wright, and DF Walls. Quantum dynamics of an atomic bose-einstein condensate in a double-well potential. *Physical Review A*, 55(6):4318, 1997.

[111] Srikanth Raghavan, Augusto Smerzi, Stefano Fantoni, and SR Shenoy. Coherent oscillations between two weakly coupled bose-einstein condensates: Josephson effects, π oscillations, and macroscopic quantum self-trapping. *Physical Review A*, 59(1):620, 1999.

[112] Juha Javanainen and Misha Yu Ivanov. Splitting a trap containing a bose-einstein condensate: Atom number fluctuations. *Physical Review A*, 60(3):2351, 1999.

[113] Juha Javanainen and Han Chen. Ground state of the double-well condensate for quantum metrology. *Physical Review A*, 89(3):033613, 2014.

[114] Luca Pezzè, Augusto Smerzi, Markus K Oberthaler, Roman Schmied, and Philipp Treutlein. Non-classical states of atomic ensembles: fundamentals and applications in quantum metrology. *arXiv preprint arXiv:1609.01609*, 1609, 2016.

[115] J Esteve, C Gross, A Weller, S Giovanazzi, and MK Oberthaler. Squeezing and entanglement in a bose–einstein condensate. *Nature*, 455(7217):1216, 2008.

[116] David J Griffiths. *Introduction to quantum mechanics.* Cambridge University Press, 2016.

[117] Patrick Cheinet, Benjamin Canuel, Franck Pereira Dos Santos, Alexandre Gauguet, Florence Yver-Leduc, and Arnaud Landragin. Measurement of the sensitivity function in a time-domain atomic interferometer. *IEEE Transactions on instrumentation and measurement*, 57(6):1141–1148, 2008.

[118] Gunnar Tackmann. *Raman interferometry with free-falling and trapped atoms.* PhD thesis, Université Pierre et Marie Curie-Paris VI; Leibniz Universität Hannover, 2013.

[119] J Le Gouët, TE Mehlstäubler, Jaewan Kim, Sébastien Merlet, Andre Clairon, Arnaud Landragin, and F Pereira Dos Santos. Limits to the sensitivity of a low noise compact atomic gravimeter. *Applied Physics B*, 92(2):133–144, 2008.

[120] Joel M Hensley, Achim Peters, and Steven Chu. Active low frequency vertical vibration isolation. *Review of scientific instruments*, 70(6):2735–2741, 1999.

[121] Tino Weber, Jens Herbig, Michael Mark, Hanns-Christoph Nägerl, and Rudolf Grimm. Three-body recombination at large scattering lengths in an ultracold atomic gas. *Physical review letters*, 91(12):123201, 2003.

[122] Sanjukta Roy, Manuele Landini, Andreas Trenkwalder, Giulia Semeghini, Giacomo Spagnolli, Andrea Simoni, Marco Fattori, Massimo Inguscio, and Giovanni Modugno. Test of the universality of the three-body efimov parameter at narrow feshbach resonances. *Physical review letters*, 111(5):053202, 2013.

[123] J Söding, D Guéry-Odelin, P Desbiolles, F Chevy, H Inamori, and J Dalibard. Three-body decay of a rubidium bose–einstein condensate. *Applied physics B*, 69(4):257–261, 1999.

[124] EA Burt, RW Ghrist, CJ Myatt, MJ Holland, Eric A Cornell, and CE Wieman. Coherence, correlations, and collisions: What one learns about bose-einstein condensates from their decay. *Physical Review Letters*, 79(3):337, 1997.

[125] LJ Wacker, NB Jørgensen, D Birkmose, N Winter, M Mikkelsen, J Sherson, N Zinner, and Jan J Arlt. Universal three-body physics in ultracold krb mixtures. *Physical review letters*, 117(16):163201, 2016.